

$\text{Na}_5\text{YSi}_4\text{O}_{12}$ -type Na^+ superionic conductors for solid-state batteries

Aikai Yang

Energie & Umwelt / Energy & Environment

Band / Volume 618

ISBN 978-3-95806-731-8

Forschungszentrum Jülich GmbH
Institut für Energie- und Klimaforschung
Werkstoffsynthese und Herstellungsverfahren (IEK-1)

Na₅YSi₄O₁₂-type Na⁺ superionic conductors for solid-state batteries

Aikai Yang

Schriften des Forschungszentrums Jülich
Reihe Energie & Umwelt / Energy & Environment

Band / Volume 618

ISSN 1866-1793

ISBN 978-3-95806-731-8

Bibliografische Information der Deutschen Nationalbibliothek.
Die Deutsche Nationalbibliothek verzeichnet diese Publikation in der
Deutschen Nationalbibliografie; detaillierte Bibliografische Daten
sind im Internet über <http://dnb.d-nb.de> abrufbar.

Herausgeber und Vertrieb: Forschungszentrum Jülich GmbH
Zentralbibliothek, Verlag
52425 Jülich
Tel.: +49 2461 61-5368
Fax: +49 2461 61-6103
zb-publikation@fz-juelich.de
www.fz-juelich.de/zb

Umschlaggestaltung: Grafische Medien, Forschungszentrum Jülich GmbH

Druck: Grafische Medien, Forschungszentrum Jülich GmbH

Copyright: Forschungszentrum Jülich 2023

Schriften des Forschungszentrums Jülich
Reihe Energie & Umwelt / Energy & Environment, Band / Volume 618

D 82 (Diss. RWTH Aachen University, 2023)

ISSN 1866-1793
ISBN 978-3-95806-731-8

Vollständig frei verfügbar über das Publikationsportal des Forschungszentrums Jülich (JuSER)
unter www.fz-juelich.de/zb/openaccess.



This is an Open Access publication distributed under the terms of the [Creative Commons Attribution License 4.0](https://creativecommons.org/licenses/by/4.0/), which permits unrestricted use, distribution, and reproduction in any medium, provided the original work is properly cited.

Abstract

The development of high-performance solid-state batteries (SSBs) has gained increasing attention in recent years as a promising alternative to conventional liquid electrolyte batteries. In this context, the $\text{Na}_5\text{YSi}_4\text{O}_{12}$ -type (NYS) Na^+ superionic conductors have emerged as potential electrolyte candidates due to their high Na^+ ionic conductivity and stability in solid-state Na batteries (SSSBs).

This thesis investigates the synthesis, characterization, and electrochemical properties of NYS-type Na^+ superionic conductors, focusing on their applicability in large-scale fabrication as well as in SSBs and the development of novel compositions with higher ionic conductivity. The background of the work is introduced in the first two chapters, followed by an explanation of the preparation and characterization methods applied. The results and discussion are divided into three main parts:

First, tape-casting of thin NYS sheets using aqueous slurries has been developed. The microstructure, crystal structure, electrochemical performance and mechanical properties of the as-prepared NYS tapes have been investigated. After sintering, the obtained NYS tapes had high crystalline purity, dense microstructure (relative density $> 90\%$), and favorable mechanical properties (hardness H of 2 GPa and Young's modulus E of 45 GPa). The NYS tapes showed a total ionic conductivity of 1.0 mS cm^{-1} at room temperature (RT), a low total activation energy of 0.30 eV, and a wide electrochemical stability window of over 8 V. The critical current density (CCD) of NYS tape against Na metal electrodes reached 2.2 mA cm^{-2} and the galvanostatic cycling time was over 280 h at 0.8 mA cm^{-2} and 0.8 mAh cm^{-2} . This work not only highlights the potential of the scarcely studied silicate-based NYS ionic conductor as a functional separator but also presents a cost-efficient and eco-friendly continuous fabrication using the aqueous tape casting technique, thus is expected to boost the practical application of NYS as a solid-state electrolyte (SSE) in SSSBs.

Second, an integrated porous/dense/porous NYS trilayered scaffold is designed and fabricated by tape casting using aqueous slurries. In this template-based NYS scaffold, the dense layer in the middle serves as a separator, and the porous layers on both sides accommodate the active materials (AMs), mitigating the adverse effect induced by the volume change of AMs during the charge/discharge. Using the porous structure also increases the contact area between SSE and the AM in the electrodes, enhances the utilization rate, and homogenizes the current distribution. The Na/NYS/Na symmetric cells with Pb-coated NYS scaffold exhibit significantly reduced interfacial impedance and superior CCD of up to 3.0 mA cm^{-2} against Na metal due to improved wettability. Furthermore, the assembled Na/NYS/S full cells operated without external pressure at RT showing a high initial discharge capacity of 970 mAh g^{-1} and good cycling stability

with a capacity of 600 mAh g⁻¹ after 150 cycles (based on the mass of sulfur). This approach paves the way for the realization of economical and practical SSSBs from the perspective of ceramic manufacturing.

Third, the strategy of aliovalent cation substitution has been used to enhance ionic conductivity while preserving the crystal structure of NYS. The optimized substitution of Y³⁺ in Na₅YSi₄O₁₂ with Zr⁴⁺ introduces Na⁺ ion vacancies, giving rise to the high bulk and total conductivities of up to 6.5 and 3.3 mS cm⁻¹ at RT, respectively, with the composition Na_{4.92}Y_{0.92}Zr_{0.08}Si₄O₁₂ (NYZS). NYZS shows outstanding electrochemical stability (up to 10 V vs. Na⁺/Na), favorable interfacial compatibility with Na, and an excellent CCD of 2.4 mA cm⁻² in Na/NYZS/Na symmetric cells. The transport pathways and the mechanism of enhanced conductivity of Na⁺ ions in NYZS are elucidated by combining solid-state nuclear magnetic resonance techniques and theoretical simulations, which reveal two migration routes with the synergistic effect of enhanced Na⁺ ion vacancies and the improved chemical environment with Zr⁴⁺ substitution. NYZS extends the list of suitable SSEs and paves the way for the facile synthesis of stable, low-cost Na⁺ ion silicate electrolyte materials.

In summary, this thesis contributes to understanding the properties and potential applications of NYS-type Na⁺ superionic conductors in SSBs. The results of this study provide important insights into the development and optimization of SSSBs, which have the potential to penetrate the field of energy storage.

Kurzfassung

Die Entwicklung leistungsfähiger Festkörperbatterien (SSB für solid-state batteries) hat in den letzten Jahren als vielversprechende Alternative zu herkömmlichen Flüssigelektrolytbatterien zunehmend an Aufmerksamkeit gewonnen. In diesem Zusammenhang haben sich Festelektrolyte aus $\text{Na}_5\text{YSi}_4\text{O}_{12}$ (NYS) aufgrund ihrer hohen Na^+ -Ionenleitfähigkeit und Stabilität in Festkörper-Na-Batterien als potenziell geeignete Werkstoffe erwiesen.

In dieser Arbeit werden die Synthese, die Charakterisierung und die elektrochemischen Eigenschaften von schnellen Na^+ -Ionenleitern des NYS-Typs untersucht, wobei der Schwerpunkt auf ihre Anwendbarkeit für eine großtechnischen Herstellung, der Anwendung in SSBs und der Entwicklung neuartiger Zusammensetzungen mit höherer Ionenleitfähigkeit liegt. Der Hintergrund der Arbeit wird in den ersten beiden Kapiteln vorgestellt, gefolgt von der Erläuterung der in dieser Arbeit verwendeten Herstellungsmethoden und Charakterisierungen. Die Arbeit ist in drei experimentelle Hauptteile gegliedert:

Zunächst wurde das Foliengießen dünner NYS-Schichten mit wässrigen Suspensionen entwickelt. Das Mikrogefüge, die Kristallstruktur, die elektrochemische Leistung und die mechanischen Eigenschaften der hergestellten NYS-Folien wurden untersucht. Nach dem Sintern zeigten die NYS-Schichten eine Gesamtleitfähigkeit von $1,0 \text{ mS cm}^{-1}$ bei Raumtemperatur (RT), eine niedrige Gesamtaktivierungsenergie von $0,30 \text{ eV}$ und ein breites elektrochemisches Fenster von über 8 V . Die kritische Stromdichte von NYS-Folien gegen Na-Metall-Elektroden kann $2,2 \text{ mA cm}^{-2}$ erreichen und die galvanostatische Zykluszeit beträgt über 280 h bei $0,8 \text{ mA cm}^{-2}$ und $0,8 \text{ mAh cm}^{-2}$. Die erhaltene Folie weist eine hohe kristalline Reinheit, ein dichtes Gefüge und günstige mechanische Eigenschaften auf (Härte H von 2 GPa und Elastizitätsmodul E von 45 GPa). Diese Arbeit unterstreicht nicht nur das Potenzial des kaum untersuchten silikatbasierten NYS-Ionenleiters als funktionaler Separator, sondern stellt auch eine kosteneffiziente und umweltfreundliche kontinuierliche Herstellung mit Hilfe der wässrigen Foliengusstechnik vor, was die praktische Anwendung von NYS als Festkörperelektrolyt in Festkörper-Na-Batterien fördern dürfte.

Zweitens wird ein integriertes poröses/dichtes/poröses dreischichtiges NYS-Gerüst entworfen und durch Foliengießen mit wässrigen Suspensionen hergestellt. In dieser auf einer Platzhaltermethode basierenden NYS-Gerüststruktur dient die dichte Schicht in der Mitte als Separator und die porösen Schichten auf beiden Seiten nehmen die aktiven Materialien mit ihren Volumenänderungen während der Lade-/Entladeprozesse auf, wodurch die Kontaktfläche vergrößert und somit die Nutzungsrate erhöht und die Stromverteilung homogenisiert wird. Die symmetrischen Na/NYS/Na-Zellen mit Pb-beschichtetem NYS-Gerüst weisen aufgrund der verbesserten Benetzbarkeit des Natriums eine deutlich reduzierte Grenzflächenimpedanz und eine höhere kritische Stromdichte von bis zu $3,0 \text{ mA cm}^{-2}$ gegenüber Na-Metall auf. Darüber hinaus zeigten

Na/NYS/S-Vollzellen, die ohne externen Druck bei Raumtemperatur betrieben wurden, eine hohe anfängliche Entladekapazität von 970 mAh g⁻¹ und eine gute Zyklenstabilität mit einer Kapazität von 600 mAh g⁻¹ nach 150 Zyklen (bezogen auf die Schwefelmasse). Dieser Ansatz ebnet den Weg für die Realisierung wirtschaftlicher und praktischer Festkörperbatterien mit Na-Metallanode.

Drittens wurde die Strategie der aliovalenten Kationensubstitution genutzt, um die Ionenleitfähigkeit zu verbessern und gleichzeitig die Kristallstruktur zu erhalten. Die optimierte Substitution von Y³⁺ in Na₅YSi₄O₁₂ durch Zr⁴⁺ führt zu Na⁺-Ionenleerstellen, was zu hohen Korn- und Gesamtleitfähigkeiten von bis zu 6,5 bzw. 3,3 mS cm⁻¹ bei Raumtemperatur in der Zusammensetzung Na_{4,92}Y_{0,92}Zr_{0,08}Si₄O₁₂ (NYZS) führt. NYZS zeigt eine hervorragende elektrochemische Stabilität (bis zu 10 V gegenüber Na⁺/Na), eine günstige Grenzflächenkompatibilität mit Na und eine ausgezeichnete kritische Stromdichte von 2,4 mA cm⁻² in symmetrischen Na/NYZS/Na-Zellen. Die Transportwege und der Mechanismus der verbesserten Leitfähigkeit von Na⁺-Ionen in NYZS werden durch die Kombination von Festkörper-Kernspinresonanztechniken und theoretischen Simulationen aufgeklärt. Es konnten zwei Migrationspfade identifiziert werden, die sich durch die vermehrten Na⁺-Ionenleerstellen und der verbesserten chemischen Umgebung durch die Zr⁴⁺-Substitution ergeben. NYZS erweitert die Liste geeigneter Festkörperelektrolyte und ebnet den Weg für die einfache Synthese von stabilen, kostengünstigen Na⁺-Ionen-Silikat-Elektrolytmaterialien.

Insgesamt trägt diese Arbeit zum Verständnis der Eigenschaften und potenziellen Anwendungen von schnellen Na⁺-Ionenleitern vom Typ NYS in SSBs bei. Die Ergebnisse dieser Studie liefern wichtige Erkenntnisse für die Entwicklung und Optimierung von Festkörper-Na-Batterien, die das Potenzial haben, sich im Bereich der Energiespeicherung zu etablieren.

Table of Contents

Abstract	I
Kurzfassung	III
Table of Contents	V
List of Abbreviations	VIII
I. Introduction	1
II. Literature Review	3
2.1. Solid-state Na batteries	3
2.1.1. General introduction of batteries.....	3
2.1.2. Li- vs. Na-based batteries.....	6
2.1.3. Liquid- vs. solid-state batteries	17
2.1.4. Solid-state Na batteries	22
2.2. Solid-state Na ⁺ ionic conductors.....	23
2.2.1. Development and classification of solid-state Na ⁺ ionic conductors	23
2.2.2. The ionic transport mechanisms in solids	33
2.3. Summary of research on solid-state Na batteries.....	34
III. Synthesis and Characterization	36
3.1. Synthesis of Na ₅ YSi ₄ O ₁₂ -type materials	36
3.1.1. Raw materials and synthesis method	36
3.1.2. Introduction of tape-casting method	36
3.1.3. Sintering fundamentals	37
3.2. Characterization techniques	38
3.2.1. X-ray diffraction	38
3.2.2. Scanning electron microscopy	39
3.2.3. X-ray photoelectron spectroscopy	40
3.2.4. Transmission electron microscopy.....	41
3.2.5. Solid-state nuclear magnetic resonance	42
3.2.6. Nano-indentation.....	43
3.3. Electrochemical testing and analysis	44
3.3.1. Ionic conductivity	44
3.3.2. Electronic conductivity	45
3.3.3. Activation energy.....	46

3.3.4. Electrochemical stability window	47
3.3.5. Areal-specific resistance	47
3.3.6. Critical current density*	48
IV. Fabrication of Thin Sheets of the Sodium Superionic Conductor $\text{Na}_5\text{YSi}_4\text{O}_{12}$ with Tape Casting	49
4.1. Chapter introduction	49
4.2. Experimental	50
4.2.1. Preparation	50
4.2.2. Characterization	52
4.3. Results and discussion	53
4.3.1. Preparation, crystal structure and microstructure.....	53
4.3.2. Electrochemical performances	56
4.3.3. Mechanical properties and sintering behavior	60
4.3.4. Fabrication of thin NYS tapes with tape casting.....	63
4.4. Chapter conclusion.....	65
V. Pressureless All-Solid-State Na/S Batteries with Self-Supporting $\text{Na}_5\text{YSi}_4\text{O}_{12}$ Scaffold	66
5.1. Chapter introduction	66
5.2. Experimental	67
5.2.1. Fabrication and synthesis	67
5.2.2. Characterization	69
5.3. Results and discussion	71
5.3.1. Fabrication, microscopic and crystal structure of NYS trilayer.....	71
5.3.2. Electrochemical performance of Na/NYS/Na symmetric cells.....	73
5.3.3. Electrochemical performance of the Na/NYS/S full cells	78
5.3.4. Comparison of electrical performance with the reported data	86
5.4. Chapter conclusion.....	89
VI. Enhanced Room-Temperature Na^+ Ionic Conductivity in $\text{Na}_{4.92}\text{Y}_{0.92}\text{Zr}_{0.08}\text{Si}_4\text{O}_{12}$	91
6.1. Chapter introduction	91
6.2. Experimental	92
6.2.1. Materials preparation	92
6.2.2. Structural characterization	92
6.2.3. Electrochemical characterization	92
6.2.4. NMR measurements.....	93
6.2.5. Theoretical calculation and fitting methods.....	94
6.3. Results and discussion	94
6.3.1. Synthesis and structural analysis of NYZS	94

6.3.2. Electrical and electrochemical properties of NYZS.....	104
6.3.3. Analysis of chemical environment with NMR spectroscopy.....	114
6.3.4. Na ⁺ ion migration pathways.....	121
6.3.5. Comparison with other investigations on NYS and other oxide-based Na ⁺ ionic SSEs.....	124
6.4. Chapter conclusion.....	127
VII. Conclusion and Perspectives.....	128
References.....	130
Index of Figures.....	145
Index of Tables.....	148
Acknowledgments.....	149

List of Abbreviations

AC	Alternating Current
AM	Active Material
ASR	Areal-Specific Resistance
CCD	Critical Current Density
CPE	Constant Phase Element
CTE	Coefficient of Thermal Expansion
CV	Cyclic Voltammetry
DC	Direct Current
DEC	Diethyl Carbonate
DMC	Dimethyl Carbonate
DSC	Differential Scanning Calorimetry
EC	Ethylene Carbonate
EDX	Energy Dispersive X-ray Spectroscopy
EIS	Electrochemical Impedance Spectroscopy
EMC	Ethyl Methyl Carbonate
EN	Electronegativity
EQ	Electrochemical equivalent
EV	Electric Vehicle
FWHM	Full Width at Half Maximum
G2	Diglyme
G4	Tetraglyme
HOMO	Highest Occupied Molecular Orbital
HRTEM	High-Resolution Transmission Electron Microscopy

LATP	$\text{Li}_{1.5}\text{Al}_{0.5}\text{Ti}_{1.5}\text{P}_3\text{O}_{12}$
LE	Liquid Electrolyte
LIB	Li-Ion Battery
LLZO	$\text{Li}_7\text{La}_3\text{Zr}_2\text{O}_{12}$
LSV	Linear Sweep Voltammetry
LUMO	Lowest Unoccupied Molecular Orbital
NaFSI	Sodium Bis(fluoro sulfonyl)imide
NASICON	NA Super Ionic CONductor
NaTFSI	Sodium Bis(trifluoromethyl sulfonyl)imide
NMP	N-Methyl-2-Pyrrolidone
NYS	$\text{Na}_5\text{YSi}_4\text{O}_{12}$
NYZS	$\text{Na}_{4.92}\text{Y}_{0.92}\text{Zr}_{0.08}\text{Si}_4\text{O}_{12}$
PC	Propylene Carbonate
PEO	Polyethylene Oxide
PITT	Potentiostatic Intermittent Titration Technique
PVDF	Polyvinylidene Fluoride
RT	Room Temperature
SEM	Scanning Electron Microscopy
SHE	Standard Hydrogen Electrode
SIB	Na-Ion Battery
SSB	Solid-State Battery
SSE	Solid-State Electrolyte
SS-NMR	Solid-State Nuclear Magnetic Resonance
SSSB	Solid-State Sodium (Na) Battery

TEM	Transmission Electron Microscopy
TGA	Thermogravimetric Analysis
TMS	Tetramethylsilane
XPS	X-ray Photoelectron Spectroscopy
XRD	X-ray Diffraction

I. Introduction

Solid-state batteries (SSBs) are considered one of the most promising energy storage technologies due to their high energy density, improved safety, and longer cycle life compared to conventional liquid electrolyte batteries.[1] However, the development of SSBs is hampered by the lack of suitable solid-state electrolytes (SSEs) with high ionic conductivity and stability as well as easy integration in cells.[2] In recent years, $\text{Na}_5\text{YSi}_4\text{O}_{12}$ -type (NYS) Na^+ superionic conductors have emerged as promising candidates for SSEs in solid-state Na batteries (SSSBs) due to their unique crystal structure that allows for the 3D diffusion of Na^+ ions, leading to high ionic conductivity.[3] In addition, the superior chemical and electrochemical stability, tolerable cost and facile preparation make NYS promising for production on a large scale.[4, 5]

The present thesis entitled “ $\text{Na}_5\text{YSi}_4\text{O}_{12}$ -type Na^+ superionic conductors for solid-state batteries” is focused on exploring the potential of NYS-type Na^+ superionic conductors as SSEs in SSBs, including both component manufacturing and exploration of novel compositions. The research in this thesis is divided into three parts.

The first part (**Chapter IV**) focuses on the fabrication of thin sheets of NYS using the tape-casting method with aqueous slurry.[4] This study aims to develop a scalable and cost-effective method for the production of thin, dense and robust NYS sheets, and investigate their electrochemical performance. The thin NYS sheets are crucial for the development of high-performance SSBs as they can maintain a relatively high ionic conductivity and guarantee the claimed high specific energy and low cost due to the less amount of the electrolyte in the full cells.

The second part (**Chapter V**) deals with the development of pressureless all-solid-state Na/S batteries with a self-supporting NYS scaffold.[6] The target is to demonstrate the feasibility of using NYS as an SSE in all-solid-state Na/S batteries. The self-supporting NYS scaffold is fabricated using the tape casting method, and the Na/S full cell is assembled and characterized using various electrochemical techniques. This work has shown the viability of the solid-state Na/S batteries operating at room temperature (RT) without external pressure.

The third part (**Chapter VI**) investigates the enhancement of Na^+ ionic conductivity in $\text{Na}_{4.92}\text{Y}_{0.92}\text{Zr}_{0.08}\text{Si}_4\text{O}_{12}$ (NYZS) at RT by partially substituting Y with Zr.[7] This improvement of ionic conductivity in NYS-type Na^+ superionic conductors is crucial for the practical application of SSBs. The optimized composition NYZS shows the highest RT Na^+ ionic conductivity among all NYS-type electrolytes.

Overall, this doctoral thesis provides a comprehensive understanding of the properties and behavior of NYS-type Na⁺ superionic conductors and their potential for practical fabrication and application as SSEs in SSBs. The results of this work contribute to the development of more cost-efficient and reliable SSSBs, which have the potential to transform the field of energy storage.

II. Literature Review

2.1. Solid-state Na batteries

2.1.1. General introduction of batteries

A battery is a device that converts chemical energy contained within its active materials (AMs) directly into electric energy by means of electrochemical oxidation-reduction (redox) reactions.[8] This type of redox reaction involves the transfer of electrons and ions from one material (electrode) to another via an electric loop circuit. The basic components of a battery include two electrodes (a positive and a negative electrode) and an electrolyte. In addition to the core components, the separator (if the electrolyte is a liquid, a gel, or a fused salt), the casing and the electrode tabs are also indispensable.[9]

While the term battery is often used, the cell is the actual electrochemical unit to generate or store electric energy. To understand the differences between a cell and a battery, one should think of a battery as a module of cells connected in series, parallel, or both, depending on the desired output voltage and capacity.[9]

Batteries can be categorized into primary and secondary batteries. (1) Primary (disposable) batteries are used once and discarded, as the AMs are irreversibly charged after discharging. A typical example is the alkaline battery used for quartz clocks and flashlights. (2) Secondary (rechargeable) batteries can be discharged and recharged multiple times, as the AMs in both electrodes are reversible during the redox reaction.[10] Examples include the Li-ion batteries (LIBs) used for portable electronics (such as laptops and cellphones) and electric vehicles (EVs) and lead-acid batteries used for low-speed and medium-speed two-/three-wheelers.[11] All the batteries mentioned in this doctoral thesis refer to secondary batteries. All materials investigated here serve rechargeable batteries.

Although batteries are prevalent in our daily lives, their history is only about 200 years old.[12] **Figure 1** shows the history of different batteries. The concept was first described by the Italian scientist Alessandro Volta around 1799.[13] The voltaic pile used Zn and Cu for electrodes with brine-soaked paper for an electrolyte. This invention disproved the common theory that electricity could only be created by living beings. Then, the Daniel cell was invented in 1836.[14] The Daniell cell used a Cu pot filled with CuSO_4 solution, which was further immersed in an earthenware container filled with H_2SO_4 and a Zn electrode. The new cell solved the previous “ H_2 bubble” problem of the Voltaic pile, in which bubbles collected on the surface of the Zn electrodes, limited the reactions and pile’s lifespan. The Daniell cell’s potential became the basis unit for voltage, equal to 1 volt. In 1859, the Pb-acid battery was invented and marketed in around 1880.[8] The Pb-acid battery was the first rechargeable battery. Pb-acid batteries excel in two aspects: they are very low cost and they can supply high surge currents. This makes them suitable for automobile starter motors even with today’s technology. In 1862, the first Zn-C batteries were produced by a French scientist

George Leclanché.[15] The battery contains a Zn anode, an electrolyte of aqueous NH_4Cl solution, and MnO_2 mixed with C as the cathode. It provides an output voltage of 1.4 V. The name “Zn-C battery” is slightly misleading as it implies that C is acting as the oxidizing agent rather than the MnO_2 . The Ni-Cd battery (1898) is a type of rechargeable battery using $\text{NiO}(\text{OH})$ and metallic Cd as electrodes.[16] It has a terminal voltage during discharge of around 1.2 V which slightly decreases until nearly the end of discharge. The modern alkaline battery was invented in 1957 by Canadian engineer Lewis Urry in the 1950s.[12] Using Zn and MnO_2 in the electrodes, the battery type gets its name from the alkaline electrolyte used – KOH. Alkaline batteries are used in regular household devices from remote controls to flashlights, which are inexpensive and typically non-rechargeable.

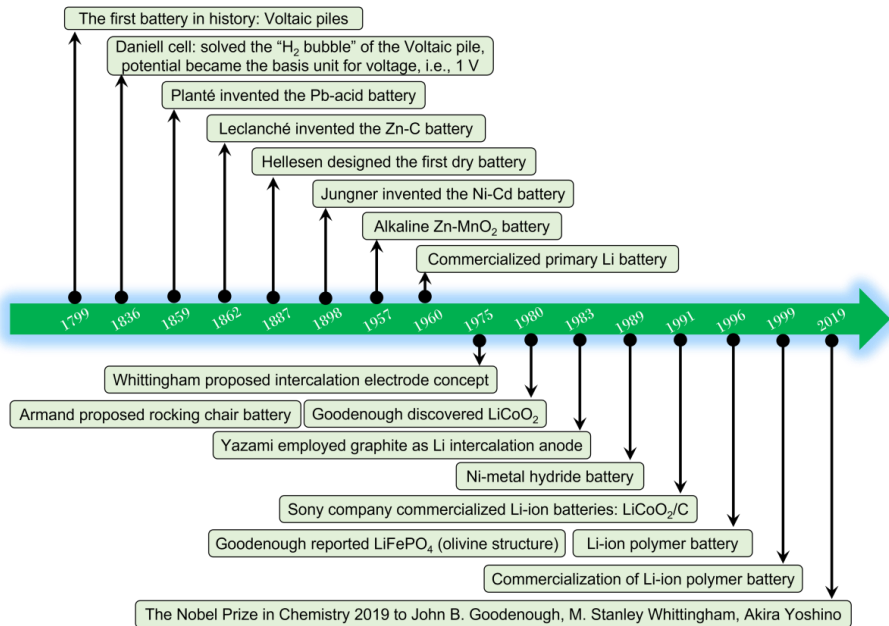


Figure 1 Overview of battery development milestones.

In comparison, lithium battery technology is actually very young. Michel Armand, Robert Huggins, and Stanley Whittingham investigated the insertion electrode reaction in the 1970s.[11] Stanley Whittingham investigated the combination of Li metal and TiS_2 to achieve a rechargeable Li battery based on the insertion reaction for rechargeable Li batteries.[17] In 1990, rechargeable Li metal batteries were abandoned from

the market due to safety concerns.[10] Subsequently, Sony introduced a LIB using graphite as the negative electrode and layered oxide as the positive electrode. The safety of this LIB has been significantly improved and is widely used today.[8] The Nobel Prize in Chemistry in 2019 stands as a testament to the monumental strides made in the field of energy storage and sustainability. Awarded jointly to John B. Goodenough, M. Stanley Whittingham, and Akira Yoshino, this prestigious honor recognizes their pioneering contributions to the development of LIBs.[18]

Whereas in chemical redox reactions, oxidation and reduction occur at the same site, in electrochemical reactions, oxidation and reduction are spatially separated, i.e., the redox reaction is split into two half-cell reactions. All electrochemical reactions follow two general principles: the law of charge conservation and Faraday's law of electrolysis. The electrochemical reaction allows the separation of electrons and ions in space, where the electrons move through the external circuit and the ions move through the electrolyte. Electrically neutral species separate electrons and ions at one of the electrodes and recombine them at the other.[19] The electrolyte needs to comply with the principle of electroneutrality, i.e., anions and cations bear the same amount but opposite charges:

$$\sum_i z_i c_i = 0 \quad (\text{Equation 1})$$

where i represents the charged species in the electrolyte, c and z represent the concentration of ion i and the number of charges it carries, respectively.

Faraday's law of electrolysis correlates the reaction rate with the current:

$$n_M = \frac{Q}{zF} \quad (\text{Equation 2})$$

$$F = eN_A \approx 1.602 \times 10^{-19} \times 6.022 \times 10^{23} \text{ C mol}^{-1} \approx 96485 \text{ C mol}^{-1} \quad (\text{Equation 3})$$

where n_M = the amount of substance M (number of moles, with the unit of mol), Q = amount of charge (in coulombs, with the unit of C), z = the amount of each species, F = Faraday constant ($1 F = 96485 \text{ C mol}^{-1}$), e = the elementary charge ($1.602 \times 10^{-19} \text{ C}$) and N_A = Avogadro constant ($6.022 \times 10^{23} \text{ mol}^{-1}$).

Under isothermal and isobaric conditions, when the system changes, the change of Gibbs free energy of the system should be equal to the non-volume work done by the system externally, i.e.,

$$\Delta_r G = W' = -nEF \quad (\text{Equation 4}) \text{ and}$$

$$E = \frac{-\Delta_r G}{nF} \quad (\text{Equation 5}),$$

where $\Delta_r G$ refers to the change of Gibbs free energy of the reaction, W refers to non-volume work, n refers to the number of electrons transferred in the reaction, E refers to the electric potential of the cell and F is the Faraday constant.

For the case where all reactants and products are in standard state, the electric potential of the cell is called “standard electric potential”, marked as E° , and defined by the equation

$$E^\circ = \frac{-\Delta_r G^\circ}{nF} \quad (\text{Equation 6}),$$

where G° refers to the change of the standard Gibbs energy of the electrochemical reaction.

Using the above thermodynamic bridge equation, we can find the value of the electromotive force of an electrochemical reaction. From the reaction kinetics, it follows that:

$$\Delta_r G = -RT \ln K \quad (\text{Equation 7}),$$

where R refers to the gas constant ($8.314 \text{ J K}^{-1} \text{ mol}^{-1}$) and K refers to the equilibrium constant. For a specific electrochemical reaction $aA + bB \rightarrow gG + hH$,

$$K = \frac{(\alpha_G)^g (\alpha_H)^h}{(\alpha_A)^a (\alpha_B)^b} \quad (\text{Equation 8}),$$

where α refers to the activities of different species in the reaction.

Therefore, the electric potential of the cell can be described as:

$$E = E^\circ - \frac{RT}{nF} \ln K \quad (\text{Equation 9}),$$

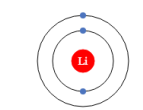
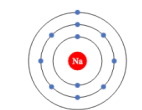
which is the well-known Nernst equation.[20]

2.1.2. Li- vs. Na-based batteries

2.1.2.1. Comparison of Li and Na physical and chemical properties

Lithium (Li) and sodium (Na) are both alkali metals and share many physical and chemical properties. However, there are some critical differences between the two elements. A systematic comparison between them is shown in **Table 1**.

Table 1 Comparison of Li and Na elements' physical and chemical properties.

Property	Li	Na	Remarks
Electronic shell configuration	<p>3: Lithium</p>  <p>[He] 2s¹ [2, 1]</p>	<p>11: Sodium</p>  <p>[Ne] 3s¹ [2, 8, 1]</p>	Both have one valence electron; Na is more prone to lose its outer electron due to its weak attraction.
Ionic radius/Å	0.76	1.02	Na ⁺ ions are larger than Li ⁺ ions.
Melting point/°C	180.54	97.72	Na metal has a lower melting point compared with Li, which is energy-conserving when melting the metal. However, Na poses a potential threat at temperatures above its melting point.
Abundance in earth's crust by weight	0.002%	2.3%	The abundance of Na in the earth's crust is 1200 times greater than that of Li.
Absolute abundance in the earth's crust	20 mg kg ⁻¹	23600 mg kg ⁻¹	
Abundance in oceans by weight	0.000018%	1.1%	The abundance of Na in the ocean is more than 60000 times greater than that of Li.
Electronegativity (EN) based on the Pauling scale	0.98	0.93	Li and Na are Group I elements with decreasing EN as the radius increases from a top-down position.
Mohs hardness/MPa	0.6	0.5	Na metal is softer and easier to be rolled into thin layers than Li metal.
Young's modulus/GPa	4.9	10	Na metal is stiffer than Li metal.
Environmental stability	Li metal can be highly reactive with the main components of air (N ₂ , O ₂ , CO ₂ , H ₂ O).	Na metal reacts aggressively with H ₂ O and can react with O ₂ .	The storage and processing of both Li and Na metals require an H ₂ O and O ₂ -free environment, and Li needs to be stored without N ₂ .

Thermal conductivity/ $W\ m^{-1}\ K^{-1}$	85	140	Na metal has a higher thermal conductivity than Li metal, i.e., Na metal has a better heat transfer capability.
Electrochemical equivalent (EQ)/ $g\ A^{-1}h^{-1}$	0.2589	0.8579	Li metal shows a lower EQ value due to its low weight.
Reduction potential vs. SHE/V	-3.04	-2.71	Li metal has the lowest potential among all materials. The potential of Na metal is 0.33 V higher than Li.
Theoretical capacity C_{th} based on Li (Na)/ $mAh\ g^{-1}$	3860	1166	The theoretical capacity of Li metal is more than three times that of Na metal.

Electronegativity (EN): refers to the ability of an atom to attract shared electrons in a covalent bond. The higher the value of the EN, the stronger that element attracts the shared electrons in the bond.

SHE: standard hydrogen electrode.

(1) Electronic shell configuration:

Li and Na are alkali metals with similar chemical properties due to their single valence electron in their outermost shell. The electron configuration of Li is $1s^2 2s^1$, meaning it has two electrons in its innermost shell and one electron in its outer shell. The electron configuration of Na is $1s^2 2s^2 2p^6 3s^1$, indicating that it has a full innermost shell and one valence electron in the 3s orbital. Therefore, while both elements have similar valence electron configurations, Na has additional electrons in its inner shells, which affects its reactivity and chemical properties. Na has a larger atomic radius and is more reactive than Li due to its weaker attraction between the nucleus and valence electrons.[21]

(2) Ionic radius:

The ionic radius of Na^+ is larger than that of Li^+ due to the additional inner electrons, which increases the shielding effect and reduces the attraction between the nucleus and the outermost electron shell.[22] The ionic size significantly influences the transport of ions in liquids and solids.

In liquids, the mobility of ions is primarily determined by their size and charge. Larger Na^+ ions tend to move more slowly through a liquid than smaller Li^+ ions because they experience more frictional drag from the surrounding solvent molecules. This is known as the Stokes-Einstein relationship (Eq. 10), which states

that the rate of diffusion of a particle is inversely proportional to its size.[23] The diffusion of spherical particles through a liquid follows the Stokes-Einstein equation:

$$D = \frac{k_B T}{6\pi\eta r} \quad (\text{Equation 10}),$$

where D is the diffusion coefficient; k_B is the Boltzmann constant ($8.314 \text{ J K}^{-1}\text{mol}^{-1}$); T is the absolute temperature; η is the dynamic viscosity and r is the radius of the diffusing ion.[23]

Different from liquids, the transport of ions in solids is mainly determined by the nature of the crystal lattice (such as its crystal structure and the presence of defects or impurities), as in the case of solid-state ionic conductors.[24] The size and charge of the ions themselves also influence the ionic diffusion in solids. Larger ions may be hindered by the smaller interstitial spaces between lattice sites, while smaller ions may diffuse more quickly through the lattice because they can move more easily between lattice sites. However, a proper steric geometry (i.e., size of bottlenecks) and a short distance between two adjacent sites are more crucial for ionic transportation in solids.[25] The charge of the ion can also affect its mobility, as ions with larger charges may be more strongly attracted to lattice sites and move more slowly than ions with smaller charges. Therefore, ionic diffusion in solids is determined by a complex interplay of factors, which needs to be considered when optimizing ionic conductors.[26]

(3) Melting point:

The melting point of Na metal is lower than that of Li metal. The reason for this difference is due to the size of the atoms and the strength of the metallic bonds.[27] Li has a smaller atomic radius than Na, meaning the metallic bonds between the atoms are strong. Therefore, more energy is required to break these bonds and melt the metal, resulting in a higher melting point. In contrast, Na has a larger atomic radius and weaker metallic bonds, which makes it easier to melt. Na metal can be processed at a lower temperature than Li, which reduces the energy and cost required for manufacturing.[28] This can be especially beneficial in large-scale battery production. However, when applied to batteries, the melting of the metal poses a safety issue when the temperature is close to its melting point. This needs to be taken into account when designing the battery temperature management system.

(4) Abundance:

Li is not only much less abundant than Na on earth but also very concentrated in its distribution. The main sources of Li are currently brine deposits in South America and hard rock mines in Australia, China, and Canada.[29] While Li reserves are sufficient to meet current demand, there are concerns about the environmental impact of Li mining and the potential for supply constraints in the future. Na, on the other hand, is one of the most abundant elements on earth and is widely available in seawater, rocks, and minerals.

Na can be extracted from seawater using relatively simple and low-cost methods, which makes it a more sustainable and cost-effective option for large-scale energy storage applications.[27]

(5) Mechanical properties:

Young's modulus of Na is higher than that of Li. Specifically, Young's modulus of Na is approximately 10.0 GPa, while Young's modulus of Li is approximately 4.9 GPa.[30] This means that Na is stiffer and more resistant to deformation under stress than Li. The difference in Young's modulus between the two metals is due to their atomic and crystal structures. Na has a body-centered cubic crystal structure, while Li has a face-centered cubic structure, which affects the way the atoms are arranged and bonded together. The yield strength of bulk polycrystalline Li is between 0.4 and 0.9 MPa,[31] while the yield strength of Na metal is 0.19 ~ 0.28 MPa.[32] When studying metal dendrites in SSBs, these values cannot reflect the true resistance to dendrites, although the yield strengths of both appear to be much lower than those of most SSEs. Zhang et al. have measured the yield strength of Li whisker (i.e., Li dendrite) with an atomic force microscope and found that ranges from 12.2 to 244 MPa, two orders of magnitude higher than that of bulk Li.[33] Both Li and Na are relatively soft and malleable metals that can be processed into thin metal anode sheets. Wang et al. showed an example of the fabrication of a processable and moldable Na-metal anode made from Na and reduced graphene oxide (r-GO, 4.5 wt%), which was employed in both Na/O₂ and Na/Na₃V₂(PO₄)₃ full cells.[34]

(6) Thermal conductivity:

Both Li and Na metals have relatively high thermal conductivities, but Na has a higher thermal conductivity than Li. The high thermal conductivity of Na can not only help to distribute heat evenly throughout the battery pack but also dissipate heat during battery operation to prevent localized overheating.[35]

(7) Electrochemical equivalent (EQ):

It refers to the mass of a chemical element (in grams) transported by 1 Coulomb of electron charge. The formula for calculating EQ is:

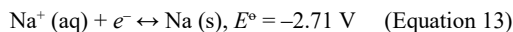
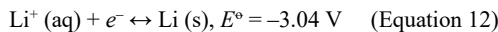
$$EQ = \frac{M}{q} = \frac{M}{It} \quad (\text{Equation 11}),$$

where M is the mass of the substance, q is the charge passed, I is the applied current and t is the time. The EQ values of Li and Na are 0.2589 and 0.8579 g A⁻¹h⁻¹, respectively. This suggests that in an electrochemical reaction, 3.3 times the mass of Na metal needs to be consumed as compared to Li metal for the same amount of charge transferred.[36]

(8) Reduction potential comparison of Li⁺/Li and Na⁺/Na:

The higher reduction potential of Na leads to a lower voltage output and energy density of Na-ion batteries (SIBs) compared to LIBs, but SIBs can still provide a useful source of energy for applications that do not require high energy densities.[29]

However, it is important to point out that the electrode potential was determined in an aqueous solution and is related to the hydration energy (solvation energy) of the metal ion. The half-reactions of Li and Na are as follows:



Li ions have a smaller radius and a larger hydration energy than those of other alkali metals. Therefore, Li exhibits the lowest reduction potential.

(9) Theoretical capacity C_{th} :

The theoretical specific capacity of a metal anode is the maximum amount of charge (measured in coulombs) that can be stored per unit mass (measured in grams) of the metal.[21] For Li and Na metal anodes, the theoretical specific capacity can be calculated using the following equations:

$$C_{th}(\text{Li}) = \frac{nF}{3.6M_w} = 3860 \text{ mAh g}^{-1} \quad (\text{Equation 14})$$

$$C_{th}(\text{Na}) = \frac{nF}{3.6M_w} = 1166 \text{ mAh g}^{-1} \quad (\text{Equation 15})$$

where n is the transferred electrons (herein is 1); F is Faraday's constant and M_w is the molecular weight.

2.1.2.2. Comparison of LIBs and SIBs

After comparing the differences between Li and Na elements, it is necessary to compare and analyze the components of LIBs and SIBs.

(1) LIBs

For LIBs, the continuous pursuit of high-specific energy and high-safety battery systems has contributed significantly to the development of battery materials and the knowledge of battery failure mechanisms.[37] The evolution of the negative electrode, positive electrode and electrolyte materials for LIBs is presented in **Figure 2**. [37] In the case of the negative electrode materials, Li metal is expected to be the most desirable choice (having the highest specific capacity of 3860 mAh g⁻¹ and the lowest electrode potential of -3.04 V

vs. SHE).[38] However, the electrode potential of Li^+/Li is higher than the lowest unoccupied molecular orbitals (LUMO) of conventional non-aqueous electrolytes, which means that both will constantly react and consume Li metal and electrolyte unless a stable passivating layer, the so-called solid electrolyte interphase (SEI) is formed. In addition, the formation of Li dendrites and volume changes during charging and discharging can cause battery performance degradation, even short-circuit and thermal runaway.[39] Moli Energy's batteries with Li metal negative electrodes caused a series of fire accidents that were the last straw that killed the camel.[13] To avoid safety hazards, Armand suggested two different intercalation hosts as electrode materials to construct LIBs.[40] Graphite with a layered structure is an excellent choice. Although the theoretical specific capacity of graphite (372 mAh g^{-1} based on LiC_6) is far inferior to that of Li metal, the layered structure of graphite has half-filled p_z orbitals perpendicular to the plane that interact with the $2s$ orbitals of Li to limit volume expansion and dendrite growth.[41]

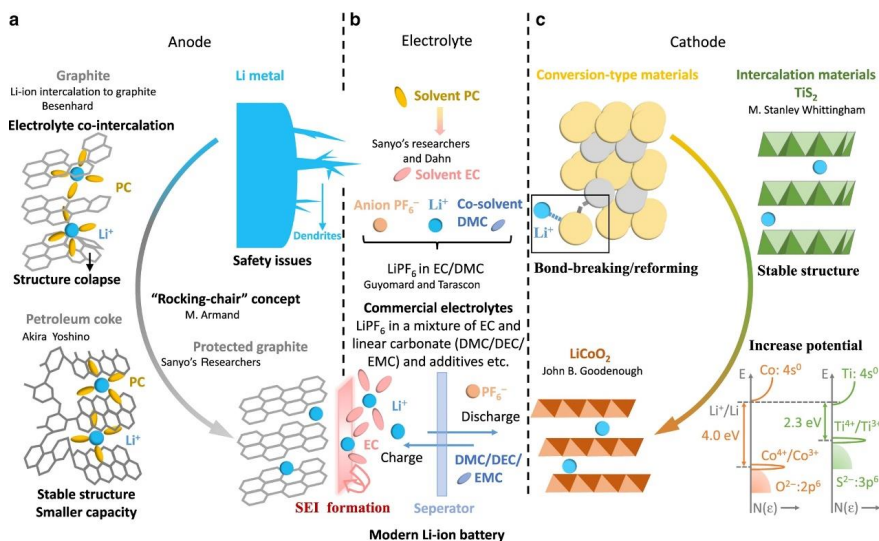


Figure 2 Milestone discoveries that shaped the modern LIBs.

The development of (a) anodes, including Li metal, petroleum coke and graphite, (b) electrolytes with the solvent propylene carbonate (PC), a mixture of ethylene carbonate (EC), linear carbonates selected from dimethyl carbonate (DMC), diethyl carbonate (DEC), ethyl methyl carbonate (EMC) and additives, (c) cathodes including conversion-type materials, intercalation materials TiS_2 and LiCoO_2 .

(Reproduced with permission from ref.[37].)

Initially, positive electrode materials such as sulfides, oxides, or metal fluorides based on conversion reaction mechanism were explored to match the Li metal negative electrode.[42] However, these materials were always accompanied by irreversible secondary phase formation during the battery cycling process, which severely limited the cycling life of the battery.[43] Subsequently, the trend of cathode materials shifted to metal chalcogenides (MX_2). TiS_2 does not undergo structural collapse, but the voltage of the full cells of around 2.5 V cannot meet the demand for high specific energy.[44] Goodenough reported LiCoO_2 with a layered structure exceeding 4 V (vs. Li^+/Li).[45] LiMn_2O_4 with spinel structure was also found, and Li ions with tetragonal sites exhibited an electrode potential of ~ 4 V (vs. Li^+/Li) and lower cost.[46] Polyanionic oxides, represented by LiFePO_4 , have further gained much attention due to the use of inexpensive transition metal elements, improved cycle life and thermal stability.[47]

In addition to the requirement for high ionic conductivity and electronic insulation of the electrolyte, a sufficiently wide electrochemical stability window is a prerequisite for cell operation.[48] The working window of an electrolyte depends on the LUMO and the highest occupied molecular orbital (HOMO), where LUMO should be higher than the potential of the anode ($\mu_{e^-, \text{Anode}}$) and HOMO lower than the potential of the cathode ($\mu_{e^-, \text{Cathode}}$), i.e. ($\text{LUMO} > \mu_{e^-, \text{Anode}}$; $\text{HOMO} < \mu_{e^-, \text{Cathode}}$) (see **Figure 3**).[49] Primarily, the initial studies favored propylene carbonate (PC) due to its lower melting point (-48.8 °C) compared to ethylene carbonate (EC) (36.4 °C). Afterward, Dahn showed that EC could facilitate the formation of stable SEI and thus inhibit the exfoliation of graphite,[50] so nowadays, PC-EC solvent mixture is often used as an electrolyte.

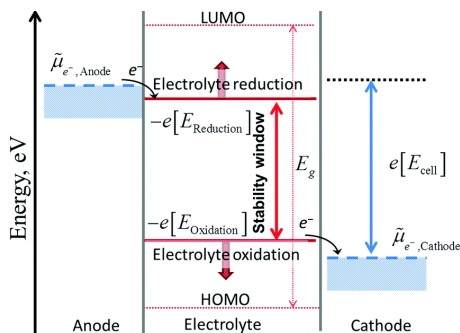


Figure 3 Correct notation for the negative and positive potential limits for the electrolyte stability and the energy levels of HOMO and LUMO.

(Reproduced with permission from ref.[49].)

(2) SIBs

The electrochemical mechanism of SIBs is not different from that of LIBs, so the research and development of SIBs can be directly adapted and employed in most LIBs.[22] Research on SIBs can be traced back to the 1970s and 1980s.[51, 52] With the release of commercial LIBs in the 1990s, research on SIBs was put on hold for a long time.[53] This is mainly due to the fact that the atomic weight of Na is larger than that of Li and the operating voltage is low, and the mass and volume-specific energy density of SIBs is significantly lower than that of LIBs.[54] Generally speaking, the battery performance and cost of both SIBs and LIBs depend largely on the cathode materials, so it is crucial to develop low-cost and high-performance cathode materials.[55] As shown in **Figure 4**,[56] the cathodes of SIBs mainly consist of layered oxides (such as α -NaMnO₂, Na_{0.67}Mn_{0.95}Mg_{0.05}O₂, Na_{0.67}Mn_{0.65}Fe_{0.2}Ni_{0.15}O₂), polyanionic compounds (such as Na₃V₂(PO₄)₃, Na₃V₂(PO₄)₂F₃, Na₂Fe(SO₄)₃), alkali-rich materials (such as Na₃FeO₄) and amorphous materials (such as amorphous V₂O₅).[57] The anode materials differ from LIBs in that hard carbon, soft carbon, TiO₂, Na₂Ti₃PO₄, or alloying or/and conversion materials are used.[56] The solvent used in the electrolyte (EC, DMC, PC, FEC, glymes) is not different from LIBs, except that the Li-containing salt is replaced by Na-containing salt (NaPF₆, NaClO₄, NaTFSI, NaFSI).[55]

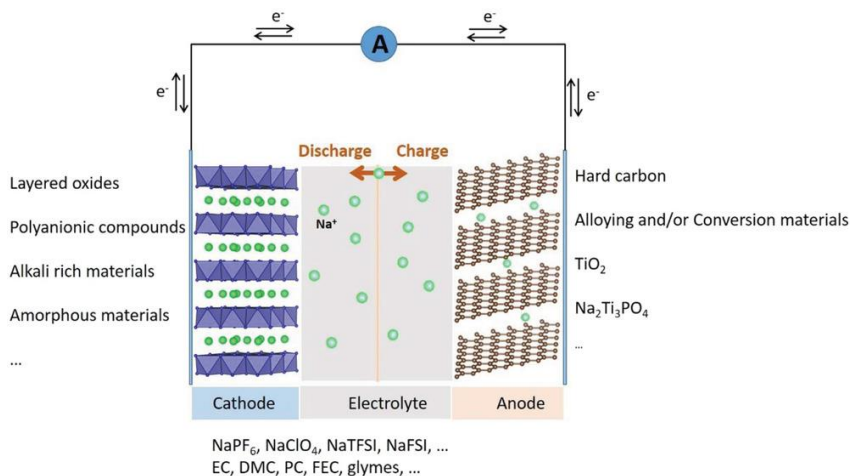


Figure 4 Illustration of a SIB system.

(Reproduced with permission from ref.[56].)

In addition to the above-mentioned inorganic positive electrode materials, sulfur (S) is an attractive class of positive electrode materials due to its ultra-high specific capacity (1675 mAh g⁻¹ based on the S mass and discharge product of Na₂S), high resource abundance and low cost.[58]

Constrained by the low specific capacity of conventional cathode materials, Li/S and Na/S batteries using liquid organic electrolytes have been increasingly reported in the past decade.[59] However, in the battery system with liquid electrolytes, S and Na_xS (0 ≤ x ≤ 2), the discharge products of different stages, lead to self-discharge and poor cycling performance due to severe dissolution in the electrolyte.[60, 61] Wang et al. fabricated a three-dimensional carbon host to accommodate S and the discharge products to mitigate the dissolution and better cycling performance was obtained.[62] Yan et al. also introduced a conductive network of N-doped porous carbon nanotube hollow cages in Na/S batteries, endowing it with superior conductivity in both short- and long-range and strong polarity toward polysulfides.[63] Although high-temperature-based Na/S batteries have been used in grid-level scale energy storage,[64] the potential safety concerns associated with molten Na metal and S at high temperatures should not be underestimated. In high-temperature Na/S batteries, the SSE as the separator and ion transport media is the most essential component and β/β''-Al₂O₃ is the most common electrolyte material.[65] Therefore, designing solid-state Na/S batteries operating at RT can not only avoid the dissolution issues of S and polysulfides but also dramatically improve practical safety.[66] Hegde et al. synthesized a NASICON/polymer composite electrolyte and constructed an RT-operating Na/S battery although the specific capacity of S is only 300 mAh g⁻¹. [67]

2.1.2.3. Cost and sustainability analysis

From the cost perspective, the cost advantage of SIBs mainly stems from the fact that the cost of Na-containing raw materials is much lower than that of Li-containing materials in LIBs.[68] The market price of carbonates, for example, is 70000 Euros per metric ton for Li₂CO₃ in 2022, while the price of Na₂CO₃ is only 220 Euros per metric ton. The price of Li₂CO₃ is more than three hundred times higher than that of Na₂CO₃ in the same period.[68, 69] However, it is unfair to benchmark the cost of batteries based on the specific gravimetric price of the raw materials.[70] This is because Li and Na cannot carry equal amounts of charges per unit mass. In **Table 1**, the electrochemical equivalents of Li and Na are 0.2589 and 0.8579 g A⁻¹h⁻¹, respectively, which suggests that 3.31 times the mass of Na can provide the same charges as Li.

Except for the cost of Li/Na-contained raw materials, the cost of cathodes also accounts for a significant portion of the battery.[71] As illustrated in **Figure 5**, the composition of common cathodes in LIBs and

SIBs has been listed.[55] Cheaper transition metal elements (like Mn, Fe and V) can be utilized for the cathode of SIBs.

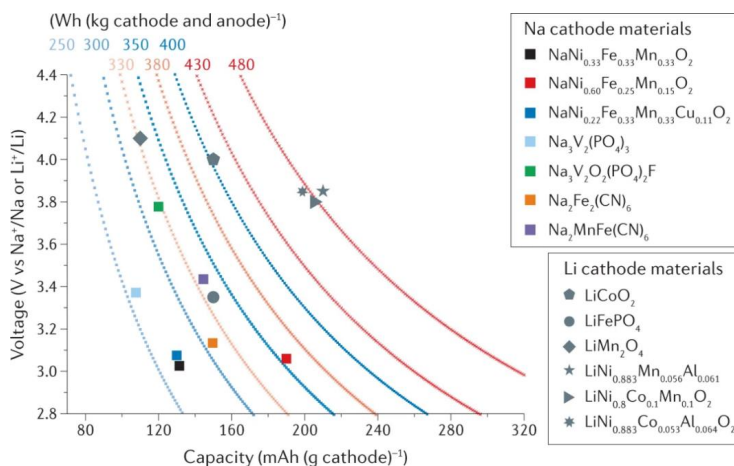


Figure 5 Specific energy of LIBs and SIBs based on different cathodes.

Average discharge voltage and capacity of various cathode materials. The predicted specific energy of full cells at a low discharge rate ($C/10$) is shown using curves of constant specific energy, assuming that the anode is hard carbon for Na batteries (blue curves, average 0.3 V versus Na^+/Na , 400 mAh g^{-1}) or graphite for Li batteries (red curves, 0.15 V versus Li^+/Li , 360 mAh g^{-1}). The curves are calculated based on the ideal cathode: anode active mass ratio and normalized by the total active mass in both electrodes.

(Reproduced with permission from ref.[55].)

In addition to the low-cost advantage of Na-containing raw materials, Al foil can be used as a current collector for the positive and negative electrodes of Na-based batteries.[72] In LIBs, Cu is used on the anode side due to the fact that Al will alloy with Li at low potentials (e.g., 0 V for Li metal and 0.2 V for negative graphite electrodes).[73] The lattice vacancies of octahedral metallic Al are similar in size to Li atoms, which makes it easy to form interstitial metal compounds with Li.[74] Li and Al form not only an alloy with the formula LiAl but also possibly Li_3Al_2 or Li_4Al_3 . [75] Cu can be used as a current collector for the negative electrode of LIBs because it has a negligible capacity for Li^+ ions and maintains a stable structure and electrochemical performance.[74] However, due to the larger ionic radius of Na atoms, Na does not

alloy with Al, thus ensuring stability during deposition. Therefore, in Na-based batteries, the current collector for positive and negative electrodes can be an Al foil, which is more cost-effective.[76]

2.1.2.4. Summary: not substitution but supplementation

Different application scenarios have different requirements for battery performance, cost and other factors that are the result of trade-offs. LIBs have obvious advantages of high specific energy and long cycling life in the fields of electric vehicles and portable devices.[77] However, considering the limited resources and gradually increasing raw material costs of LIBs, SIBs are a suitable supplement in the field of stationary energy storage and electric bicycles.[78] The cheap and easily available sodium resources ensure the application of Na batteries on a large scale.

2.1.3. Liquid- vs. solid-state batteries

2.1.3.1. From liquid to solid: configuration

The evolution of battery configuration from liquid-state batteries to SSBs has been driven by the need for improved safety, higher energy density and longer cycling life of energy-storage systems.[37] Although LIBs with organic liquid electrolytes dominate the current market, the specific capacity of LIBs based on graphite anode and cathode materials such as LiFePO_4 , LiMn_2O_4 , LiCoO_2 , $\text{LiNi}_x\text{Co}_y\text{Mn}_z\text{O}_2$ (NCM_{xyz}, $x + y + z = 1$), with the intercalation reaction mechanism approaching the capacity limit.[43] After shifting from a liquid electrolyte system to an SSE system, it is expected to reduce the mass fraction of electrolytes in the battery with the fabrication of thinner SSEs,[79] simplify the full cell configuration, and match the high-voltage cathode and metal anode to achieve a better system with higher specific energy.[80]

The basic configuration of a battery – the positive electrode, the negative electrode and the electrolyte – remains unchanged from a conventional liquid electrolyte battery to a solid electrolyte battery.[81] As shown in **Figure 6a**, the change in structure can be considered as liquid solidification.[72] This means that not only is it necessary to find a solid electrolyte material that is superior in conducting only ions and not electrons, but it is also required to solve the problem of good interfacial contact between the electrolyte and the electrode, which is more challenging for a solid electrolyte compared with a liquid electrolyte that can flow.[82] In addition, the arrangement of the cells in the solid-state pack can be more flexible and compact (**Figure 6b**).[83] The step of liquid injection is avoided during the preparation of the cells.

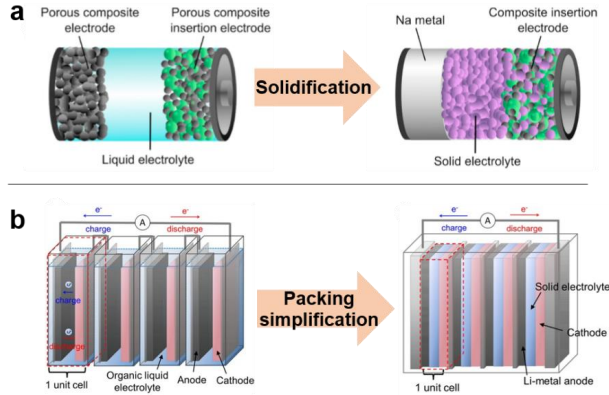


Figure 6 The cell configuration changes from liquid to solid system.

(a) Schematic cell configuration of the most common types of Na-based batteries. Left: SIB; right: SSSB with Na metal as the negative electrode. (b) Schematic of conventional stacked Li-ion battery using a liquid electrolyte (left) and bipolar stacked all-solid-state battery (right).

(a: Reproduced with permission from ref.[72]. b: Reproduced with permission from ref.[83].)

In an SSSB, Na metal is one of the ideal anode candidates and is mostly used as a Na foil having a thickness of several tens of micrometers and cut into a proper size.[84] It is, however, necessary to pay special attention to the storage and handling of Na metal. Na readily reacts with moisture and oxygen in the ambient atmosphere to form sodium oxide and sodium carbonate.[85] Therefore, a moisture-free and oxygen-free atmosphere is required in the full cell production processes if Na metal is adopted as the anode.[86]

For large-scale and continuous manufacturing, advanced fabrication techniques should be developed.[86] As shown in **Figure 7**, a production process designed for SSBs based on the adaptation of a well-established preparation process for existing LIBs cells is proposed.[87] The continuous preparation of the cells is achieved by sequential coating and drying the solid electrolyte and coating and drying the solid electrodes. After the cells are prepared, they are cut and stacked to assemble the pouch cell pack as required. Although this concept is perfectly compatible with existing LIB production lines,[88] it is only applicable to polymer-based or partially polymer-containing flexible electrolyte systems.[89] However, for rigid oxide ceramic electrolytes with good chemical and electrochemical stability and high ionic conductivity, further development of suitable scale-up production lines is required.[4, 6]

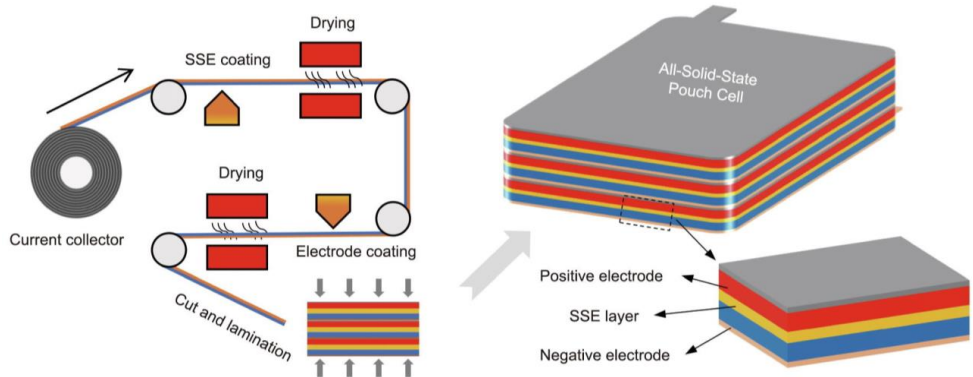


Figure 7 A slurry coating process to fabricate practical multilayer all-solid-state pouch cells.

The continuous production processes consist of SSE slurry coating and drying, electrode coating and drying, layer cutting and lamination, then packing and sealing of the all-solid-state pouch cells.

(Reproduced with permission from ref.[87].)

2.1.3.2. Comparison of liquid and solid electrolytes for Na batteries

The functionality of both conventional liquid electrolytes and solid electrolytes in a battery is to connect the transport of ions on both sides of the positive and negative electrodes while blocking electrons.[25] The solid electrolyte plays the role of ion pathway as well as replacing the traditional separator.[90] Taking Na⁺ ion electrolytes as an example, we compare the difference (**Table 2**) between liquid electrolytes and solid electrolytes and analyze their advantages and disadvantages.

Table 2 Comparison between liquid and solid electrolytes for Na-based batteries.

Property	Liquid electrolyte	Solid electrolyte	Remarks
General composition	Sodium salt in organic solvent (salt: NaClO ₄ , NaPF ₆ , NaBF ₄ , NaTFSI. solvent: cyclic carbonate: PC, EC; chain carbonate: DEC, DMC, EMC; chain ether: G2, G4)	Oxides: Na ₃ Zr ₂ Si ₂ PO ₁₂ , Na-β/β"-Al ₂ O ₃ , NYS; sulfides: Na ₃ PS ₄ , Na ₁₁ Sn ₂ PS ₁₂ ; polymer composites: PEO + NaTFSI + Na-β"-Al ₂ O ₃	There are different combinations of sodium salts and organic solvents for liquid electrolytes. The different classes of solid electrolytes vary widely.

Ionic conductivity at RT	5 ~ 15 mS cm ⁻¹	0.01 ~ 10 mS cm ⁻¹	σ (most SSEs) \ll σ (liquid electrolytes).
Electronic insulation	$< 10^{-7}$ mS cm ⁻¹	$< 10^{-8}$ mS cm ⁻¹	Both can meet the criteria.
Electrochemical stability	1 ~ 3.5 V vs. Na ⁺ /Na	Oxide electrolytes: ≥ 5 V; polymer composites/sulfides: ≤ 4 V (vs. Na ⁺ /Na)	SSEs have the significant advantage of wide electrochemical stability.
Transference number of Na ⁺ ions	≤ 0.4	Inorganic electrolytes: ≈ 1 ; polymer-based composite: 0.2 ~ 0.4	The anions in liquid and composite electrolytes contribute significantly to the transference numbers.
Interfacial contact with electrodes	Very good due to the fluidity	Very hard, especially the robust oxide ceramic electrolytes	-
Operating temperature	-20 ~ 60 °C	PEO-based composites: 60 ~ 85 °C; inorganic electrolytes: ≥ 0 °C	Usually, the higher the temperature, the better the performance of inorganic electrolytes within the safety range.
Environmental impact	Toxic (especially, fluorides)	The sintering process is energy-consuming.	-
Fabrication process	Easy	Complicated for oxides and easy for polymers	Depends on the technology roadmap and scaling level.
Cost	Due to the massive production and compatibility with the established LIBs, the cost is not high	Relatively high due to the sintering process	The cost of SSEs can be further reduced once they are prepared on a large scale and can be prepared as ultra-thin sheets.
Leakage	Yes	No	-
Safety	Thermal runaway; explosion concern	Very high safety (Except for Na/S batteries, etc. with SSEs operating at high temperatures)	SSEs have a significant advantage with improved safety.

(1) Comparison of electrochemical properties:

The conductivity of an electrolyte is one of the most important parameters for the evaluation of electrolytes.[72] Besides a few reported sulfide electrolytes,[91, 92] the conductivity of most solid electrolytes cannot compete with that of liquid electrolytes. Moreover, there are severe compatibility issues between SSEs and electrodes. Therefore, the absence of electrolyte materials with high ionic conductivity and the lack of a viable and robust electrode/electrolyte interface are the two main challenges for SSBs.[7]

However, the electrochemical stability window of SSEs, especially oxide electrolytes, is much better than that of liquid electrolytes,[4, 7] which is one of the considerations why SSBs are regarded as next-generation batteries. A sufficiently wide electrochemical stability window makes it possible to use cathodes with higher potential and Na metal as the anodes, which are expected to break the upper limit of the specific energy of current LIBs.[81]

(2) Safety:

SSBs essentially eliminate the safety concerns (thermal runaway, short-circuit caused by dendrites, etc.) associated with conventional LIBs using organic liquid electrolytes.[93] Good electrochemical stability ensures the safety and reliability of the battery during operation, unlike the irreversible capacity loss caused by the continuous decomposition of the liquid electrolyte at high voltages or by the direct chemical reaction with the electrode materials.[94]

(3) Perspectives:

As shown in **Figure 8**, the SSBs (top right) outperform the current LIBs (bottom left) in terms of specific energy ($E > 10^2 \text{ Wh kg}^{-1}$) and specific power ($P > 10 \text{ kW kg}^{-1}$), which is what we are pursuing.[95] However, it must be realized that high-specific energy and high-specific power SSBs require not only electrolyte materials with higher conductivity and better stability but also the development of scalable manufacturing processes of SSEs to prepare thinner and robust electrolyte layers.[96] But it has to be noted that here sulfides were used, having higher conductivity than liquids.[91, 97] Otherwise, the SSBs would not be at the top right.[98] It is worth pointing out that the Li/S battery system in the lower right of **Figure 8** exhibits very high specific energy, which is attributed to the ultra-high specific capacity of Li storage in S. S also exhibits excellent ultra-high specific capacity and specific energy in Na storage. Although the Na/S battery system is not indicated in **Figure 8**, it should be located to the left of the Li/S battery system in the context of the reported performance of Na/S batteries[99] and the performance of solid-state Na/S batteries in **Chapter 5** of this thesis.[6] The specific energy range for this system falls between 10^2 and 10^3 Wh kg^{-1} and the specific power falls between 10^{-1} and 10^2 kW kg^{-1} .

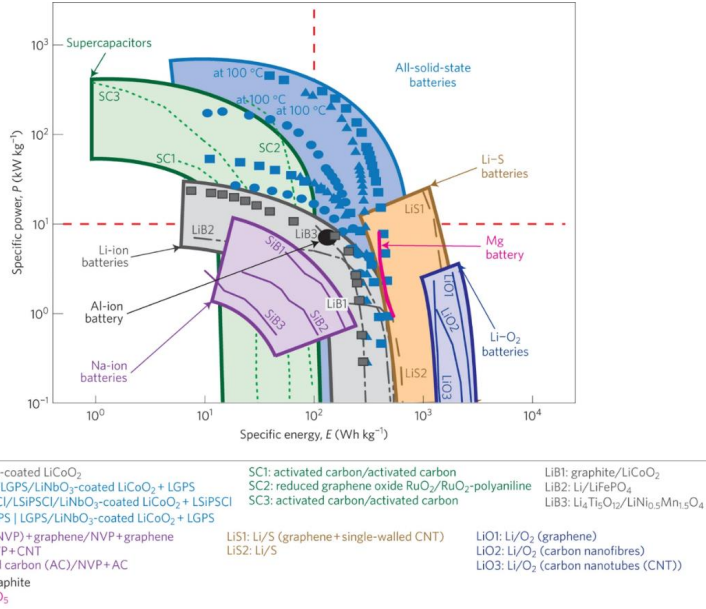


Figure 8 The Ragone plots of the reported batteries and capacitors.

(Reproduced with permission from ref.[95].)

2.1.4. Solid-state Na batteries

The development of low-cost and safer SSSBs to meet specific application scenarios (e.g., energy-storage plants) is an important target.[100] Despite some insight into SSBs over the past half-century, two key constraints limit the operation of the batteries – the inferior conductivity of the electrolyte and the poor interfacial contact between the electrodes/electrolyte.[90] Therefore, the development of new compositions with higher ionic conductivity and the construction of robust electrode/electrolyte interfaces are challenges for SSBs.[25]

Overall, SSBs are one of the ideal options for both high performance and high safety, as they can solve the current dilemma of energy density ceiling and safety concerns faced by LIBs.[87] From the reported laboratory data, SSBs (including solid-liquid hybrid batteries, semi-solid-state batteries, quasi-solid-state batteries, and all-solid-state batteries) are able to operate smoothly under some specific test conditions (e.g., higher than RT, applying external pressure, at very low charge/discharge current).[101, 102] Novel

electrolyte materials and electrode materials are the foundation of SSBs. It is also necessary to develop new SSB configurations and technologies for large-scale preparation.[96]

2.2. Solid-state Na⁺ ionic conductors

2.2.1. Development and classification of solid-state Na⁺ ionic conductors

There are three main categories of promising solid-state Na⁺ ionic conductors: oxides (e.g., Na-β/β''-Al₂O₃, NASICON, NYS)[103-105], sulfides (Na₃PS₄, Na₃SbS₄, Na₁₁Sn₂PS₁₂, Na₁₁Sn₂SbS₁₂)[106], and polymer-based electrolytes [e.g., polyethylene oxide (PEO), polyacrylonitrile (PAN)][107].

Sulfide electrolytes exhibit the highest conductivity but require protective synthesis and fabrication atmospheres due to their poor chemical stability (reacting with moisture to release toxic H₂S).[91] Polymer-based electrolytes enable good cathode/electrolyte interfaces, but the poor conductivity and the high operating temperature limit their scale-up applications.[108]

Na-β/β''-Al₂O₃ in oxide electrolytes was one of the first Na⁺ ionic conductors discovered and was commercially used in the 1980s for large-scale energy storage in Na/S battery systems,[109] but the synthesis process required sintering at temperatures up to 1600 °C.[110]

NASICON materials were reported by Hong et al. in 1976, and their structural modifications and electrochemical properties have been widely studied and reported.[111] However, the presence of phosphorus in conventional NASICON materials has limited the choice of matching cathode materials due to the easy oxidation of phosphorus.[4]

Rhombic NYS materials are another type of Na⁺ superionic conductor, which was discovered in the 1970s.[105, 112, 113] There is a lack of conductivity data at RT and very few reports on the structure and properties of such materials.[111] Considering the high Na⁺ ionic conductivity at elevated temperatures and the good stability of NYS, this is a promising class of Na⁺ ion conductors and is worthy of further study.[3]

The timeline of the development of Na⁺ ionic conductors is summarized in **Figure 9**.

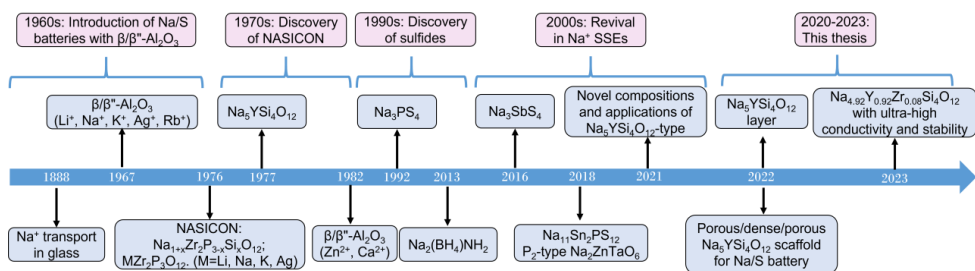


Figure 9 Timeline of the discovery and development of Na⁺ ionic conductors.

2.2.1.1. Na- $\beta/\beta''\text{-Al}_2\text{O}_3$

Na- $\beta/\beta''\text{-Al}_2\text{O}_3$ electrolytes are historically the first fast ionic conductors used in large-scale Na/S and Na/metal chloride (e.g., NiCl₂) batteries, especially at elevated temperatures (270 ~ 350 °C).[110] The cell configuration and operating principle of the Na/S battery are demonstrated in **Figure 10**. [114] The Na/S batteries operating at 300 °C capable of megawatt-level electric power storage have been commercialized by NGK Insulator Company.[115]

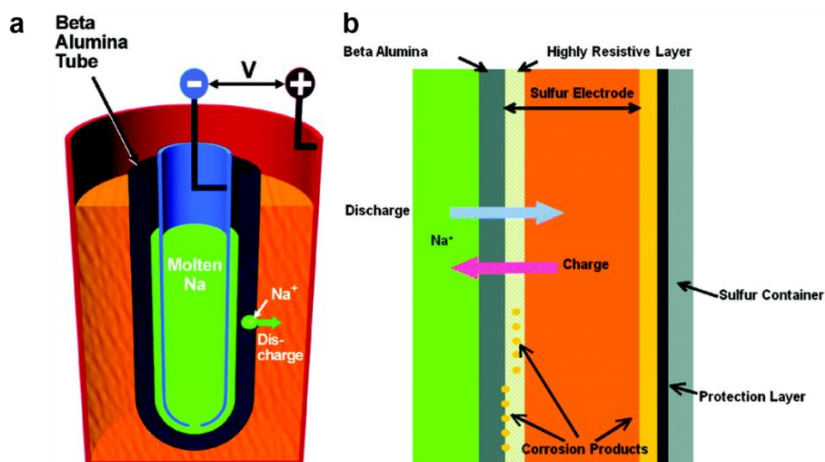


Figure 10 Schematic (a) cell configuration and (b) operating principle of the Na/S battery with Na- $\beta\text{-Al}_2\text{O}_3$.

(Reproduced with permission from ref.[116].)

The crystal structures of Na- β/β'' -Al₂O₃ are shown in **Figure 11**. [110] Na- β/β'' -Al₂O₃ (termed Na- β -Al₂O₃, Na- β' -Al₂O₃ and Na- β'' -Al₂O₃ with increasing Na₂O content, respectively) are composed of spinel layers between Na⁺ cations diffuse. [117] The Na⁺ ionic conduction exists only within its conduction planes, and the ionic conductivity is almost zero in the vertical direction of the structure. There are three distinct crystal structures, and the corresponding compositions and structure data are summarized in **Table 3**. Compared to Na- β -Al₂O₃ and Na- β' -Al₂O₃, the rhombohedral Na- β'' -Al₂O₃ phase exhibits a higher ionic conductivity due to its higher Na⁺ ions concentration in the conduction plane and the larger unit cell (1.5 times longer in *c* axis over the Na- β -Al₂O₃ phase). [118] It is reported that Na- β'' -Al₂O₃ single crystal possesses an extremely high ionic conductivity of 1 S cm⁻¹ at 300 °C, which is four times higher than that of its polycrystalline phase (0.22 ~ 0.35 S cm⁻¹ at 300 °C, but only 2.0 × 10⁻³ S cm⁻¹ at RT). [119]

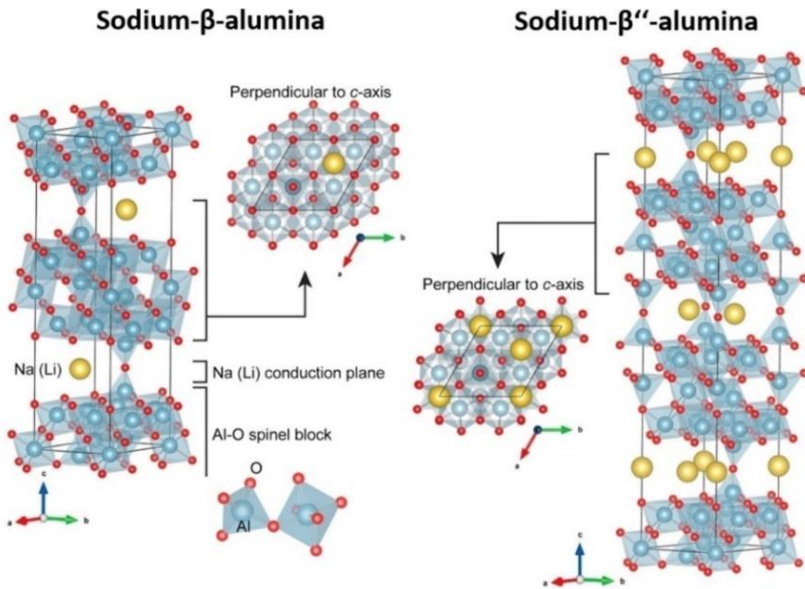


Figure 11 Crystal structures of Na- β/β'' -Al₂O₃.

(Reproduced with permission from ref. [110].)

Table 3 Composition, structure data and conductivity of Na- β / β' / β'' -Al₂O₃.

Abbreviation	Composition	Crystal system	Space group/ Å	σ / S cm ⁻¹	E _a /eV	Preparation temperature/°C	Ref.
Na- β -Al ₂ O ₃	Na ₂ O 11Al ₂ O ₃	hexagonal	P6 ₃ /mmc; a ₀ =5.59, c ₀ =22.61.	/	0.378	~ 1600	[117 , 120]
Na- β' -Al ₂ O ₃	Na ₂ O 7Al ₂ O ₃	rhombohedral	P6/mmc; a ₀ =5.59, c ₀ =22.56.	/		~ 1600	
Na- β'' -Al ₂ O ₃	Na ₂ O 5Al ₂ O ₃	rhombohedral	R3m; a ₀ =5.60, c ₀ =33.95.	$\sigma_{\text{poly,RT}}=10^{-3}$; $\sigma_{\text{poly,300 °C}}=4 \times 10^{-1}$.		~ 1600	

However, the highly conductive Na- β'' -Al₂O₃ single crystal fabrication is too expensive at the industrial scale.[110] On the other hand, polycrystalline Na- β'' -Al₂O₃ could be synthesized via high-temperature solid-state-reaction (~ 1600 °C), solution combustion and sol-gel methods. It is still challenging to achieve homogeneous and pure-phase products of Na- β'' -Al₂O₃ polycrystals since the synthesized β'' -Al₂O₃ is often mixed with the Na- β -Al₂O₃ phase.[121] Additionally, the remnant NaAlO₂ phase accumulated along the β'' -Al₂O₃ grain boundaries makes the polycrystalline product susceptible to the H₂O and CO₂ attack from the atmosphere, diminishing its chemical stability in air. The poor chemical stability of the β / β'' -Al₂O₃ mixture and the 2D ionic conduction hinder the application of β -Al₂O₃ in SSSBs.[122]

2.2.1.2. NASICON

NASICON is the abbreviation of NA Super Ionic CONductor.[123] The first NASICON with the composition of Na_{1+x}Zr₂Si_xP_{3-x}O₁₂ (0 ≤ x ≤ 3) was discovered in 1976 by Hong, Kafalas and Goodenough.[124, 125] Now the NASICON term is used to describe a special crystalline structure with a general composition formula of AMP₃O₁₂, where the A site can be occupied by monovalent cations (e.g., Li⁺, Na⁺, K⁺), divalent cations (e.g., Mg²⁺, Ca²⁺, Ba²⁺, Cu²⁺, Co²⁺), trivalent cations (e.g., Al³⁺, Y³⁺) and tetravalent cations (e.g., Ge⁴⁺, Zr⁴⁺, Hf⁴⁺); and the M sites can be occupied by divalent cations (e.g., Cd²⁺, Mn²⁺, Co²⁺, Ni²⁺, Zn²⁺), trivalent cations (e.g., Al³⁺, Ga³⁺, Y³⁺), tetravalent cations (e.g., Ti⁴⁺; Zr⁴⁺) and pentavalent cations (e.g., V⁵⁺; Nb⁵⁺; Sb⁵⁺).[126-128] NASICON features three-dimensional (3D) ionic diffusion channels within tetrahedra SiO₄, PO₄ and octahedra ZrO₆ for Na⁺ transport.[129] The 3D tunnels

for Na ion migration overcome the 2D restrictions of β - Al_2O_3 electrolyte. As shown in **Figure 12**, $\text{Na}_{1+x}\text{Zr}_2\text{Si}_x\text{P}_{3-x}\text{O}_{12}$ can form two polymorphs, which are rhombohedral ($R\bar{3}c$) and monoclinic ($C2/c$) ($1.8 \leq x \leq 2.2$) phases.[130] It is able to form a monoclinic phase at low temperatures, which can be considered as a rotational distortion of the rhombohedral phase. In the rhombohedral phase, two different Na^+ sites (Na1 and Na2) form the 3D diffusion network, but in the distorted monoclinic phase, the Na2 site splits into Na2 and Na3 to form both Na1-Na2 and Na1-Na3 diffusion channels. In this series of compounds, the framework includes the two interstitial sodium sites and the Na2 shows the highest mobility.

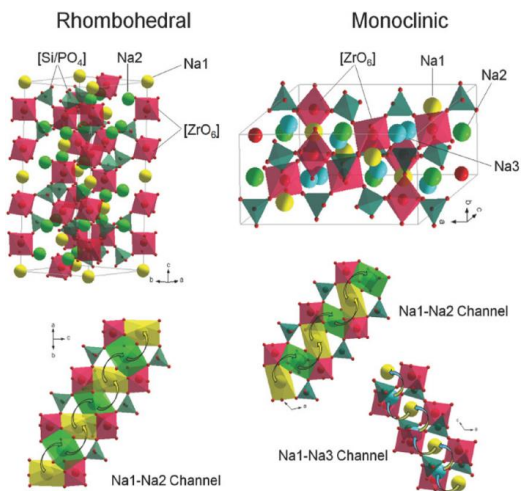


Figure 12 Crystal structures of rhombohedral and monoclinic NASICON compounds ($\text{Na}_3\text{Zr}_2\text{Si}_2\text{PO}_{12}$).

(Reproduced with permission from ref.[130].)

In NASICON-type compounds, the different compositions cause a huge ionic conductivity difference (up to several orders of magnitude).[131] The maximum ionic conductivity was observed when the effective ionic radius of the M-site was near 0.72 Å.[126] Since the ionic radii of Sc^{3+} (0.745 Å) and Zr^{4+} (0.720 Å) are the closest, Sc-substituted $\text{Na}_{3.4}\text{Sc}_{0.4}\text{Zr}_{1.6}\text{Si}_2\text{PO}_{12}$ prepared by solution-assisted solid-state reaction approach showed a high Na^+ ionic conductivity of 4.0 mS cm^{-1} at RT.[129] However, the expensive Sc is not suitable for scalable applications. Ma reported a bulk conductivity of $1.5 \times 10^{-2} \text{ S cm}^{-1}$ and a total conductivity of $5 \times 10^{-3} \text{ S cm}^{-1}$ for $\text{Na}_{3.4}\text{Zr}_2\text{Si}_{2.4}\text{P}_{0.6}\text{O}_{12}$ at RT, which is the highest Na^+ conductivity among NASICONs at RT.[132] NASICON materials generally show a huge grain boundary resistance (R_{gb}) at RT.

Attempts have been made to improve the total ionic conductivity (bulk and grain boundary conductivity) by applying different sintering techniques, such as rare earth oxide-assisted sintering[133] to densify the pellets with liquid-phase and ultrafast sintering[134] of $\text{Na}_3\text{Zr}_2\text{Si}_2\text{PO}_{12}$. Representative NASICONs are listed in **Table 4**.

Table 4 Conductivity and activation energy of NASICONs.

Composition	$\sigma_{25\text{ }^\circ\text{C}}/\text{mS cm}^{-1}$	E_a/eV	Ref.
$\text{Na}_{3.4}\text{Zr}_2\text{Si}_{2.4}\text{P}_{0.6}\text{O}_{12}$	5.0	0.32	[132]
$\text{Na}_{3.4}\text{Sc}_{0.4}\text{Zr}_{1.6}\text{Si}_2\text{PO}_{12}$	4.0	0.26	[129]
$\text{Na}_{2.96}\text{Nb}_{0.04}\text{Zr}_{1.96}\text{Si}_2\text{PO}_{12}$	4.95	0.21	[135]
$\text{Na}_{2.1}\text{Y}_{0.1}\text{Zr}_{1.9}\text{SiPO}_{12}$	1.98	0.25	[135]
$\text{Na}_{3.36}\text{Zn}_{0.08}\text{Zr}_{1.92}\text{Si}_{2.2}\text{P}_{0.8}\text{O}_{12}$	1.1	0.32	[136]
$\text{Na}_{3.2}\text{Hf}_2\text{Si}_{2.2}\text{P}_{0.8}\text{O}_{12}$	2.3	0.36	[137]
$\text{Na}_{3.4}\text{Hf}_2\text{Si}_{2.4}\text{P}_{0.6}\text{O}_{12}$	1.4	0.35	[137]
$\text{Na}_{3.6}\text{Hf}_2\text{Si}_{2.6}\text{P}_{0.4}\text{O}_{12}$	1.2	0.34	[137]

Unlike the sulfide-based electrolytes, where intimate electrode/electrolyte contact could be easily formed via the cold-pressing treatment, unstable electrode (especially the metallic Na)/electrolyte interface and high interfacial impedance have been found with NASICON-type electrolytes (without interface modification).[138, 139] A successful demonstration of Na/NASICON/ $\text{Na}_3\text{V}_2(\text{PO}_4)_3$ full cells has been reported by Tu et al. with a novel infiltration method of the cathode precursor solution, which realized good electrode/electrolyte interfacial compatibility.[140] The synthesis of NASICON materials is not as stringent as those of Na- β "- Al_2O_3 , but still, high-temperature sintering (> 1200 °C) is needed to prepare phase-pure highly ionic conductive NASICONs.[132]

2.2.1.3. $\text{Na}_5\text{YSi}_4\text{O}_{12}$ -type electrolyte

This class of electrolytes exhibits higher oxidation stability and improved chemical stability with oxide cathodes compared with solid sulfide electrolytes.[4, 6, 7] Currently, the RT bulk ionic conductivity of NYS, similar to other oxide solid electrolytes, is generally lower than that of sulfides, and their large grain-boundary resistance further restricts the total ionic conductivity. However, the development of NYS-type

electrolytes is still in the early stages. Further investigation is necessary to find out the intrinsic properties of the materials.[3]

The structure of NYS-type materials is shown in **Figure 13**. [141] The immobile Na atoms are situated within the rings. The high conductivity arises from the presence of mobile Na atoms between the columns. [142] This behavior is consistent with a structure consisting of $\text{Si}_{12}\text{O}_{36}$ rings stacked to form columns held apart by YO_6 octahedra. The size of the channels is dictated by the size of the YO_6 octahedra. The YO_6 octahedra, which links the columns, also holds them apart, leaving a large open channel near the twofold axes between the two columns. [143] Along these channels, Na ions can move quite freely. These compounds should have excellent conductivity parallel to the c -axis and, therefore, might be expected to be highly anisotropic conductors. [111] Because the $\text{Si}_{12}\text{O}_{36}$ rings are held apart by the LnO_6 octahedra, the amount of “open” space between rings is determined largely by the size of the Ln^{3+} ion. Assuming that the critical channel size has not been reached, this should result in a continuous increase in conductivity with the change of the Ln^{3+} radius. Shannon *et al.* reported that the highest conductivities and smallest activation energies were found for rare earth element ions having radii comparable to that of Na^+ ions. [105] Other NYS-type materials are listed in **Table 5**. The size of the channels containing the partly occupied Na^+ -sites was changed by the substitution of the Y site.

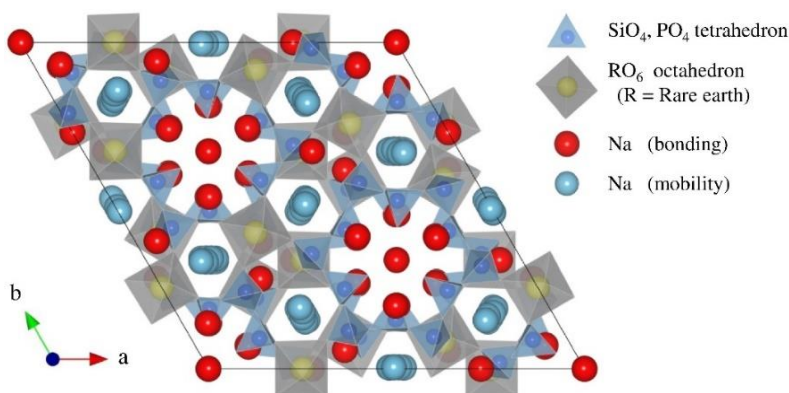


Figure 13 Crystal structure of $\text{Na}_5\text{YSi}_4\text{O}_{12}$ -type electrolyte.

(Reproduced with permission from ref.[141].)

Table 5 Conductivity and activation energy of reported Na₅YSi₄O₁₂ materials.

Composition	Structure	$\sigma_{300^\circ\text{C}}/\text{S cm}^{-1}$	Activation energy /eV (300 °C)	Year	Ref.
Na ₅ GdSi ₄ O ₁₂	rhombohedral	$\sigma_{300^\circ\text{C}} = 0.3$ $\sigma_{200^\circ\text{C}} = 0.06$	0.26	1977	[113, 144]
Na ₅ YSi ₄ O ₁₂	rhombohedral; R $\bar{3}c$; $a = 22.00 \text{ \AA}$, $c = 12.61 \text{ \AA}$.	$\sigma_{300^\circ\text{C}} = 0.15$; $\sigma_{300^\circ\text{C}} = 1.0$ (single crystal)	0.15	1978	[113]
Na ₅ LuSi ₄ O ₁₂	rhombohedral	0.06	0.33	1978	[111]
Na ₅ SmSi ₄ O ₁₂		0.3	0.32	1978	[111]
Na ₅ TbSi ₄ O ₁₂		0.2	0.34	1978	[111]
Na ₅ DySi ₄ O ₁₂		0.1	0.27	1978	[111]
Na ₅ ErSi ₄ O ₁₂		0.04	0.33	1978	[111]
Na ₅ TmSi ₄ O ₁₂		0.05	0.32	1978	[111]
Na ₅ YbSi ₄ O ₁₂		0.02	0.33	1978	[111]
Na ₅ ScSi ₄ O ₁₂		0.02	0.33	1978	[111]

NYS-type SSEs have some advantages over traditional liquid electrolytes, which make them attractive for use in advanced SSBs. (1) High ionic conductivity: NYS-type SSEs have ionic conductivities in the range of 10^{-3} to 10^{-2} S cm^{-1} (most of the reported conductivities are tested at elevated temperatures, like 300 °C).[143] This high ionic conductivity makes them suitable for use in full cells and other electrochemical devices. (2) Wide electrochemical window: they have a wide electrochemical window, which allows them to operate at higher voltages without decomposing or degrading. This makes them suitable for use in high-voltage applications.[142] (3) Good chemical stability: they are chemically stable in a wide range of environments, including aqueous and organic solvents, as well as at high temperatures. This makes them suitable for use in harsh operating conditions.[7] (4) Good mechanical stability makes them suitable for use in flexible and conformal batteries and other devices.[4] (5) Compatibility with a wide range of electrode materials: they are compatible with a wide range of electrode materials, including lithium, sodium, and other alkali metals, as well as various cathode and anode materials. (6) Acceptable cost: cost-efficient raw materials and facile preparation methods (such as solid-state reaction, melting-recrystallization, sol-gel method, solution-assisted solid-state reaction, etc., the especially solid-state

reaction was used in this thesis.) can guarantee a high phase purity, which makes the massive production possible.[4, 5]

2.2.1.4. Thiophosphate

Sulfide-based electrolytes are one of the attractive SSEs, as they possess a fast Na^+ ionic conduction at RT and require a relatively low temperature for synthesis.[145] Furthermore, only a cold-pressing treatment is enough to form good contact between the sulfide-based electrolyte and the electrode materials when assembling the full cells since it is mechanically ductile, further reducing the industrial production cost.[106] Na_3PS_4 is a typical sulfide-based ceramic electrolyte.[146] With a 3D pathway along the Na1 and Na2 sites in the open framework (**Figure 14**), cubic Na_3PS_4 ($I43m$: $a_0 = 6.9965 \text{ \AA}$) ceramic electrolyte owns a moderate conductivity at RT ($\sim 10^{-4} \text{ S cm}^{-1}$) and a relatively wide electrochemical window ($0 \sim 5 \text{ V}$).[130] The glass-ceramic phase of Na_3PS_4 exhibits an even higher total ionic conductivity of $(2.0 \sim 4.6) \times 10^{-4} \text{ S cm}^{-1}$ at RT and a lower activation energy for hopping ($0.197 \sim 0.280 \text{ eV}$).[147, 148] This is because intimate contacts among grains could be achieved in the Na_3PS_4 glass-ceramic phase, which effectively suppresses the grain boundary resistance. It is found that cation-substitution or anion-substitution in Na_3PS_4 -based compounds could further facilitate the Na ion conduction, as additional point defects are generated via the element doping or substitution.[92] Specifically, it should be mentioned that the $\text{Na}_{2.88}\text{Sb}_{0.88}\text{W}_{0.12}\text{S}_4$ composition at the Sb^{5+} and W^{6+} co-substituted P^{5+} sites achieved an unprecedented Na^+ ionic conductivity of up to 32 mS cm^{-1} at RT, which is the highest RT conductivity value reported so far for sulfide SIEs.[149] The conductivity and activation energy of typically reported Na_3PS_4 -type sulfides are summarized in **Table 6**.

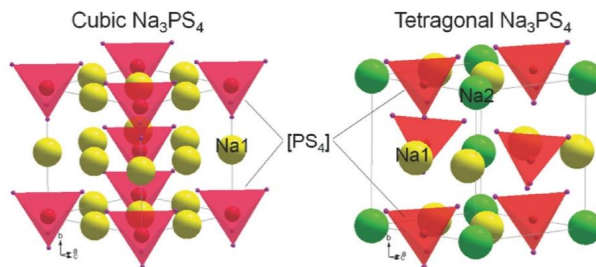


Figure 14 Crystal structures of Na_3PS_4 (cubic and tetragonal).

(Reproduced with permission from ref.[130].)

Table 6 Conductivity and activation energy of sulfides.

Composition	$\sigma_{25\text{ }^\circ\text{C}}/\text{mS cm}^{-1}$	E_a/eV	Ref.
Na ₃ PS ₄ (cubic)	0.46	0.200	[150]
Na ₇ P ₃ S ₁₁	1.097	0.220	[151]
Na ₃ SbS ₄	1.0	0.220	[152]
Na ₃ P _{0.62} As _{0.38} S ₄	1.46	0.256	[153]
Na _{2.9375} PS _{3.9375} C _{10.0625}	1.14	0.249	[154]
Na ₇ P ₃ Se	13.46	0.213	[151]
Na _{2.88} Sb _{0.88} W _{0.12} S ₄	32	0.218	[149]

However, the Na₃PS₄-type thiophosphate SSEs are unstable against oxygen and moisture in air and tend to decompose to the toxic H₂S.[155] Although the electrochemical stability window of Na₃PS₄ measured by cyclic voltammetry is in the range of 0.5 ~ 5 V vs. Na⁺/Na₊[146] experimental evidence suggests that it reacts with the Na metal anode. Interfacial layers such as Na₂S and Na₃P were detected on Na metal deposited on the surface of Na₃PS₄ using X-ray photoelectron spectroscopy (XPS).[156] The Na₂S in the interfacial layer is electronically insulating, which is detrimental to the cycling performance of the full cell. Theoretical calculations show that the electrochemical stability window of Na₃PS₄ is only in the 1.55 ~ 2.25 V region.[157] The narrow electrochemical stability window makes the sulfide susceptible to redox reactions after matching with the cathode and anode materials, leading to the rapid decay of the battery performance. Therefore, a lot of studies on sulfide electrolytes have been devoted to enhancing the stability of electrolyte materials or improving the electrode/electrolyte interface.[158]

2.2.1.5. Other new types of inorganic Na⁺ ionic conductors

With the rapid development of SSSBs, some novel Na ion conductors have been reported, such as the antiperovskite type and hydrides.

(1) Antiperovskites

These electrolytes mainly include Na₃OX (X = Cl, Br) and Na₃OBH₄. Na₃OBH₄ has a high structural tolerance and rotatable properties of BH₄ and exhibits a high Na ion conductivity of 4.4 mS cm⁻¹ at RT.[159] Similar to the oxide SIEs, the internal grain boundary impedance of the antiperovskite-based electrolytes is high. Unlike conventional oxide electrolytes, antiperovskite electrolytes are synthesized at lower temperatures (< 300 °C) and have higher ionic conductivity.[160] However, these materials are highly

hygroscopic in air, resulting in rare applications in full cells.[161] If the electrode/electrolyte interface issue can be solved, these materials will have very good prospects for application in SSBs.[161]

(2) Boro-hydrides

Usually, hydride electrolytes exhibit high ionic conductivity only above the phase transition temperature ($> 300\text{ }^{\circ}\text{C}$). However, the phase transition temperature of these materials is relatively high, which is one of the obvious disadvantages of these materials. Utilizing ion doping or preparation of composite electrolytes, the phase transition temperature of the materials can be reduced to near RT, which offers the possibility of practical applications of the materials in SSBs. For example, by mixing $\text{Na}_2\text{B}_{10}\text{H}_{10}$ with $\text{Na}_2\text{B}_{12}\text{H}_{12}$ in a 1:3 molar ratio and mechanically ball-milling, the obtained composite electrolyte has no phase transition and has a moderate RT ionic conductivity (0.1 mS cm^{-1}) and an electrochemical stability window of up to 5 V vs. Na^+/Na .[162] However, the other composition, $\text{Na}_5(\text{B}_{11}\text{H}_{11})(\text{B}_{12}\text{H}_{12})_2$, has an electrochemical stability window of only 2.6 V vs. Na^+/Na . The complicated preparation process and narrow electrochemical window of hydride electrolytes may hinder their further application.[163, 164]

2.2.2. The ionic transport mechanisms in solids

As it is well known, the ionic conductivity of SSEs is closely related to various types of disorders. The intrinsic ionic conductivity in crystals depends on the lattice defects: either Frenkel or Schottky defects are observed, while more complex structure disorder exists in SSEs.[165] **Figure 15** is the schematic of ion transport in (a) SIEs and (b and c) SPEs.[166] Ion transport in SIEs is facilitated by Schottky and Frenkel defects, as well as vacancies at grain boundaries. An interfacial layer (space-charge layer) forms when two different materials are in contact because of different chemical potentials. This layer can retard or accelerate ion transport across the interface, depending on the operating conditions. Ion conduction in SPEs has been proposed to occur through the amorphous and crystalline phases. Within the amorphous phase, the segmental motion of the polymer chains assists in the migration and hopping of alkali-metal ions (M^+) from one coordination site to another (panel b). In contrast, in the crystalline phase, conduction occurs through ordered domains formed by folded polymer chains, while the anions (X^-) migrate outside these tunnels (panel c).[26]

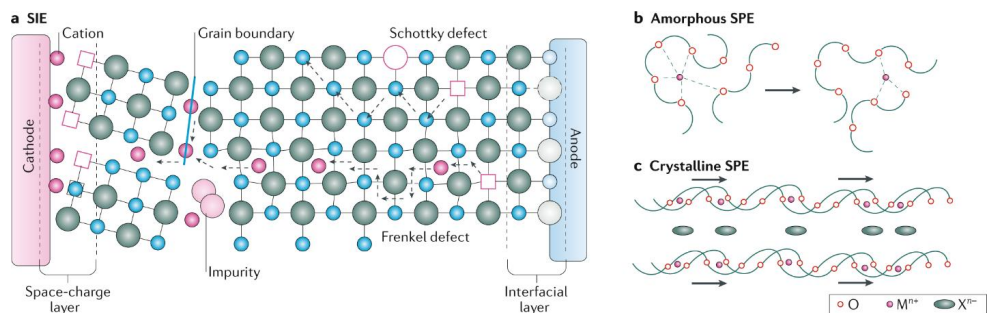


Figure 15 Ionic transport in solid inorganic electrolytes and solid polymer electrolytes.

(Reproduced with permission from ref.[26].)

2.3. Summary of research on solid-state Na batteries

SSSBs have attracted significant research attention as a promising alternative to conventional liquid electrolyte batteries due to their potential for higher energy density, improved safety, and environmental sustainability. The research on SSSBs involves several key areas, including the development of SSEs with high performance, optimization of the electrode materials, and design of the cell configuration.[90]

One of the critical challenges in developing SSSBs is to find suitable solid electrolytes with high ionic conductivity, chemical stability, and low interfacial resistance with the electrode materials. Several types of solid electrolytes have been investigated and reported, including oxide-based electrolytes ($\text{Na-}\beta/\beta''\text{-Al}_2\text{O}_3$, NASICON, NYS-type, etc.), sulfide-based electrolytes (Na_3PS_4 -type, $\text{Na}_{11}\text{Sn}_2\text{PS}_{12}$ -type, etc.), hydrides ($\text{Na}_5(\text{B}_{11}\text{H}_{11})(\text{B}_{12}\text{H}_{12})_2$, etc.), polymer-based electrolytes (PEO + NaClO_4 , etc.), and ceramic/polymer composite electrolytes (NASICON + NaClO_4 + PEO, etc.). Among these, oxide-type materials have shown great promise due to their high ionic conductivity and excellent stability,[87] while sulfide-based materials have shown higher RT ionic conductivities in $\text{Na}_{2.88}\text{Sb}_{0.88}\text{Mo}_{0.12}\text{S}_4$ (3.9 mS cm^{-1})[106] and $\text{Na}_3\text{SbS}_{3.75}\text{Se}_{0.25}$ (4.03 mS cm^{-1})[167].

Apart from the development of the SSEs, another critical area of research is the optimization of the electrode materials for SSSBs. The electrode materials need to be compatible with the solid electrolyte, have high capacity and have good cycling stability. Cathode materials in liquid electrolyte battery systems, such as NaMO_2 -type layered materials, polyanionic materials, and Prussian blue analogs, can typically be used directly in SSSBs.[168] However, the volume change of the AMs during the charging and discharging processes results in an interfacial degradation between the electrode and SSE. The development of all-solid-

state Na/S batteries or Na/gas (air, O₂, N₂, CO₂, etc.) batteries operating at RT will have more potential in terms of specific energy.[99] Although laboratory-scale Na/S and Na/CO₂ batteries with SSEs have been reported, both systems still face challenges. Na/S batteries are not only plagued by the proliferation of Na dendrites and poor electrode/electrolyte interfacial contact but also face very low S loading (~ 1 mg cm⁻²) and irreversible capacity losses due to the slow kinetics of the stepwise reaction and the electrically insulating properties of S.[6] Na/gas batteries suffer from ultra-high polarization voltages due to slow electronic transfer on the positive side of the gas and the capacity degradation due to the irreversibility of discharge products (e.g., superoxide, carbonate), in addition to the same problems of growth of Na dendrites and poor interfacial contact.[169]

Furthermore, the cell configuration plays a crucial role in the performance of SSSBs. Different cell designs, such as planar and cylindrical (only for flexible and soft polymer or composite electrolytes) cells, have been developed and optimized to improve the battery's performance, including capacity, energy density, and cycling stability.[96] The interfaces between the SSEs and both electrodes should also be addressed in the full cells. Co-sintering the SSE with cathode material, infiltrating active cathode materials in the porous electrolyte, and introducing the interface-compatible polymer in the composite cathode are several major solutions to optimize the cathode/SSE interface. Modifying the electrolyte surface, alloying the Na metal, and introducing liquid electrolytes are some strategies to address the interface of Na metal anode/SSE.[98]

In summary, the research on SSSBs has made significant progress in recent years, with the development of SSEs with high-performance, optimization of electrode materials, and cell configuration design. These advances provide a roadmap for the future development of efficient, safe, cost-efficient and environmentally friendly SSSBs for energy storage.

III. Synthesis and Characterization

3.1. Synthesis of $\text{Na}_5\text{YSi}_4\text{O}_{12}$ -type materials

3.1.1. Raw materials and synthesis method

The powder synthesis of NYS-type materials in this thesis typically adopts solid-state reaction methods, which consist of ball-milled mixing, drying, calcination and sintering steps with the nominal stoichiometric ratio of the starting materials. The ball-milled mixing step helps to ensure a homogeneous mixture of the starting materials. The calcination step eliminates gaseous substances at high temperatures. And the sintering step shall deliver dense pellets and tapes. Considering the structure of the thesis using three research topics in parallel, the chemicals used for the experiments and the preparation methods are described in **Chapter 4.2**, **Chapter 5.2** and **Chapter 6.2**, respectively.

3.1.2. Introduction of tape-casting method

Tape-casting is a widely used technique for the fabrication of ceramics.[79] The process consists of the spreading of a ceramic slurry onto a flexible substrate, followed by drying and sintering. This method is particularly well-suited for the production of thin, flat, and uniform SSEs with controlled thickness and microstructure. The tape-casting process typically begins with the preparation of a ceramic powder, which is mixed with a binder and a solvent to form a slurry. The slurry is then cast onto a flexible substrate using a doctor's blade, which controls the thickness of the resulting membrane. After drying, the tape is typically sintered at a proper temperature to densify the ceramic and remove the binder.[170, 171]

The preparation of the ceramic slurry is a critical step in the tape-casting process. The slurry consists of ceramic powder, a binder, a plasticizer, a solvent, and other additives as necessary. The ceramic powder is first mixed with the binder and plasticizer to form a homogenous mixture, which is then suspended in a solvent to create a slurry with the desired rheological properties.[172]

Once the slurry is prepared, it is cast onto a flexible substrate, such as a Mylar sheet, using a doctor's blade. The doctor blade controls the thickness of the resulting tape, which can range from tens of microns to several millimeters.[173] After casting, the tape is dried to remove the solvent and any excess plasticizer, leaving behind a green tape. The green tape is then sintered at high temperatures to densify the ceramic and remove any remaining binder. The sintering process can be optimized to achieve the desired microstructure, such as grain size and porosity. After sintering, the resulting ceramic tape is typically inspected for defects and measured for thickness and other physical properties.[174]

Tape casting is a widely used technique for the production of a range of ceramic materials, including electronic ceramics, structural ceramics, and advanced ceramics.[175] It offers several advantages over other ceramic processing methods, such as improved homogeneity, precise control over thickness and microstructure, and the ability to produce large quantities of material with high reproducibility. The tape casting method is a critical tool for the development of advanced ceramics and has been applied to a wide range of applications, from electronic devices to energy storage, such as SSBs.[176]

3.1.3. Sintering fundamentals

Sintering is a phenomenon or process that occurs when a molded body (green body) is heat-treated at the appropriate temperature and atmosphere. Its purpose is to transform the ceramic powder into a dense sintered body. After sintering, bonding occurs between the powder particles and the strength and density of the sintered body increase. This sintered dense body is a polycrystalline material whose microstructure is composed of crystals, glass, impurities and pores. The sintering process directly affects the grain size distribution, grain boundary volume fraction, pore size distribution, etc., in the microstructure. The properties of ceramic materials are not only related to the compositions but also closely related to the microstructure. For two sintered bodies with the same compositions but different grain sizes, differences in the amount of grain boundaries can lead to differences in the properties of the ceramics.[177]

The mechanical energy of the crushing and grinding process is converted into the form of surface energy in the powder. As the powder has a high surface energy and is in an unstable state, there is a tendency to spontaneously change to a low-energy state. The surface energy of the powder is higher than the grain boundary energy after sintering and the energy difference is the driving force of sintering. The grain boundary energy replaces the surface energy after the powder is sintered, which is the reason for the stable existence of polycrystalline materials.[178] The driving force of sintering is very low compared to the energy change of a phase transition or chemical reaction. Therefore, sintering requires the addition of high temperatures to the powder to transform it into a sintered body.

A model in **Figure 16** can be used to explain the sintering process. When the powder is tightly packed, there are still a large number of small pores between the particles. Due to the surface tension, pressure differences are produced on these curved surfaces:

$$\Delta P = \frac{2\gamma}{r} \quad (\text{Equation 16})$$

where γ is the surface tension of the powder and r is the spherical radius of the powder.

In the case of non-spherical surfaces, two principal curvatures r_1 and r_2 can be used the following:

$$\Delta P = \gamma \left(\frac{1}{r_1} + \frac{1}{r_2} \right) \quad (\text{Equation 17})$$

The above two equations (Equations 17 and 18) show that the additional pressure on the curved surface is inversely proportional to the radius of curvature of the spherical particle (or surface) and proportional to the surface tension of the powder.[178] It follows that the finer the powder, the greater the driving force of sintering due to curvature.

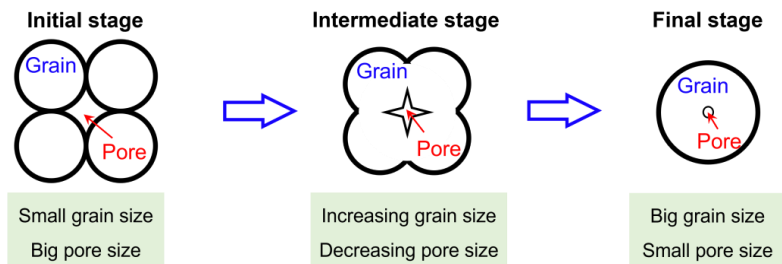


Figure 16 A model explaining the sintering process.

3.2. Characterization techniques

3.2.1. X-ray diffraction

X-ray diffraction (XRD) is a common technique used for the structural characterization of materials. XRD allows us to determine a material's crystal structure, crystallographic orientation, and lattice parameters. When an X-ray beam strikes a crystalline material, it interacts with the atoms in the crystal and is scattered in different directions. This scattering is known as X-ray diffraction. The scattered X-rays have a specific intensity and direction, which depend on the crystal structure and the wavelength of the X-rays.[179]

The intensity and direction of the diffracted X-rays can be used to determine the material's crystal structure. Bragg's law is the fundamental equation that describes the relationship between the angle of incidence, the lattice spacing, and the X-rays' wavelength (**Figure 17**). Bragg's law is expressed as:

$$n\lambda = 2d \sin \theta \quad (\text{Equation 18}),$$

where n is an integer, λ is the wavelength of the X-rays, d is the interatomic spacing in the crystal lattice, θ is the angle of incidence, and 2θ is the angle of diffraction.

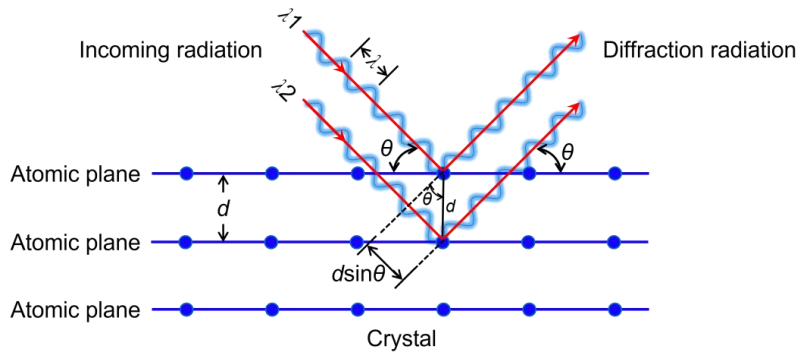


Figure 17 Schematic of Bragg plane diffraction.

An XRD instrument typically consists of an X-ray source, a sample holder, and a detector. The X-ray source produces a beam of X-rays, which is directed onto the sample.[180] The scattered X-rays are then collected by the detector, which measures the intensity and angle of the diffracted X-rays. XRD data are typically presented as a diffraction pattern, which is a plot of the intensity of the diffracted X-rays as a function of the diffraction angle 2θ . The diffraction pattern allows the determination of the crystal structure because the d spacing of the lattice planes is a characteristic fingerprint of the investigated material.

XRD is a powerful tool for structural characterization, but it has some limitations. XRD is not sensitive to the local structure of the material. Additionally, XRD requires a high-quality sample, and the sample must be crystalline and have a well-defined crystal structure.

3.2.2. Scanning electron microscopy

Scanning electron microscopy (SEM) and energy-dispersive X-ray spectroscopy (EDX) are two powerful tools for analyzing the structure and composition of materials at the microscale. When an incident electron beam with a certain energy impacts the surface of the sample, single or multiple elastic and inelastic collisions occur between the electrons and the nucleus and electrons of the element, and some electrons are

reflected by the surface of the sample while the rest are absorbed by the sample. In this process, more than 99% of the incident electron energy is converted to thermal energy, heating the sample, while the remaining about 1% of the incident electrons excite various signals from the sample. These signals mainly include secondary electrons, backscattered electrons, absorbed electrons, transmitted electrons, oscillating electrons, electron electric potential, cathodoluminescence and X-rays.

Secondary electrons are those electrons in the sample that are stimulated by the incident electrons. Due to the low binding energy between the nucleus and the valence electrons, the valence electrons can leave the atom and become free electrons when they have gained energy from the incident electrons that is greater than the binding energy of the sample. If the scattering process occurs at the surface of the sample, those free electrons with energy greater than the escape energy of the sample can be released from the sample surface and become free electrons in a vacuum, i.e., secondary electrons. The secondary electron comes from the region of 5 ~ 10 nm on the sample surface with an energy of 0 ~ 50 eV. It is very sensitive to the sample surface and can effectively indicate the microscopic morphology of the sample surface. Since it comes from the sample surface and the incident electrons are not reflected, the area of the secondary electrons produced is the same as the area of the incident electrons, so the resolution of the secondary electrons is high to the nanoscale.

Backscattered electrons are a fraction of the incident electrons that are reflected by the atoms of the sample, which includes both elastic and inelastic backscattered electrons. Elastically backscattered electrons are the incident electrons that are reflected by the nucleus in the sample at an angle of scattering greater than 90° , with essentially no change in energy (thousands to tens of thousands of eV). Inelastic backscattered electrons are electrons that are inelastically scattered upon impact between the incident electron and the electron outside the nucleus. Inelastically scattered electrons change not only in energy but also in direction. The energy range of inelastic backscattered electrons is wide, from tens of electron volts to thousands of eV.

SEM equipment gives a variety of information about the sample. In the case of EDX, the emitted X-rays of the sample are when it is excited by a beam of electrons.[181] This data is used to determine the elemental composition of the sample.

3.2.3. X-ray photoelectron spectroscopy

XPS is a technique for analyzing the surface chemistry of a material. XPS can measure the elemental composition, empirical formula, chemical state and electronic state of the elements within a material. XPS spectra are obtained by irradiating a solid surface with a beam of X-rays while simultaneously measuring

the kinetic energy and electrons that are emitted from the top 1 ~ 10 nm of the material.[182] A photoelectron spectrum is recorded by counting ejected electrons over a range of electron kinetic energies. Peaks appear in the spectrum from atoms emitting electrons of a particular characteristic energy. The energies and intensities of the photoelectron peaks enable the identification and quantification of all surface elements (except hydrogen).

When a beam of X-rays (photons) irradiates the surface of a sample, the photons can be absorbed by an electron in an atomic orbital of an element, causing the electron to be released from the nucleus and emitted from inside the atom with a certain kinetic energy (E_k) into a free photoelectron (shown in **Figure 18**), while the atom itself becomes an excited state ion. According to Einstein's law of photoelectron emission:

$$E_k = h\nu - E_b \quad (\text{Equation 19})$$

where E_k is the kinetic energy of the emitted photoelectron; $h\nu$ is the energy of the photonic X-ray source; E_b is the binding energy of a specific atomic orbital (different atomic orbitals have different binding energies).[182]

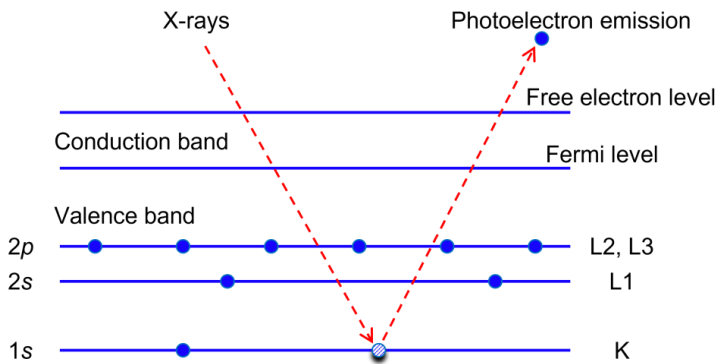


Figure 18 Schematic of X-ray photoelectric effect.

3.2.4. Transmission electron microscopy

Transmission electron microscopy (TEM) is an imaging technique used to observe the microscopic structure of a sample. The electron beam from the electron gun travels along the optical axis in the vacuum chamber through the focusing mirror and then converges into a thin, bright and uniform spot and irradiates

the sample. The electron beam that passes through the sample carries information about the structure inside the sample. The number of electrons transmitted through the dense part of the sample is small and the number of electrons transmitted through the sparse part is large.[183] After convergence focalization of the objective lens and primary magnification, the electron beam enters the following intermediate lens and projection mirror for integrated magnification. The magnified electron image is projected on a fluorescent screen in the observation room. Finally, the fluorescent screen converts the electron image into a visible image. The interaction of the electrons with the atoms in the material allows the imaging of the microstructure of the material, as well as the determination of its crystal structure through electron diffraction.[184]

3.2.5. Solid-state nuclear magnetic resonance

Solid-state nuclear magnetic resonance (SS-NMR) is an analytical technique that uses solid-state samples as the object of study.[185] The NMR phenomenon is the result of the interaction of radiofrequency with atomic nuclei of non-zero spin quantum number I in a static magnetic field. When I is not zero, the nuclear spins produce a magnetic moment μ . When a nucleus with a magnetic moment is placed in an external magnetic field B_0 , the magnetic field interacts with the nuclear magnetic moment, resulting in a different orientation of the nuclear magnetic moment and an energy level splitting, also known as Zeeman splitting. When the radiofrequency is applied to the nuclear spin system along the direction perpendicular to the static magnetic field B_0 , the nucleus undergoes a resonant jump between Zeeman energy levels.[186]

The sample for solid-state NMR is typically a polycrystalline or single-crystalline material. The material is packed into a rotor, which is spun rapidly around the axis of the magnetic field. This helps to average out any orientation effects and produces a more representative signal.[187] SS-NMR can provide information about the local environments of ions in the SSEs, such as their coordination number, bond distances, and angles. By comparing the NMR spectra of the SSE before and after an ionic migration event, it is possible to determine the pathways that the ions have followed.[188] For example, if an ion migrates through an interstitial site, it will change its local environment, leading to a change in the NMR spectrum. Additionally, it can be used to study the mobility of ions in SSEs. By measuring the rate of ion diffusion, it is possible to determine the activation energy for ionic migration and gain insight into the mechanisms that govern the process.[185]

3.2.6. Nano-indentation

Nano-indentation is one of the commonly used methods to test the mechanical properties of materials that can be measured at the nanoscale, such as load-displacement curves, modulus of elasticity, hardness, fracture toughness, strain-hardening effects, viscoelastic or creep behavior, etc.[189, 190] The schematic of the deformation pattern of an elastic-plastic sample before, during, and after indentation is shown in **Figure 19a**. The depth of the indenter in contact with the sample under applied load is defined as the contact depth (h_c). The depth measured during indentation (h) consists of the depression of the sample around the indenter (h_s) and h_c . The depression of the sample ($h_s = h - h_c$) is caused by elastic displacements and should be subtracted from the obtained values to get the real depth of indentation and the real hardness. The radius of the depression circle is a . The final depth of the residual hardness impression is h_f when the indenter is completely withdrawn after unloading.[189]

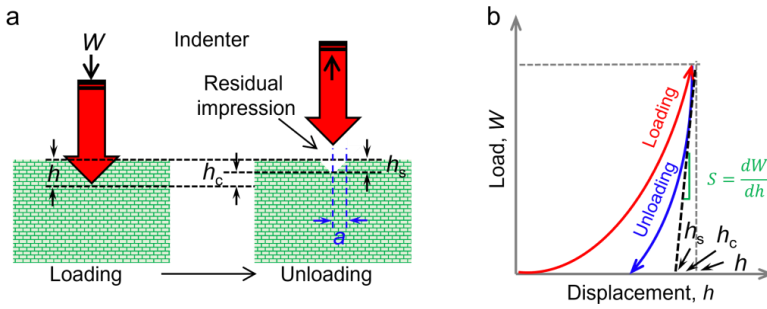


Figure 19 (a) Schematic of the indenting process and (b) schematic of the load-displacement curve.

A typical load-displacement curve is shown in **Figure 19b**. The load and displacement at peak load are W_{max} and h_{max} , respectively. The depth of contact h_c at the maximum load from h_{max} can be expressed as:

$$h_c = h_{max} - \frac{\epsilon W_{max}}{S_{max}} \quad (\text{Equation 20})$$

where $\epsilon = 0.72$ for the conical indenter, $\epsilon = 0.75$ for the paraboloid of revolution, and $\epsilon = 1$ for the flat punch; and S_{max} is the stiffness (the inverse of the yield stress) equal to the slope of the unloading curve ($\frac{dW}{dh}$) at W_{max} . [189]

3.3. Electrochemical testing and analysis

3.3.1. Ionic conductivity

The transport of ions in crystals takes place mainly as point defects. There are Schottky and Frenkel defect types for point defects (**Figure 20**).[191]

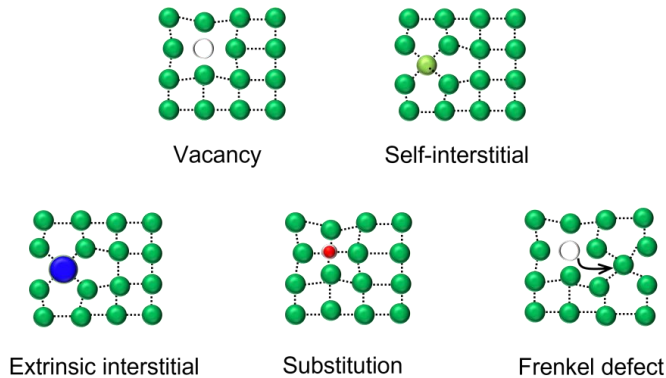


Figure 20 Schematic of point defects in a crystal.

The thermal vibration of ions allows some ions to leap to the adjacent interstitial sites or vacancies, thus enabling the migration of ions. Some common mechanisms for ion transport in SSEs are vacancy-mediated diffusion, interstitial diffusion, grain boundary diffusion, and surface diffusion.[192, 193]

Vacancy-mediated diffusion: ions move through the SSE by hopping between vacant sites in the crystal lattice. The vacancies can be created by crystal structure defects or thermal activation. The movement of ions in this mechanism is thermally activated, and the diffusion rate depends on factors such as temperature, vacancy concentration, and the size and charge of the ions. The strategy of different site substitutions to optimize the concentration of mobile species and vacancies is also used in this thesis to explore compositions with high conductivity.[194]

Interstitial diffusion: ions move through the SSE by occupying interstitial sites between the atoms or ions in the lattice. This mechanism is typically observed for small ions such as Li and H, which can occupy interstitial sites in a crystal lattice. The diffusion rate is determined by the concentration of interstitial sites and the activation energy required for the ions to move between them.[195]

Grain boundary diffusion: in polycrystalline SSEs, ions can also move along the grain boundaries between individual crystals.[196] This mechanism is often observed in materials such as ceramic electrolytes, where the grain boundaries provide a network of pathways for ion transport. The diffusion rate in this mechanism is determined by the concentration of grain boundaries and the material's grain size. In general, the energy barrier for ion diffusion in grain boundaries is much higher than that for diffusion within grains.

Surface diffusion: In some SSEs, ions can also move along the surface of the grain, particularly in nanostructured materials. The diffusion rate in this mechanism is determined by the surface area of the material and the surface energy.

One of the most common methods of testing the ionic conductivity of SSEs is using electrochemical impedance spectroscopy (EIS).[197] EIS is a non-destructive technique that is widely used to measure the ionic conductivity of SSEs. An alternating current (AC) is applied to the electrolyte and the resulting sinoidal phase shift of the current is measured. By analyzing the impedance of the system at different frequencies, one can determine ionic conductivity. With the EIS method, the electrodes on both sides of the electrolyte can be either ionically reversible electrodes (e.g., Na metal) or ionically blocking electrodes (e.g., Ag and Au coatings).

With the direct current (DC) polarization method, DC voltage is applied to the SSE to measure the resulting current flow. By analyzing the current-voltage curve, the ionic conductivity of the electrolyte can be determined. In this case, the electrodes on both sides of the electrolyte should be electronic-blocking electrodes.[25]

3.3.2. Electronic conductivity

There are two primary mechanisms for electron transport: band transport and hopping transport.

Band transport: electrons move through the material by jumping between energy bands. In metals and semiconductors, there are multiple energy bands that the electrons can occupy, with gaps between the bands known as band gaps. Electrons in the lower energy bands are able to move freely throughout the material, while electrons in the higher energy bands are restricted to a smaller region. When an electric field is applied to the material, the electrons in the lower energy bands can accelerate and move through the material, creating a current.[25]

Hopping transport: electrons move through the material by hopping from one atom or molecule to another. This mechanism is common in insulators and some semiconductors, where the band structure does not allow the free movement of electrons. In hopping transport, electrons move by jumping from one site to

another, with the probability of hopping determined by the energy levels of the sites and the distance between them. Hopping transport is typically slower than band transport but can still result in a measurable current.[197]

In general, the electronic conductivity of a semiconductor follows the Arrhenius relationship with temperature over a wide range of temperatures:

$$\sigma_e = \sigma_{0,e} e^{-\frac{E_{a,e}}{kT}} \quad (\text{Equation 21})$$

where σ_e is the electronic conductivity; $\sigma_{0,e}$ is a prefactor.

To test the electronic conductivity of SSEs, the DC polarization method and four-point probe method can be used, depending on the state of the materials.[198]

DC polarization method is the facile and most commonly used way for testing the electronic conductivity of SSEs. A constant DC voltage (U) can be applied on both sides of the electrolyte pellet, and after the current (I) is stabilized (usually 2 ~ 5 h), the resistance (R) of electron transport can be calculated using Ohm's law, and thus the electron conductivity can be obtained.

$$R = \frac{U}{I} \quad (\text{Equation 22})$$

The four-point probe method is a technique placing four electrodes on the surface of the SSE and measuring the voltage drop across the two inner electrodes when a current is passed through the two outer electrodes. This technique is particularly useful for measuring the electronic conductivity of thin films and coatings.

3.3.3. Activation energy

The activation energy of ionic migration in SSEs can be measured using a variety of techniques.

The Arrhenius plot is the most commonly used method to determine the activation energy of ionic migration in SSE.[199] The ionic conductivity at different temperatures can be measured and plotting the natural logarithm of the conductivity can be done against the reciprocal of temperature. The slope of the resulting line is equal to the activation energy of ionic migration.[199]

Isothermal ionic conductivity measurements are carried out at a fixed temperature and varying frequencies of the applied AC. The resulting frequency-dependent conductivity data can be analyzed using different models to determine the activation energy.[200]

3.3.4. Electrochemical stability window

The electrochemical stability window of SSEs can be tested using a variety of techniques, including:

Cyclic voltammetry (CV) is a commonly used technique for measuring the electrochemical stability window of SSEs.[201] This technique involves applying a cyclic voltage waveform to the electrolyte and measuring the resulting current response. By gradually increasing the voltage amplitude, one can determine the onset of oxidation or reduction reactions, which indicate the upper and lower limits of the electrochemical stability window.

Linear sweep voltammetry (LSV) is another technique that can be used to measure the electrochemical window of SSEs, which applies a linearly increasing voltage to the electrolyte and measures the resulting current response. By analyzing the current-voltage curve, one can determine the upper and lower limits of the stability.

The potentiostatic intermittent titration technique (PITT) applies a series of constant potential steps to the electrolyte and measures the resulting current response. One can determine the stability window by analyzing the current response at different potentials.[202]

3.3.5. Areal-specific resistance*

In SSBs, the solid-solid interface between Na metal and SSE remains a considerable challenge for development. The high reactivity of metallic Na can also result in a reduction of the SSEs, thus destabilizing the Na/SSE interface and deteriorating the electrochemical performance. For example, the Na₃PS₄ electrolyte decomposes into a poorly ionically conducting and electronically insulating interlayer composed of sodium sulfide and sodium phosphide when it contacts the Na metal.[156] In addition, volume changes upon the Na metal electrode's plating and stripping (i.e., charge and discharge) further result in a rather unstable interface between Na and SSE. The intimate contact between Na metal and SSE with high ionic conductivity and chemical/electrochemical stability can reduce the interfacial impedance, which can be evaluated in terms of areal-specific resistance (ASR_{inter}), and ensure a homogeneous stripping/plating of Na⁺ ions. The calculation of ASR_{inter} of the interface between Na metal and SSE can be written as:

$$ASR_{inter} = R_{inter}S \quad (\text{Equation 23})$$

* Content of this section has been published in *Energy Technology* (DOI: 10.1002/ente.202200149).

where R_{inter} indicates the interfacial resistance derived from the internal resistance of the cell and S indicates the effective contact area between Na and SSE. In this case, the contact area of both sides is involved like in symmetric cells with Na metal as electrodes; then the measured R_{inter} has to be divided by 2.[25]

A high ASR_{inter} gives rise to a high overpotential, which can reduce the overall energy efficiency of the cell, and trigger an inhomogeneous nucleation in the Na^+ ion plating process, in turn increasing the local current density and inducing the formation of dendrites.[25]

3.3.6. Critical current density*

The critical current density (CCD) is an important parameter in SSEs to test the dendrite tolerance and to evaluate starting anomalies and final failure during stripping and plating with increasing current.[25]

Additional layers can artificially modify an interface to achieve good interfacial contact between Na and SSE while reducing the interfacial impedance and enhancing the CCD, which is a further common parameter to evaluate the performances of the SSE and the interfacial contact. The CCD is defined as the transport current at which the flow voltage (e.g., significant voltage drift) appears. The CCD is given by the critical current I_c divided by the cross-sectional area S of the contact region, as described in Equation (24).[203-205]

$$CCD = \frac{I_c}{S} \quad (\text{Equation 24})$$

In the CCD measurement, the polarization voltage is relatively smooth before reaching the CCD; when CCD is reached, there is a significant fluctuation in the polarization voltage, followed by short-circuiting. The CCD depends on the properties of the SSE material itself and the stability of the interface between the Na metal and the SSE.[25]

IV. Fabrication of Thin Sheets of the Sodium Superionic Conductor Na₅YSi₄O₁₂ with Tape Casting[†]

4.1. Chapter introduction

The conductivity at elevated temperatures (typically 200 ~ 300 °C) and crystal structure of NYS-type SSEs have been introduced in **Chapter 2.2.1**. However, NYS electrolytes were prepared by the melting-recrystallization method, which required high temperatures (≥ 1450 °C) and complex procedures.[5] By optimizing the components and ratios of the slurry, we successfully fabricated NYS thin sheets using the tape casting technique and investigated their RT conductivity and other properties as the SSEs.

Tape casting of ceramics, first patented by Howatt in 1952 for the preparation of thin capacitor sheets is suitable for both the thickness-adjustable (usually 10 ~ 1000 μm for the green tape) and the continuous fabrication of ceramic products. It is one of the primary techniques for large-scale ceramic manufacturing used in applications like porous membranes, electronic substrates, wear-resisting plates, capacitors, and SSE-supported batteries and fuel cells today.[171, 206] However, the tape casting method usually utilizes highly volatile non-aqueous solvents. Many efforts have been undertaken in recent decades towards improving the application of tape casting using aqueous solutions and natural products as alternatives for the frequently toxic solvents and binders, driven by environmental and health concerns.[207] Especially in the battery field, Ye *et al.* have successfully fabricated Li₇La₃Zr₂O₁₂ (LLZO) electrolytes by using an aqueous tape casting technique.[208, 209] Although the room-temperature ionic conductivity ($\sigma_{\text{RT}} = 0.15$ mS cm⁻¹) has potential for improvement, this work integrated water-soluble, eco-friendly polymers as binders and plasticizers to achieve successful preparation.[210]

Compared to the studies on the production of Li⁺ ion-conducting SSEs at scale, there are scarce studies on the scaling-up of Na⁺ ion SSEs except for the commercialized Na- β / β' -Al₂O₃ dedicated to high-temperature Na/S batteries. Among the Na⁺ ion-conducting SSEs that can be found as sulfides,[211] polymers or oxides,[212] the latter benefit from favorable stability in air, established synthesis processing as well as desirable σ_{RT} . Therefore oxide-based ceramic electrolytes are regarded as a superior choice for mass preparation. Li and Ligon *et al.* reported the fabrication of Na- β' -Al₂O₃ solid electrolyte employing tape casting with a mixture of ethanol and methylethylketone (MEK) as solvents and achieved $\sigma_{200\text{ }^\circ\text{C}}$ of 12 mS cm⁻¹ and $\sigma_{300\text{ }^\circ\text{C}}$ of 180 mS cm⁻¹, respectively,[213, 214] while the synthesis of Na- β' -Al₂O₃ requires sintering temperature over 1600 °C for densification. Okubo *et al.* have prepared Na₃Zr₂Si₂PO₁₂ (NaSICON) with the addition of 60Na₂O-10Nb₂O₅-30P₂O₅ glass (5 ~ 10 wt%) as a sintering aid and used the tape casting technique to obtain a σ_{RT} of 0.44 mS cm⁻¹. [215] The tedious procedure for the preparation of NASICON

[†] Content of this section has been published in *Chemical Engineering Journal* (DOI: 10.1016/j.cej.2022.134774).

raw powder and the adoption of toxic toluene as a solvent in tape casting restrict scale-up.[215] Another Na⁺ ion superionic conductor, silicate-based NYS offers a comparable σ_{RT} and high stability with humidity, which makes it a good choice for aqueous tape casting fabrication. The facile synthesis for obtaining pure phase powders makes this material attractive as cost-effective SSEs and for up-scaling.

Herein, NYS was used for the manufacturing of ceramic sheets using the aqueous tape casting technique. An innovative sandwiched structure design used for the sintering process enabled the preparation of dense, crack-free, flat and robust tapes with different sizes and thicknesses. The sintered tapes of NYS showed decent σ_{RT} (1.0 mS cm⁻¹) and favorable mechanical properties (hardness H of 2 GPa and elastic modulus E of 45 GPa). XRD refinement and SEM revealed a highly pure rhombohedral phase and a dense microstructure, respectively, which explained the high conductivity of the sintered NYS sheets at RT. The activation energy for ionic conduction, the electrochemical stability window, CCD and galvanostatic cycling stability were also investigated.

4.2. Experimental

4.2.1. Preparation

The calcined NYS precursor powder was synthesized with a solid-state reaction by stoichiometrically mixing Na₂CO₃·H₂O (Aldrich, 98%), Y₂O₃ (VWR, 99.0%), and SiO₂ (Aldrich, 99%, 1 ~ 5 μm) and appropriate ball-milling of 24 h. The calcination was carried out at 950 °C in air for 5 h. An aqueous solution was prepared by mixing and dissolving methylcellulose (MC, Alfa Aesar), polyethylene glycol (PEG, Merck) and glycerol (Merck, 99%) in the deionized water with the assistance of a stirrer (IKA, RET Basic). Then the NYS precursor powder was added to the aqueous solution. The suspension was homogenized in a vacuum (ca. 10⁴ Pa) with zirconia balls (5 mm in diameter) in a planetary mixer (Thinky, ARE-500) at 1000 rpm for 10 minutes to form a uniform slurry for tape casting. Details of the recipe are listed in **Table 7**. The selection and optimization of the percentage content of dispersant, binder and plasticizer in the aqueous slurry in terms of the rheological behavior and the characteristics of the green tape have been reported for LLZO tapes.[208] The mixed slurry was transferred into the slurry reservoir of the tape-casting machine and then cast onto a Mylar substrate foil using a height-adjustable doctor blade. Here a slit width of 0.4 mm at a blade speed of 10 mm s⁻¹ was used. After drying overnight in an ambient atmosphere, the tapes were warm-pressed at 80 °C and 120 MPa for 2 minutes to enhance the green density before punching, laminating and sintering steps. As the green tapes are thin and flexible, they can be punched into different diameters and laminated into multi-layers as required (**Figure 21**). The sintering at 1100 °C for 6 h resulted in densities of 2.57 ~ 2.72 g cm⁻³, corresponding to 90 ~ 95 % of the theoretical density (2.86 g cm⁻³).[111]

It should be noted that in order to obtain a flat and dense tape, the green tape was placed between two NYS pellets prepared by uniaxial pressing and sintering. This sandwiched structure (**Figure 22**), prepared with the same raw powder, effectively prevents the tape from bending and sticking to the substrate during the high-temperature sintering process. Since tapes are typically thin, the sintering process requires only the gravity of the top NYS pellet (produced the pressure of ~ 77 Pa, see **Figure 22** and Equation 25) to ensure a flat tape without pressure sintering.

Table 7 Slurry recipe for the NYS tape.

Material	Function	Mass percentage (%)
NYS precursor	Ceramic precursor	32.64
Deionized water	Solvent	59.35
Methylcellulose	Binder	0.89
Glycerol	Plasticizer	3.56
Polyethylene glycol	Plasticizer	3.56

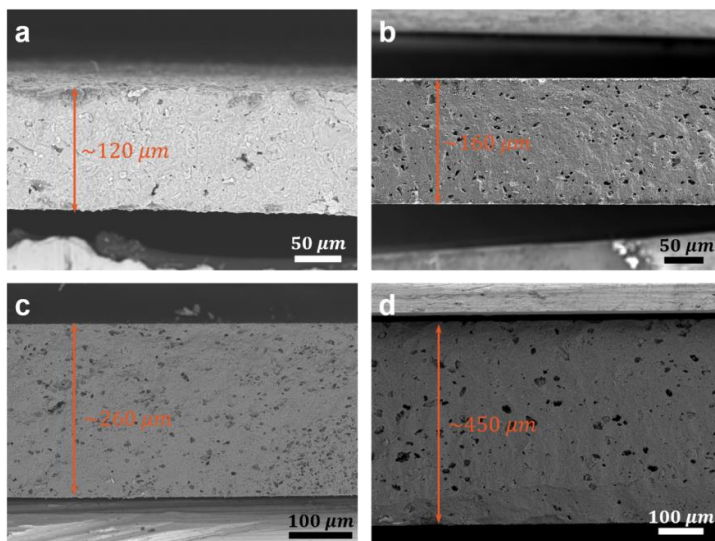


Figure 21 Cross-sectional SEM images of NYS tape with different thicknesses (120, 160, 260 and 450 μm).

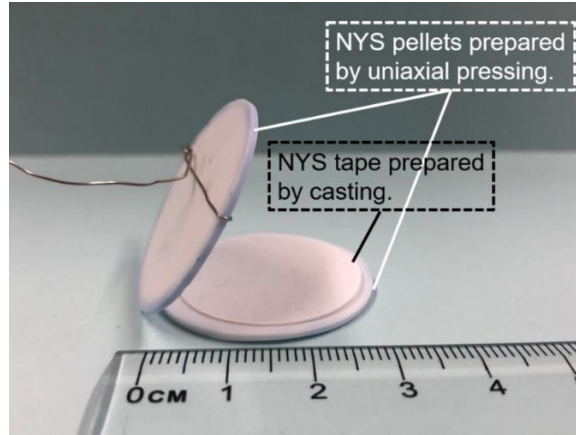


Figure 22 Photograph of the sandwiched structure used for the tape sintering.

The calculation for the load (NYS pellet) applied during sintering (**Figure 22**, for example):

The mass of each NYS pellet is about $m = 3$ g. The diameter of NYS green tape is $d = 22$ mm. Gravitational acceleration: $g = 9.8$ N kg⁻¹.

$$P = \frac{F}{S} = \frac{mg}{\pi\left(\frac{d}{2}\right)^2} = \frac{3 \times 10^{-3} \times 9.8}{\pi\left(\frac{22 \times 10^{-3}}{2}\right)^2} = 77.4 \text{ Pa.} \quad (\text{Equation 25})$$

4.2.2. Characterization

The crystal structure of NYS was characterized by XRD using a Bruker D4 ENDEAVOR diffractometer with Cu K_{α} radiation. The crystal lattice parameters of the sample were determined by the software Jana2006 program for the Rietveld refinement.[216] The microstructure of the sintered tape was analyzed using the scanning electron microscope HITACHI TM3000 and Zeiss Merlin field-emission SEM equipped with an energy dispersive spectroscopy (EDX) detector to analyze the elemental composition of samples.

The electrical conductivities were measured with two commercial electrochemical systems (Keysight E4991B and Novocontrol Technologies Alpha-A), with an AC frequency range from 3 GHz to 1 MHz and from 7 MHz to 1 Hz, respectively. In combination, the impedance spectrum of the samples from 3 GHz to 1 MHz can be observed. The fitting of the impedance data was conducted by the Zview software (Scribner Associates Inc.). The as-sintered tapes were sputtered with Au on both sides for the AC impedance

measurements in the frequency range from 3 GHz to 1 Hz with an alternating voltage amplitude of 5 mV. The temperature-dependent impedance was recorded between -100 and 100 °C to determine the activation energy (E_a).

The electrochemical window, CCD and galvanostatic cycling stability were measured with an electrochemical workstation (BioLogic VMP300) equipped with climate chambers (Vötsch, VT4002) for controlling the temperature. The LSV measurement was performed in an asymmetric cell with Na as the reversible electrode and Au as the blocking electrode, which was assembled in a glovebox (Glovebox System, Germany) filled with Ar gas. The voltammetry range for the LSV measurement was between open-circuit voltage (2.2 V) and 8 V (vs. Na⁺/Na) and the scanning rate was 0.1 mV s⁻¹. The CCD and galvanostatic cycling stability measurements were performed in a Na||NYS tape||Na symmetric cell with Na metal as reversible electrodes in a Swagelok cell. The galvanostatic cycling for testing the Na⁺ plating/stripping stability was performed under the constant current density of 0.8 mA cm⁻².

The indentation tests were conducted at RT using a NanoTest Xtreme test setup from Micro Materials® (Wrexham, UK) equipped with a diamond Berkovich tip. The samples were indented at a constant loading time of 10 s to maximum load. When the maximum load was reached, the load was held constant for 5 s before unloading the sample. The analysis of the data was based on an automatic procedure of the instrument following the Oliver-Pharr methodology[217] and ASTM E2546-07.[218] Modulus and hardness were derived from the load-displacement data by determining contact stiffness from the unloading portion. Poisson's ratio and Young's modulus of diamond were assumed as $E_i = 1141$ GPa and $\nu_i = 0.07$, respectively.[219]

The sintering behavior of NYS tape was measured with a 402 C dilatometer (Netzsch-Gerätebau GmbH) between 30 and 1000 °C in air. The heating and cooling rates during the test were 10 K min⁻¹. The sample was prepared by isostatic pressing of an 8 mm diameter and 5 mm thickness pellet.

4.3. Results and discussion

4.3.1. Preparation, crystal structure and microstructure

The preparation process of NYS tapes consists of four steps: slurry preparation, tape casting, punching and sintering. The first step was the mixing of the slurry, comprising the NYS precursor powder, binder, plasticizer, and water as solvent. The second step was to inject the well-mixed slurry into the tape reservoir for casting and to evaporate the solvent, where the doctor blade gap and casting speed were two parameters that significantly influenced the quality of the green tape. Before sintering, the peeled tape was punched into different shapes.

The crystal structure of tape-cast NYS was characterized by XRD (**Figure 23a**) and the refinement demonstrated that NYS crystallized in the rhombohedral phase with space group $R\bar{3}c$ (**Figure 23b**). The refined lattice parameters are $a = 22.019 \text{ \AA}$, $c = 12.605 \text{ \AA}$, and $V = 5292.6 \text{ \AA}^3$, which is very close to the reported data ($a = 22.03164 \text{ \AA}$, $c = 12.60818 \text{ \AA}$)[142].

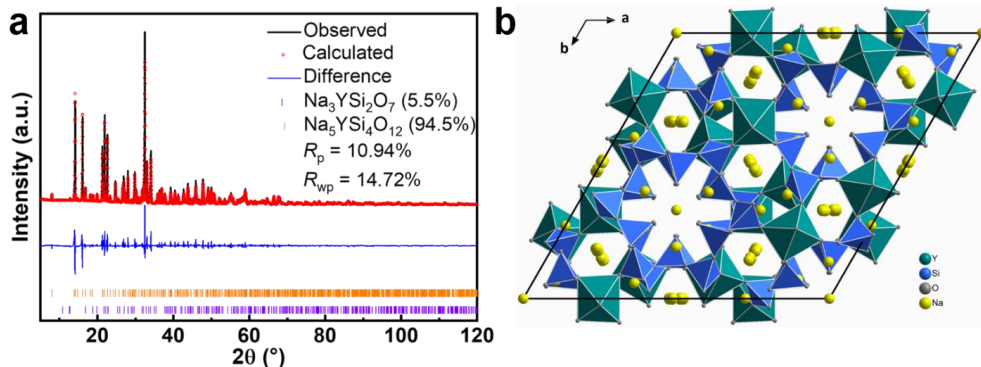


Figure 23 Crystal structure analysis of NYS tape.

(a) XRD pattern of sintered NYS tape (1100 °C for 6 h), which exhibits high crystal phase purity ($\text{Na}_5\text{YSi}_4\text{O}_{12}$: 94.5%; $\text{Na}_3\text{YSi}_2\text{O}_7$: 5.5%). (b) Projection of crystal structure of NYS from the refinement of XRD patterns along $[001]$ direction.

The microstructure of the NYS tape was shown in the cross-sectional and top-viewed SEM images (**Figure 24**), and the thickness of the tape was about 160 μm . The uniform elemental distribution in the NYS tape is shown in **Figure 25**. The analysis of crystal structure and microstructure showed that the sintered tape had good crystalline phase purity and high density.

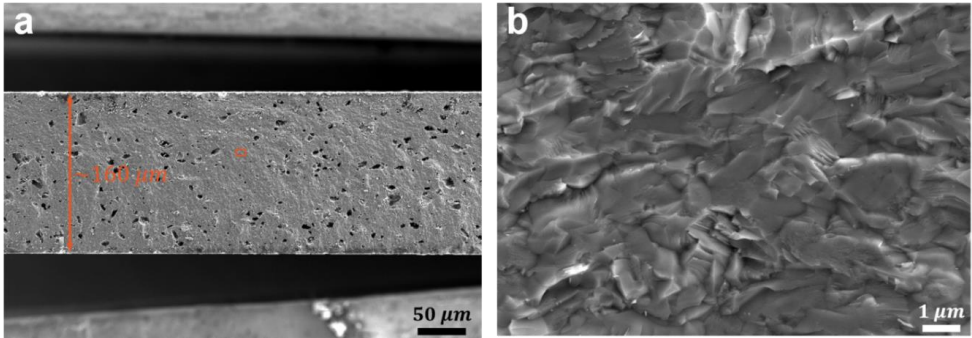


Figure 24 Morphology of the NYS tape microstructure.

SEM images of the cross-section (a) and the top surface (b) of NYS. The thickness of the tape is about 160 μm and the microstructure is very dense.

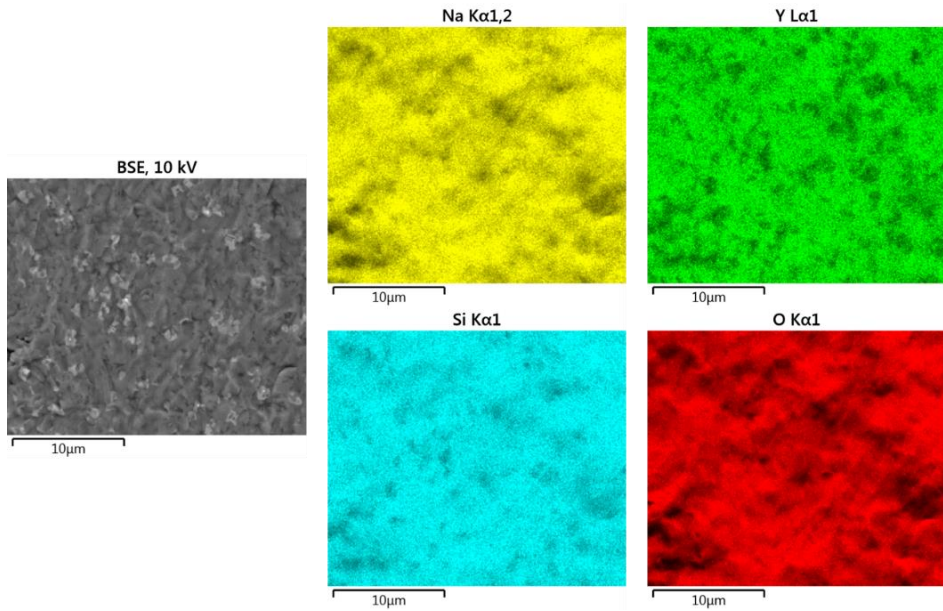


Figure 25 EDX analysis images of NYS tape.

4.3.2. Electrochemical performances

The impedance spectrum of NYS tape and the fitted impedance profile with an equivalent circuit is shown in **Figure 26**. The impedance spectrum can be fitted with an inductance (L_0) in series with two RC elements (here $R_1 + CPE1$ and $R_2 + CPE2$) and an additional constant phase element ($CPE3$), in which L_0 represents the inductance from the cables, $R_1 + CPE1$ ascribe to the resistance of the Na^+ ionic conduction in the bulk (i.e. grain), $R_2 + CPE2$ belong to the grain-boundary processes followed by a capacitive process ($CPE3$) associated with the electrode polarization, i.e., the NYS tape/Au interfacial capacitance (C_{inter}). The total resistance of 34Ω at RT comprised 18Ω for bulk resistance ($R_1 = R_{\text{bulk}} = 18 \Omega$) and 16Ω for grain-boundary resistance ($R_2 = R_{\text{gb}} = 16 \Omega$), indicating that the bulk and total Na^+ -ion conductivities are 1.9 and 1.0 mS cm^{-1} , respectively. The low frequency “spike” represents charge build-up at the blocking Au electrodes.[220] The attributions of each component in the equivalent circuit are summarized in **Table 8**. For comparison, the electrical and electrochemical performances of several representative Li^+ and Na^+ solid electrolytes are summarized in **Table 9**. The NYS tape exhibited comparable total ionic conductivity (1.0 mS cm^{-1}) with the reported polycrystalline NYS pellet (1.59 mS cm^{-1}).[142]

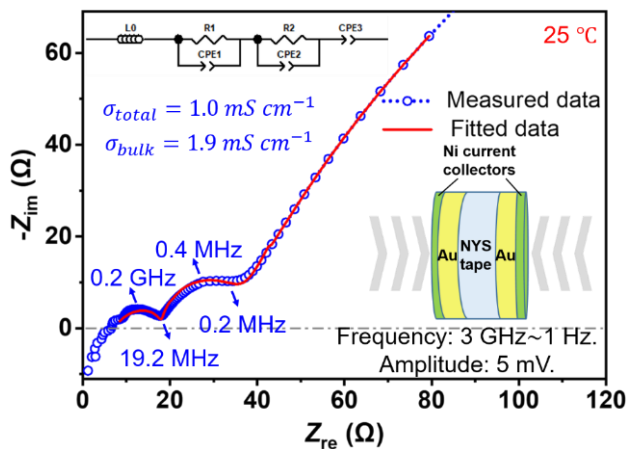


Figure 26 The Nyquist plot of measured and fitted impedance spectrum for NYS tape at RT.

The bulk and total resistances from the fitted data are 18 and 16Ω , respectively. The insets show the cell configuration and the equivalent circuit used for data fitting. The Au coating is applied as blocking electrodes and Ni sheets act as current collectors on both sides of the tape. The frequency range varies

between 3 GHz and 1 Hz, and the amplitude is 5 mV. The bulk and total conductivities of NYS tape are 1.9 and 1.0 mS cm⁻¹ at RT.

Table 8 The attributions of each component in the equivalent circuit are in **Figure 26**.

Component	L0 (H)	R1 (Ω)	R2 (Ω)	CPE1 (F)	CPE2 (F)	CPE3 (F)
Attribution	Inductance from cables	Bulk resistance	Grain-boundary resistance	Bulk capacitance	Grain-boundary capacitance	NYS tape Au interfacial capacitance
Value	1.0×10^{-8}	18	16	3.0×10^{-12}	3.3×10^{-8}	1.6×10^{-5}
Capacitance range from ref. [220]	/	/	/	10^{-12}	$10^{-11} \sim 10^{-8}$	$10^{-7} \sim 10^{-5}$

L: inductance; R: resistance; CPE: constant phase element.

Table 9 Comparison of ionic conductivity, activation energy and electrochemical stability window with representative Li⁺ and Na⁺ electrolytes, especially tape-cast samples.

Composition	Total σ_{RT} (mS cm ⁻¹)	E_a (eV)	Electrochemical window (V)	Refs.
Na ₃ Zr ₂ Si ₂ PO ₁₂ (NASICON) with 60Na ₂ O-10Nb ₂ O ₅ -30P ₂ O ₅ glass (5 ~ 10 wt.%) tape	0.44	/	/	[215]
Na-β"-Al ₂ O ₃ tape	180 (300 °C)	0.29	/	[214]
Na-β"-Al ₂ O ₃ tape	12 (200 °C)	/	/	[213]
Poly(acrylonitrile) (PAN)+ Na ₃ Zr ₂ Si ₂ PO ₁₂ composites	0.14	0.33	4.8 (vs. Na ⁺ /Na)	[221]
Li _{1.5} Al _{0.5} Ti _{1.5} P ₃ O ₁₂ (Li-NaSICON) tape	0.30	0.26	/	[206]
Cellulose-supported PPC solid polymer electrolyte (CPPC-SPE)	0.30	/	4.5 (vs. Li ⁺ /Li)	[222]
NYS pellet (950 °C/8 h; 1050 °C/36 h)	1.59	0.20	> 8 (vs. Na ⁺ /Na)	[142]
NYS tape (1100 °C/6 h)	1.0	0.30	> 8 (vs. Na ⁺ /Na)	This work

The temperature-dependent ionic conductivities are plotted in Arrhenius diagrams (**Figure 27**) and linearly fitted for the determination of the bulk and total activation energies of $E_{a\text{-bulk}} = 0.27$ eV and $E_{a\text{-total}} = 0.30$ eV, respectively, which are higher than that of the NYS pellet ($E_{a\text{-total}} = 0.2$ eV) [142] mainly influenced by high grain-boundary resistance in the NYS tape, which might be the influence of different grain-boundary conductivity of the samples prepared by another method, as well as amorphous or undesired secondary phase $\text{Na}_3\text{YSi}_2\text{O}_7$ (4.5%), which are not favorable for ionic conduction.

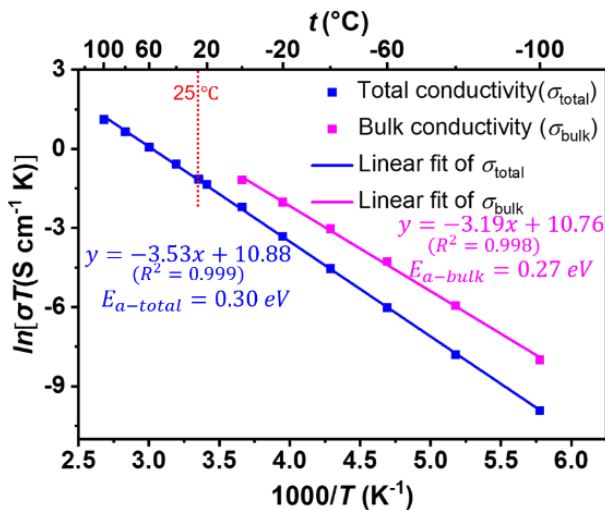


Figure 27 Arrhenius plots of bulk and total conductivities of the NYS tape.

Their activation energies calculated from the slopes of the fitted lines are $E_{a\text{-bulk}} = 0.27$ eV and $E_{a\text{-total}} = 0.3$ eV, respectively.

The electrochemical stability of the NYS tape was characterized by LSV (**Figure 28**), which suggests a stable electrochemical window up to 8 V vs. Na^+/Na electrode, much higher than polymer or composite electrolytes of below 5 V [107] without significant oxidation and with the perspective to be coupled with high voltage cathodes for high energy density SSSBs.

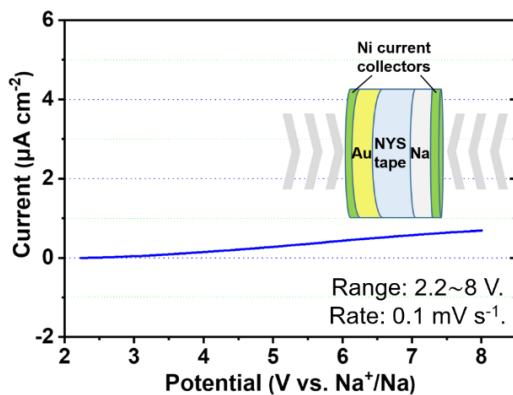


Figure 28 The LSV profile of NYS tape.

The inset shows the configuration of the cell with Na and Au as reversible and blocking electrodes on both sides of the tape. The voltage range varies between 2.2 and 8 V, and the scanning rate is 0.1 mV s^{-1} .

To investigate the feasibility of NYS tape as an electrolyte, symmetric cells with NYS tapes as electrolytes and Na metal as electrodes were assembled and tested, and their CCDs and galvanostatic cycling stability have been shown in **Figure 29** and **Figure 30**. The CCD value of NYS tape against Na metal electrodes is 2.2 mA cm^{-2} and the galvanostatic cycling time is over 280 h under the current density of 0.8 mA cm^{-2} without apparent overpotential, which indicates a stable Na^+ stripping/plating flux and shows the qualification of NYS tapes as the electrolytes and functional separators in SSSBs.

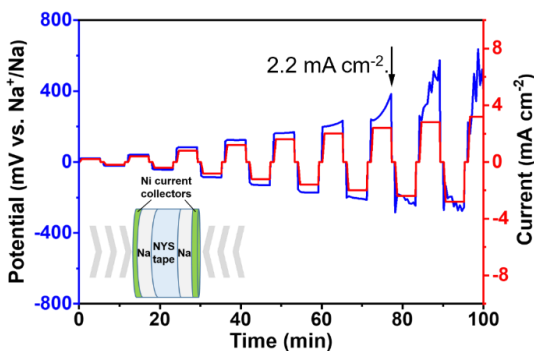


Figure 29 The profile of the CCD measurement of NYS tape.

The CCD value is 2.2 mA cm^{-2} . The inset shows the symmetric cell configuration for CCD and galvanostatic cycling stability measurements with Na metal as electrodes.

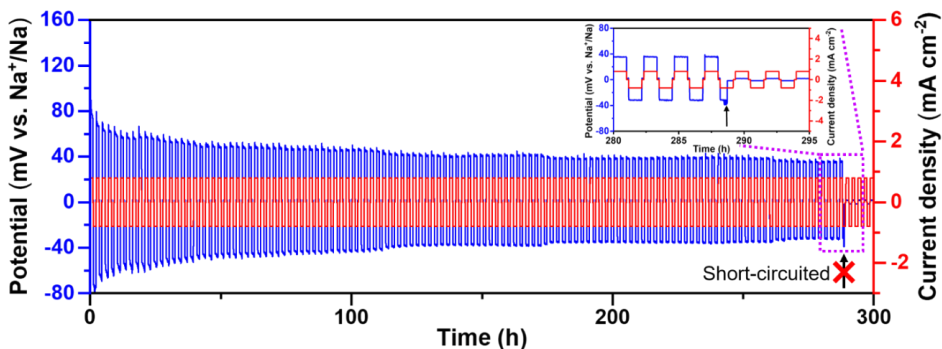


Figure 30 The profile of galvanostatic cycling stability measurement.

The applied current density is 0.8 mA cm^{-2} and the time of stable cycling is over 280 h. The inset is a magnified view of a part of the curves.

4.3.3. Mechanical properties and sintering behavior

Besides the conductivity and electrochemical window, the mechanical properties of the sintered NYS tape are of vital importance for solid electrolytes considering the planar configuration of SSBs which require pressure to ensure good contact between components for stable operation. The measurements of the hardness (H) and elastic modulus (E) of NYS tape have been performed by the nano-indentation method. The measurements are presented as nano-indentation curves with different loadings (250 and 500 mN) in **Figure 31**. The measured values of E have been evaluated according to Equation 1, which are summarized in **Table 10**. The H value of the NYS tape is almost 2 GPa and the E is nearly 45 GPa depending on the different loading. Compared with $\text{Li}_{1.5}\text{Al}_{0.5}\text{Ti}_{1.5}\text{P}_3\text{O}_{12}$ (LATP) and Al/Y-substituted NaSICON (see **Table 11**), NYS tape exhibited lower hardness and elastic modulus, which suggests accommodation of significant chemomechanical strain in the adjacent electrode materials and ensures good contact between the NYS tape electrolyte and the electrode.

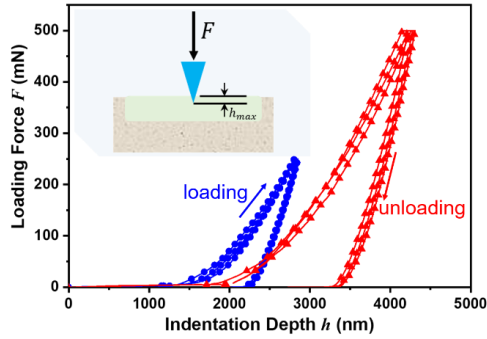


Figure 31 The nano-indentation curves for the loading-unloading cycles under 250 and 500 mN.

The test was repeated three times for each loading force. The elastic modulus and hardness were derived from the unloading part. The inset schematically shows the indenter tip pushed into the sample.

Table 10 Mechanical properties of NYS tape determined by nano-indentation method.

Loading force (mN)	Indentation depth h_{max} (nm)	Hardness H (GPa)	Elastic modulus E (GPa)
250	2850	1.926	45.07
500	4300	1.797	39.06

Table 11 Comparison of synthesis, thermal and mechanical properties with representative Li^+/Na^+ SSEs.

Composition	Processing method	Sintering condition	Mechanical properties	Refs.
$\text{Na-}\beta\text{-Al}_2\text{O}_3$ tape	Tape casting with ethanol/methylethylketone (MEK) as solvent.	1600 °C/2 h.	Ring-on-ring flexural strength: 144 ± 14 MPa.	[214]
$\text{Na-}\beta\text{-Al}_2\text{O}_3$ tape	Tape casting with ethanol/MEK as solvent.	1600 °C.	/	[213]

$\text{Li}_{1.5}\text{Al}_{0.5}\text{Ti}_{1.5}\text{P}_3\text{O}_{12}$ (LATP) tape	Tape casting with ethanol/MEK as solvent.	850 ~ 1000 °C / 1 h.	Nano-indentation: E : 109 GPa; H : 8.7 GPa.	[206]
$\text{Na}_{1+2x}\text{Al}_x\text{Y}_x\text{Zr}_{2-2x}(\text{PO}_4)_3$ and $\text{Na}_{3+2x}\text{Al}_x\text{Y}_x\text{Zr}_{2-2x}(\text{SiO}_4)_2(\text{PO}_4)$ pellets	Pechini method.	1150 ~ 1200 °C/5 ~ 10 h.	Indentation: E : 72 ~ 82 GPa; H : 4.8 ~ 5.8 GPa.	[223]
NYS tape	Aqueous tape casting.	Onset for shrinkage: 890 °C; 1100 °C/6 h.	Nano-indentation: E : 45 GPa; H : 2 GPa.	This work

The elastic modulus E of the NYS tape can be correlated with the equivalent modulus according to the unloading curve by using

$$\frac{1}{E_r} = \frac{1-\nu^2}{E} + \frac{1-\nu_i^2}{E_i} \quad (\text{Equation 26})$$

where E_i and ν_i are the elastic modulus and Poisson's ratio of the indenter material, respectively. A diamond indenter was used in the measurement and the parameters are $E_i = 1141$ GPa and $\nu_i = 0.07$ (given by equipment parameters). ν is the Poisson's ratio of the sample, which is assumed to be 0.25 (derived from the reported NASICON materials due to the chemical similarity of NYS and NASICON).[219] The shrinkage behavior of NYS tape was recorded in a dilatometer and is shown in **Figure 32**. The onset temperature for shrinkage is 890 °C. The most favorable sintering conditions for obtaining the dense NYS tape is 1100 °C for 6 h, which is lower than conventional NASICON (generally over 1200 °C) or Na- β/β' - Al_2O_3 electrolytes (over 1500 °C) (see **Table 12**). The shrinkage is about 15 ~ 19% in the x-y plane (i.e., in diameter for round tapes), yet 1 ~ 4% in the z-axis (i.e., in thickness). The shrinkage along the z-axis is not significant due to the uniaxial pressing of the tape.

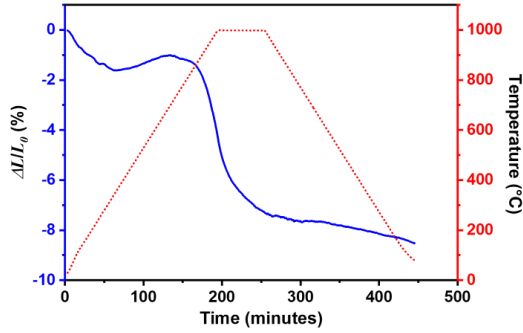


Figure 32 Shrinkage behavior of NYS tape.

The onset temperature of sintering is 890 °C.

Table 12 Shrinkage of the tapes during sintering.

Direction	Diameter (mm) (x-y plane)	Thickness (mm) (z-axis)
Before sintering	22.00	0.10 ~ 0.40
After sintering	17.80 ~ 18.65	0.10 ~ 0.38
Shrinkage	15 ~ 19%	1 ~ 4%

4.3.4. Fabrication of thin NYS tapes with tape casting

As one of the mature technologies for ceramic materials processing, tape casting is expected to be integrated into the production and fabrication lines for SSB materials, thus fostering the development and industrialization of SSBs. **Figure 33a** shows a green tape of NYS produced by tape casting, which has a uniform thickness of 50 μm , high flatness, and good ductility for easy trimming and stacking, which allows flexibility in tuning the size and thickness of electrolytes. **Figure 33b** shows sintered tapes with a very flat and uniform shape. The translucent feature illustrates the good densification of the thin NYS ceramic tapes ($\sim 120 \mu\text{m}$). The NYS tape was prepared by aqueous tape-casting after a simple ball-milling and calcining to produce the NYS precursor powder, which is relatively facile and inexpensive compared to other ionic conductor tapes, both in terms of raw materials and processing cost (see **Table 13**). The thin electrolyte sheets obtained by tape casting can facilitate the industrialization of SSBs.

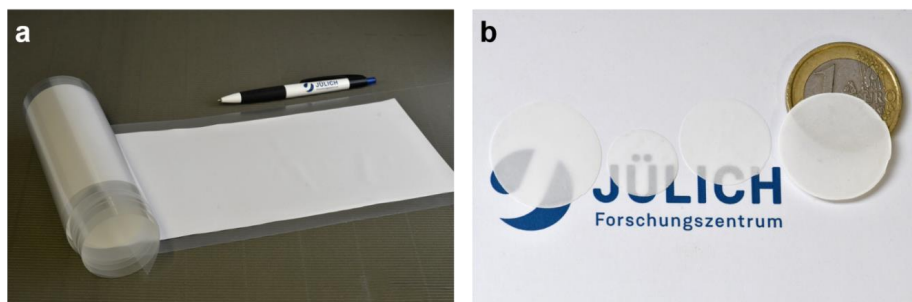


Figure 33 Digital pictures of (a) the green tape and (b) the translucent sintered NYS tapes.

Table 13 The cost comparison of representative Li^+/Na^+ SSEs tapes.

Composition	Raw materials	Precursor synthesis	Tape processing	Comments	Refs.
$\text{Na-}\beta\text{-Al}_2\text{O}_3$ tape	Na_2CO_3 , Li_2CO_3 and Al_2O_3	Two precursors of NaAl_5O_8 and LiAl_5O_8 : solid-state reaction at $1250\text{ }^\circ\text{C}$ for 2 h. Stoichiometrically ($\text{Na}_{1.67}\text{Al}_{10.67}\text{Li}_{0.33}\text{O}_{17}$) ball milling NaAl_5O_8 and LiAl_5O_8 for 4 h.	Ethanol/MEK, trichloroethylene/propyl alcohol and cyclohexanone as co-solvent and dispersants. Sintering at $1600\text{ }^\circ\text{C}$.	Two different kinds of precursors, organic solvents, were used for casting. More expensive.	[213]
$\text{Li}_{1.5}\text{Al}_{0.5}\text{Ti}_{1.5}\text{P}_3\text{O}_{12}$ (LATP) tape with SiO_2 additive	SiO_2 , Li_2CO_3 , $\text{Al}(\text{NO}_3)_3 \cdot 9\text{H}_2\text{O}$, $\text{Ti}[\text{OCH}(\text{CH}_3)_2]_4$ and LiH_2PO_4	Solution-assisted solid-state reaction. Calcined at $750\text{ }^\circ\text{C}$. Ball-milled for 24 h.	Ethanol/MEK as co-solvent. Sintering at $800 \sim 1000\text{ }^\circ\text{C}$ for 1 h.	Soluble raw materials are more expensive than common oxides and carbonates, organic solvents used for casting.	[206]
$\text{Na}_3\text{Zr}_2\text{Si}_2\text{PO}_{12}$ (NASICON) with $60\text{Na}_2\text{O}-10\text{Nb}_2\text{O}_5-30\text{P}_2\text{O}_5$ glass	NASICON: ZrO_2 , SiO_2 and $\text{Na}_3\text{PO}_4 \cdot 12\text{H}_2\text{O}$; glass: Na_2CO_3 ,	NASICON: Ball milling for 1 h and calcined at $1100\text{ }^\circ\text{C}$ for 12 h; glass: melting at $900\text{ }^\circ\text{C}$ for 0.5 h and quenching and grinding. Ball milling for 20 h.	2-propanol and toluene as co-solvent for casting; degreased at $400\text{ }^\circ\text{C}$ for 1 h and sintered at	The mixture of crystal and glass as precursors, organic solvents for casting and	[215]

(5 ~ 10 wt.%) tape	NaH ₂ PO ₄ ·2H ₂ O and Nb ₂ O ₅		900 ~ 1230 °C for 4 h.	high sintering temperature.	
NYS tape	Na ₂ CO ₃ ·H ₂ O, Y ₂ O ₃ and SiO ₂	Ball milling for 24 h and calcined at 950 °C for 5 h.	Aqueous tape casting. Sintered at 1100 °C for 6 h.	Easy- synthesized precursor from oxides and carbonates; water as solvents for casting.	This work

After screening for interface-compatible cathodes or modifying the cathode/electrolyte interface, the tape casting technique can be used for the continuous preparation of laminated configurations of electrolyte/interface/cathode, thus facilitating the production of NYS electrolytes or SSSBs.

4.4. Chapter conclusion

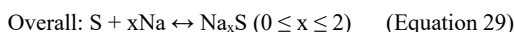
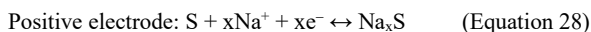
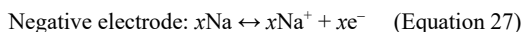
This work demonstrated the fabrication of silicate-based NYS electrolytes using an aqueous tape casting technique, which exhibited good Na⁺ ion conductivity ($\sigma_{RT} = 1.0 \text{ mS cm}^{-1}$) and mechanical properties (hardness H of 2 GPa and elastic modulus E of 45 GPa), the low activation energy for Na⁺ ion migration ($E_a = 0.30 \text{ eV}$), and a wide electrochemical stability window (over 8 V vs. Na⁺/Na). The high CCD value of up to 2.2 mA cm⁻² and stable galvanostatic cycling performance over 280 h under the current density of 0.8 mA cm⁻² and the capacity of 0.8 mAh cm⁻² verify the advantages of NYS tape as a suitable solid electrolyte. The aqueous tape casting technique promises environmental and operational safety and low preparation cost in scaling up, which pioneers an eco-friendly way for the continuous preparation of self-supported Na⁺ ion SSEs.

V. Pressureless All-Solid-State Na/S Batteries with Self-Supporting Na₅YSi₄O₁₂ Scaffold[‡]

5.1. Chapter introduction

In **Chapter IV**, silicate-based NYS Na⁺ superionic conductor sheets were fabricated[4] using the well-established tape casting technique. They exhibit good RT conductivity (1 mS cm⁻¹) and a wide electrochemical stability window (> 8 V vs. Na⁺/Na). However, some challenges still exist related to the utilization of NYS sheets in SSBs: the fabrication of thin but robust electrolytes, the construction of stable electrode/electrolyte interfaces and the selection of compatible cathodes.[79, 224] To tackle the aforementioned challenges, the well-established aqueous tape casting technique is employed to fabricate a porous/dense/porous NYS trilayered structure with scaffolds for the electrode materials.

The NYS layers with a total thickness of 300 ~ 400 μm provide the necessary ionic conductivity and stability, whereby the dense layer in the middle separates both electrodes and the porous layers on both sides accommodate the AMs. With high capacity and low-cost advantages, elemental sulfur is used as the cathode AM of choice[225] and coupled with a Na metal anode to create a Na/NYS/S battery that can operate at RT. The half- and overall-cell reactions are as follows:[60]



where the theoretical capacity (C_{th}) of 1675 mAh g_S⁻¹ is based on the fully sodiated state (Na₂S).[226, 227] In the following, the capacity is referred to the weight of sulfur (g_S⁻¹). In conventional Na/S batteries with liquid electrolytes, S and polysulfides dissolve into the electrolyte and then shuttle to the Na metal anode, resulting in a severe self-discharge behavior and continuous capacity degradation of the batteries.[225, 228-230] Furthermore, S as the cathode AM usually undergoes severe volume changes during charge and discharge so that the S electrode sheets manufactured by typical coating processing detach from the current collector inducing irreversible capacity loss.[226] In contrast, the dense NYS layer used here effectively prevents the shuttling of S and the open porosity present in the NYS scaffold additionally provides space for the volume swelling of S during sodiation while increasing the contact area between S and NYS electrolyte. For the infiltrated Na metal anode, the NYS porous structure can be coated with Pb to effectively improve the interfacial wettability between Na and NYS.[231] This reduces the interfacial impedance, increases the contact area and distributes the local current.

[‡] Content of this section has been published in *Carbon Energy* (DOI: 10.1002/cey2.371).

Therefore, the main benefits of porous/dense/porous NYS trilayered scaffold structure fabricated by aqueous tape casting are as follows: 1) stable interfaces between the electrode AMs and the NYS electrolyte enable pressureless Na/NYS/Na symmetric cells and Na/NYS/S full cells with good cycling stability; 2) the porous structure provides a host for the S composite cathode while increasing the contact area and improving the utilization rate; 3) the thin Pb-coating of the porous NYS scaffold effectively improves its wettability with Na metal[231] and distributes the local current; 4) the aqueous tape casting process used for the fabrication of NYS ceramics is eco-friendly and has the potential for scale-up. This work presents a promising design for pressureless ceramic-based Na/S batteries and provides a new paradigm for the development of cheap and reliable ASS-SMBs. It also shows for the first time the application of NYS in a realistic cell design beyond the generic use of ceramic pellets.[142, 232]

5.2. Experimental

5.2.1. Fabrication and synthesis

Preparation of $\text{Na}_5\text{YSi}_4\text{O}_{12}$ precursor for tape casting: The raw materials $\text{Na}_2\text{CO}_3 \cdot \text{H}_2\text{O}$ (Aldrich, 99 %), Y_2O_3 (VWR, 99.999 %), SiO_2 (Honeywell Fluka, 99 %, 1 ~ 5 μm) were mixed in a stoichiometric ratio and milled with ZrO_2 balls (3 mm and 5 mm in diameter, 200 rpm) and ethanol as a dispersant for 24 h. After ball-milling, the mixture of raw materials was heated in an oven (60 °C for 24 h) in flowing N_2 . The white powder was calcined at 950 °C for 5 h in air. Then, the calcined powder was roughly ground in an agate mortar and subsequently ball-milled for 24 h to decrease the particle size of the NYS precursor for the subsequent fabrication of the NYS tape. Part of the NYS precursor was sintered at 1100 °C for 6 h in air to obtain the pure NYS phase and then ball-milled to obtain fine particle sizes as an additive in the S composite cathode.

Fabrication of porous and dense NYS tapes: The aqueous slurry for dense and porous tapes was prepared by mixing methylcellulose (MC, Alfa Aesar), polyethylene glycol (PEG, Merck) and glycerol (Merck, 99%) in deionized water with the assistance of a stirrer (IKA, RET Basic). Then the finely ground NYS precursor powder was added to the slurry. For the preparation of the porous tape, spherical polymethylmethacrylate (PMMA, Merck) particles with an average diameter of 100 μm were admixed to the slurry acting as a pore former. Both suspensions for dense and porous layers were homogenized in a vacuum ($\sim 10^4$ Pa) with ZrO_2 balls (5 mm in diameter) in a planetary mixer (Thinky, ARE-500) at 1000 rpm for 10 minutes to form uniform slurries for the subsequent casting step. The mixed slurries were individually transferred to the slurry reservoir of the tape-casting machine and then cast on a Mylar substrate using a height-adjustable doctor blade. The optimized parameters were 400 μm in thickness (i.e., the slit width) and 10 mm s^{-1} casting

speed. After drying naturally at RT overnight, the dense and porous green tapes were easily peeled off the Mylar substrate. The obtained green tapes were thin and flexible and could be punched into the desired round-shaped samples with varying diameters and laminated into multilayer structures. Each piece of tape was first pressed with 60 MPa at RT for 2 minutes to improve the green density, which to some extent can break and flatten the PMMA spheres in the porous tapes. Then, these pressed tapes were laminated together to obtain the porous/dense/porous trilayered structure by subsequent warm-pressing at 80 °C with 120 MPa for 2 minutes. Finally, the laminated tapes were sintered in air with a heating rate of 60 °C h⁻¹ until 600 °C for 1 h to decompose the organic additives followed by a heating rate of 180 °C h⁻¹ up to 1100 °C for 6 h to densify the tapes. During sintering, the green tapes were placed between two sintered NYS pellets prepared with the same raw powder. This prevented the tapes from bending into a bowl shape and sticking to the substrate during the sintering process.

Preparation of S composite cathode paste: Polyvinylidenfluorid (PVDF, $M_w = 600000$, Sigma-Aldrich) powder was dissolved in N-methyl-2-pyrrolidone (NMP, Merck) under magnetic stirring (IKA, RET Basic). The PEO ($M_w = 200000$, Alfa Aesar) powder was added to acetonitrile (Merck) and agitated until completely dissolved. The anhydrous NaClO₄ powder (Alfa Aesar) was then added to the PEO solution with the molar ratio of EO: Na⁺ = 10:1. Both solutions were mixed and stirred until homogeneity was achieved. The elemental sulfur powder (Alfa Aesar) as the AM, the carbon black of super P (Alfa Aesar) as the electronic conductor and NYS powder with pure phase as the bi-functional plasticizer to decrease the crystallinity of PEO chains and increase the Na⁺ ionic conductivity were added into the solution and mixed with stirring for 6 h to get a uniform and concentrated paste. Different weight fractions of S (20, 32, 40, 50, 60 wt.%) in the composite cathode were fabricated (see **Table 14**). The last step was homogenization in a high-speed mixer device (Thinky, ARE-500, 1500 rpm for 10 minutes) to completely mix the paste.

Table 14 Formulations of the composite cathodes with different S content.

Item	Mass of individual component (wt%, 2 g in total)																		
	S-20%		S-32%		S-40%		S-50%		S-60%										
-	Ratio/ wt%	Mass/ g	Ratio/ wt%	Mass/ g	Ratio/ wt%	Mass/ g	Ratio/ wt%	Mass /g	Ratio/ wt%	Mass /g									
S	20	0.4	32	0.64	40	0.8	50	1.0	60	1.2									
Super P	25	0.5	20	0.4	15	0.3	10	0.2	7	0.14									
PVDF	8	0.16	8	0.16	8	0.16	8	0.16	8	0.16									
PEO	90	47	90	40	90	37	90	32	90	25									
											0.658		0.56		0.518		0.448		0.35
NaClO ₄											0.188		0.16		0.148		0.128		0.1
NYS	10	0.094	10	0.08	10	0.074	10	0.064	10	0.05									

Fabrication of symmetric and full cells: (1) For the Na/NYS/Na symmetric cells, both porous sides of the NYS scaffold were sputter-coated with a Pb layer (Pb target: Micro to Nano, 70-PB5708; Cressington sputter coater 108auto series) to ameliorate the wettability between Na metal and NYS ceramic. The Pb layer was sputtered at a current of 20 mA for 120 s, which gives rise to a uniform Pb coating with a thickness of 50 nm. The weight ratio of Pb in the Na anode side is about 5 wt.% (0.1 mg Pb and 2.0 mg Na). The diameter of the sintered NYS scaffold varied between 10 and 14 mm (usually 12 mm). The Na metal was heated to melt (120 – 150 °C) in a glass bottle, then the liquid Na metal was pipetted and dropped on both sides of the Pb-coated NYS scaffold. The melting and dropping of the Na metal were conducted in an Ar-filled glovebox (Glovebox System, Germany; $p(\text{O}_2) < 1.0$ ppm and $p(\text{H}_2\text{O}) < 0.5$ ppm). Once the Na metal had solidified, the Al foils (Dezhi Company, Shenzhen, China; 0.01 mm in thickness) were attached on both sides as current collectors and mounted in a pouch cell with aluminum-plastic film (Dezhi Company, Shenzhen, China) and sealed in the glove box. (2) For the assembly of the full cells, one side of the NYS scaffold was coated with a Pb layer to accommodate Na metal as an anode. The other side filled with the prepared S composite cathode paste was poured and gently squeezed into the porous layer. An excess of paste was gently scraped off. The filled scaffold was dried naturally (48 h) in a ventilated hood to remove the solvents. The areal loading of S was calculated from the mass difference before coating and after complete drying which is usually in the range of 0.9 ~ 1.0 mg cm⁻². The procedure of loading the Na anode was the same as in the case of symmetric cells.

5.2.2. Characterization

Crystal structure characterization: The crystal structure of the as-prepared NYS scaffold was determined by XRD (Bruker D4 Endeavor) with Cu K_α radiation. The refinement of the XRD pattern was carried out with Fullprof Suite software to get the detailed lattice parameters of the unit cell. The XRD sample was NYS powder, which was ground in an agate mortar from the as-sintered NYS trilayer.

Morphological characterization: The microstructure of the NYS scaffold was analyzed with SEM (Hitachi TM3000). The NYS scaffold was coated with a thin Au layer to improve electrical contact before being transferred to the sample chamber.

The pore volume of the porous layer in the NYS scaffold was determined with Archimedes' method. The sintered NYS scaffold was immersed in liquid propanol for 24 h and then weighed after removing the propanol residuals on the surface. The density of propanol at RT was 0.8034 g cm⁻³.

Particle size measurement: The particle size measurement was conducted with a laser-scattering particle size distribution analyzer (HORIBA, LA-950). The particle size distribution of the NYS precursor powder after calcination is shown in **Figure 34**.

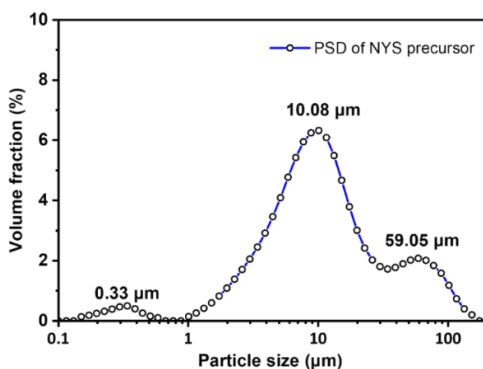


Figure 34 Particle size distribution measurement of NYS precursor.

Electrochemical measurements: All electrochemical performance tests were performed with an electrochemical workstation (BioLogic VMP300, France) equipped with climate chambers (Vötsch, VT4002) to adjust the temperature. The a.c. impedance measurements of the Na/NYS/Na symmetric cells were performed in the frequency range from 7 MHz to 1 Hz with an alternating voltage amplitude of 5 mV. The fitting of the impedance data was carried out with Zview software (Scribner Associates Inc.). The temperature-dependent impedance spectra were recorded between $-20\text{ }^{\circ}\text{C}$ and $80\text{ }^{\circ}\text{C}$ and then plotted in an Arrhenius diagram to determine the E_a of Na^+ ionic conduction. The CCD was measured with Na/NYS/Na symmetric cells by gradually increasing the current density at RT. The cycling stability of the Na/NYS/Na cells was measured with galvanostatic cycling at 1.3 mA cm^{-2} and 1.3 mAh cm^{-2} . The signals occurring during cyclic voltammetry were recorded between -0.5 V and 8 V (vs. Na^+/Na) with a scanning rate of 0.01 mV s^{-1} to obtain the electrochemical window of the Au/NYS/Na cell (Au as the cathode and Na as the anode), in which the Au was coated with a sputter coater device (20 mA applied current; 150 s coating time). The long-term galvanostatic charge and discharge performance of the Na/NYS/S full cells were tested in the voltage range of 1.0 V to 3.3 V vs. Na^+/Na whereas 3.5 V were applied for the test at different current densities (from 0.017 to 3.4 mA cm^{-2}). The impedance spectra of the full cell were measured with the same setting as in the case of the symmetric cells. The CV curves at the different scanning rates from 0.01 mV s^{-1} to 100 mV s^{-1} were recorded in the range of 1.0 V to 3.5 V vs. Na^+/Na . The electronic conductivity of the composite cathode was characterized using Ni/composite cathode/Ni symmetric cells by applying a constant voltage of 0.1 V and recording the current. The electronic conductivity can be calculated according to Ohm's law using the constant current value. The Na^+ ionic conductivity of the composite cathode was measured with symmetric cells composed of NYS dense tape/composite

cathode/NYS dense tape. The NYS dense layers act as Na^+ ion reversible electrodes and electronically blocking electrodes to eliminate the contribution of electronic conduction.

5.3. Results and discussion

5.3.1. Fabrication, microscopic and crystal structure of NYS trilayer

The NYS precursor was prepared using a ball-milling process followed by heat treatment, as shown in **Figure 35**. For the following tape casting, the NYS precursor was mixed with a binder and plasticizer. The porous layers required the addition of a pore former. Here spherical polymethyl methacrylate (PMMA) beads were used to prepare the porous layers. The NYS and NYS/PMMA green tapes were laminated together before co-sintering. The slurry preparation and the sintering protocol followed the preparation of dense tapes of NYS.[4]

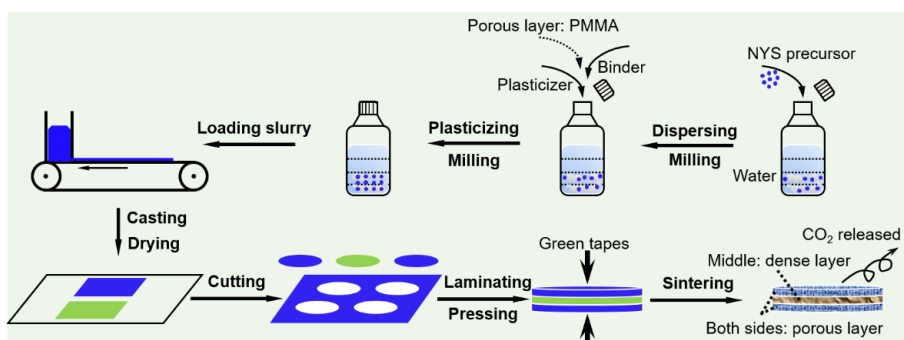


Figure 35 Schematic processing steps of the preparation of NYS trilayers: milling of the raw materials, casting the slurries, drying, cutting, laminating, pressing and sintering the green tapes.

The microstructure (**Figure 36a**) of the sintered tapes shows that the dense and porous layers are very tightly joined, which facilitates the rapid migration of Na^+ ions in the NYS phase and results in a robust mechanical scaffold with good flatness due to the symmetric geometry of the laminates. The thicknesses of the dense and porous layers were 90 μm and 170 μm after sintering, respectively. The dense layer (**Figure 36b**) can effectively support the entire trilayered laminate and separates both electrodes due to the high hardness (2 GPa) and elastic modulus (45 GPa), which is sufficient to maintain excellent mechanical

properties during cycling.^[16] The micron-scale interconnected open pores in the porous layer (**Figure 36c**) can accommodate electrode AMs and simultaneously provide continuous Na⁺ ionic transport pathways. The pore volume in the porous layer is about 68% as determined by Archimedes' method and very suitable for infiltration.

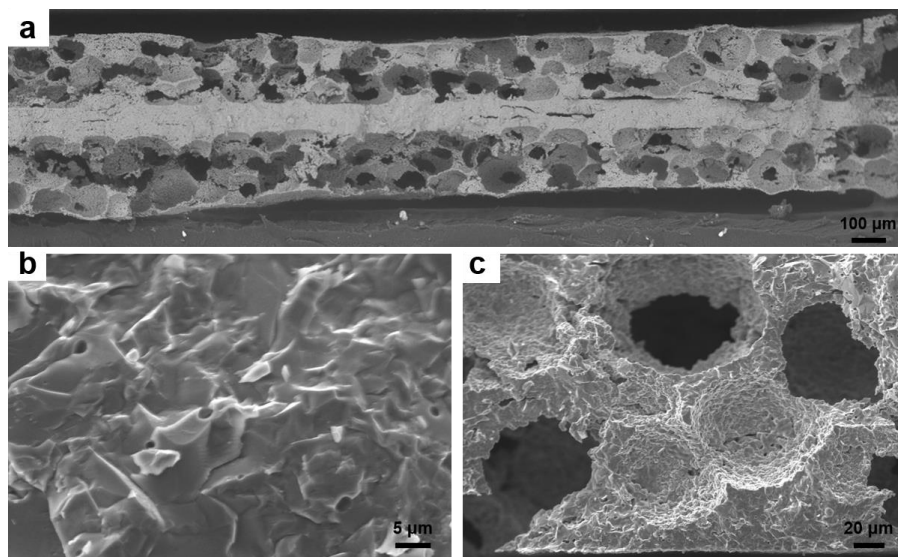


Figure 36 (a) Cross-sectional SEM image of the NYS trilayered structure, (b) and (c) magnified SEM images of the dense and porous layer, respectively.

The NYS phase crystallized in rhombohedral symmetry with a space group of $R\bar{3}c$, which is revealed by the XRD pattern (**Figure 37a**) and Rietveld refinement (refined parameters of the unit cell shown in **Figure 37b** are listed in **Table 15**). An explanation for the appearance of the secondary phases is described below.

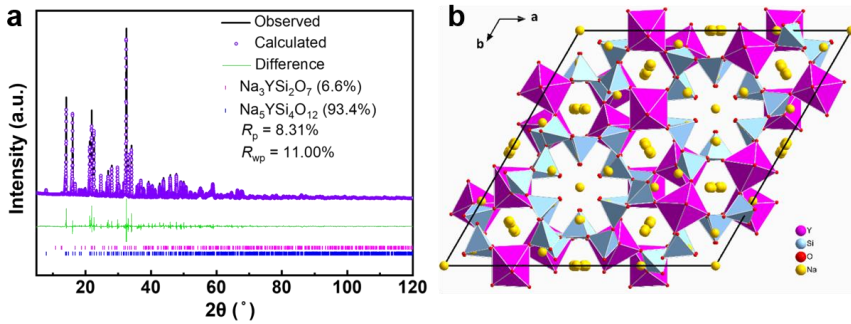
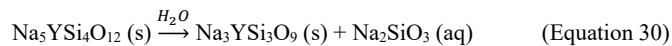


Figure 37 (a) Refined XRD pattern after tape casting and sintering and (b) projection of crystal structure along the c-axis.

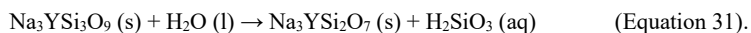
Table 15 The parameters of NYS unit cell from refined XRD data.

Space group	a (Å)	c (Å)	V (Å ³)
Rhombohedral phase, $R\bar{3}c$	22.0190	12.6050	5292.6

Secondary phases should be analyzed. During tape casting, NYS powder was mixed with water and slowly reacted to non-conducting secondary phases, like $\text{Na}_3\text{YSi}_2\text{O}_7$ (ca. 5 wt%), which is ascribed to the following stepwise reactions:



and



The reaction products Na_2SiO_3 and H_2SiO_3 stuck to the surface of the milling balls and the container due to their high viscosity. Therefore, except for the main phase NYS, there are approximately 5 wt% secondary phases, like $\text{Na}_3\text{YSi}_2\text{O}_7$.

5.3.2. Electrochemical performance of Na/NYS/Na symmetric cells

The as-prepared NYS scaffold was used to assemble Na/NYS/Na symmetric cells to evaluate Na^+ ionic conductivity with impedance spectroscopy. Different from the determination of the electrode area of dense

NYS tapes, the precise contact area between Na metal and electrolyte and the influence of tortuosity in the porous layers is difficult to analyze. As a simplified approach to obtain comparable values of conductivity, the total thickness of the NYS scaffold and the planar area based on the tape diameter are used for the calculation of conductivity. The total ionic conductivity σ_{total} (sum of conductivities of bulk and grain boundaries) of the NYS scaffold is 1.0 mS cm^{-1} at RT, which corresponds to the first semi-circle in the fitted impedance spectra (**Figure 38a, 38b**). The values of the individual components of the fitted impedance spectra are listed in **Table 16**. The area-specific resistance (*ASR*) of the NYS trilayer is only $43 \text{ } \Omega \text{ cm}^2$ based on the following equation:[233]

$$ASR = \frac{l}{\sigma} \quad (\text{Equation 32})$$

where l is the thickness and σ is the conductivity of the electrolyte. For the pristine NYS scaffold in the symmetric cell, the interfacial resistance ($R_{\text{interface}}$) is as high as $5000 \text{ } \Omega \text{ cm}^2$ (**Figure 38a**) derived from the second semi-circle in the fitted impedance spectrum. In contrast, the $R_{\text{interface}}$ is reduced to $25 \text{ } \Omega \text{ cm}^2$ (**Figure 38b**) for the Pb-coated NYS scaffold. This is attributed to the significantly improved interfacial wettability of Na metal on the Pb-coated NYS,[231, 234, 235] which was confirmed by the contact angle test (**Figure 38c**). The Pb coating on the NYS reduces the initial contact angle between Na metal and NYS from 109° to 41° . In the analogous Na/Pb-coated NYS/Na symmetric cell, the temperature-dependent total conductivity is used to derive an Arrhenius plot (**Figure 38d**), and the fitted activation energy (E_a) for Na^+ ion conduction is 0.29 eV , the same value as previously reported.[4]

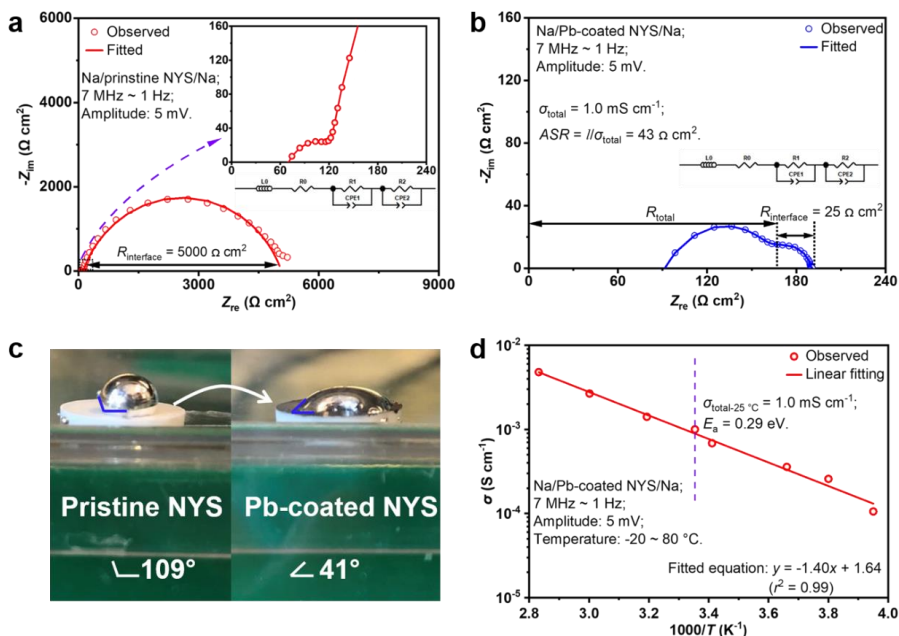


Figure 38 Electrochemical performance of NYS scaffold in Na/NYS/Na symmetric cells and Na/NYS/Au cells.

Nyquist plots of Na/NYS/Na cell with (a) pristine NYS scaffold and (b) Pb-coated NYS scaffold. Insets show the magnified spectrum at high frequencies and the equivalent circuit for fitting. (c) Contact angle measurement for pristine and Pb-coated NYS scaffold with Na metal in the glovebox. (d) Arrhenius plot of the temperature-dependent conductivities in the Na/NYS/Na symmetric cell with linear fitting between $-20\text{ }^{\circ}\text{C}$ and $80\text{ }^{\circ}\text{C}$.

Table 16 Values of the individual equivalent circuit elements of the fitted impedance spectra of Na/NYS/Na cells.

Item	L0 (H)	R0 (Ω)	R1 (Ω)	CPE1 (F)	R2 (Ω)	CPE2 (F)
Figure 38a	2.9×10^{-7}	69	45	6.1×10^{-11}	4952	1.3×10^{-6}
Figure 38b	5.6×10^{-7}	90	77	8.9×10^{-10}	25	4.7×10^{-6}

Attribution	Inductance from cables	Bulk resistance	Grain-boundary resistance	Grain-boundary capacitance	Na/NYS interfacial resistance	Na/NYS interfacial capacitance
Capacitance range from ref.[220].	-	-	-	$10^{-11} \sim 10^{-8}$	-	$10^{-7} \sim 10^{-5}$

The CCD at RT is measured by gradually increasing the current density in a symmetric cell until the polarization voltage significantly fluctuates and the cell is short-circuited. The CCD in Na/NYS/Na symmetric cells with NYS scaffold is 3.0 mA cm^{-2} (**Figure 39**) against Na metal, which is higher than the previously reported CCD with dense NYS tapes[4] and sheets[142] (both are 2.2 mA cm^{-2}). This is attributed to the good ionic conductivity and the increased contact area in the Pb-coated NYS scaffold. However, an increasing voltage spike occurs starting at the current density of 1.3 mA cm^{-2} , which can be explained by the rate of Na^+ ion transport in the vicinity of the Na/NYS interface. At low current density ($< 1.3 \text{ mA cm}^{-2}$), the rate of Na^+ ion depletion is lower than the Na metal diffusion at the stripping side. This leads to low Na vacancy concentration at the interface and maintains good contact and there is no significant irregular voltage signal. However, when the current density increases, the rate of Na metal diffusion cannot compete with the Na^+ ion depletion leading to vacancy clustering and void formation at the interface, which causes a sharp voltage increment at the beginning of each cycle. When stripping and plating are reversed, the polarized voltage increases gradually with the return transport of the deposited Na metal and here voids also appear near the interface. Therefore, in the high current density region, the polarized voltages of the first half cycle and the second half circle show opposite trends.

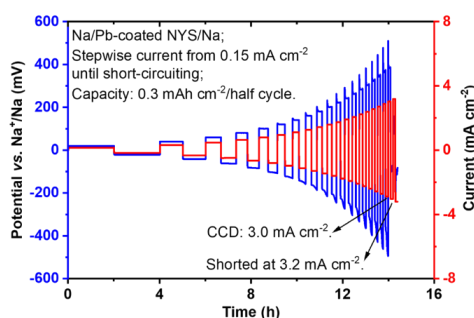


Figure 39 CCD measurement with stepwise increase of the current density until short-circuiting.

The electrochemical stability window of stripping/plating for Na^+ ions was tested by CV in Na/NYS/Au cells (**Figure 40**), showing a wide stability range of over 8 V (vs. Na^+/Na). The sharp redox peaks between -0.5 V and 0.5 V vs. Na^+/Na suggest no visible side reactions between Na metal and NYS and high reversibility.

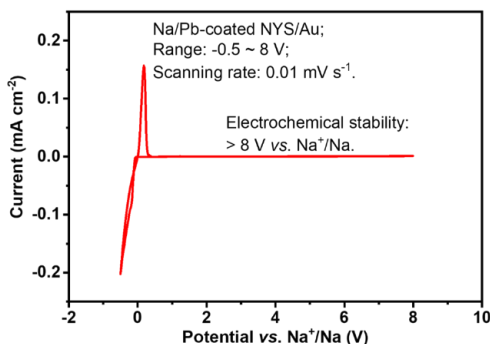


Figure 40 CV profile in the range of -0.5 V to 8 V vs. Na^+/Na in the Na/NYS/Au cell with a scanning rate of 0.01 mV s⁻¹.

The galvanostatic stability indicates that the NYS scaffold easily sustains 460 h cycling (**Figure 41**) at a current density of 1.3 mA cm⁻² and a capacity of 1.3 mAh cm⁻² without obvious fluctuation of the voltage. This cycling stability is better than that of the reported NYS dense tapes[4] resulting from the increased contact area and improved interfacial wettability between Na and NYS scaffold. Furthermore, a cycling stability test at 2.4 mA cm⁻² and 2.4 mAh cm⁻² (**Figure 42**) was also conducted to show its practical viability at higher current density, but cycling failed after the 15th cycle. The potential curve is not as stable as at a lower current density (1.3 mA cm⁻²) and the obvious voltage fluctuation after the 15th cycle can be explained by the increased amount of Na metal involved in the plating/stripping processes and the increased tendency of void formation at the interface.

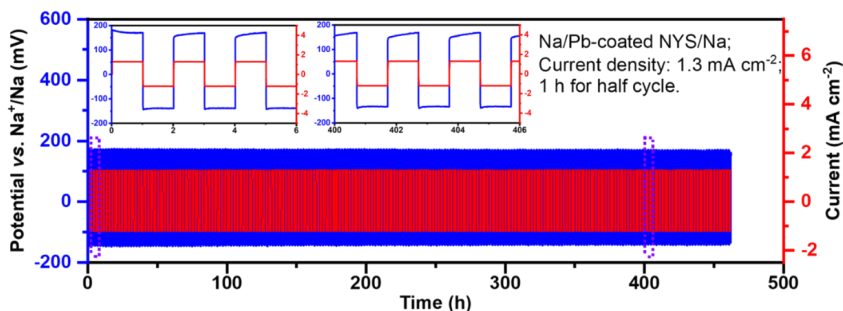


Figure 41 Galvanostatic cycling performance of the Na/NYS/Na symmetric cell at the current density of 1.3 mA cm^{-2} and capacity of 1.3 mAh cm^{-2} .

Insets show the magnified profiles in the time intervals of 0 ~ 6 h and 400 ~ 406 h.

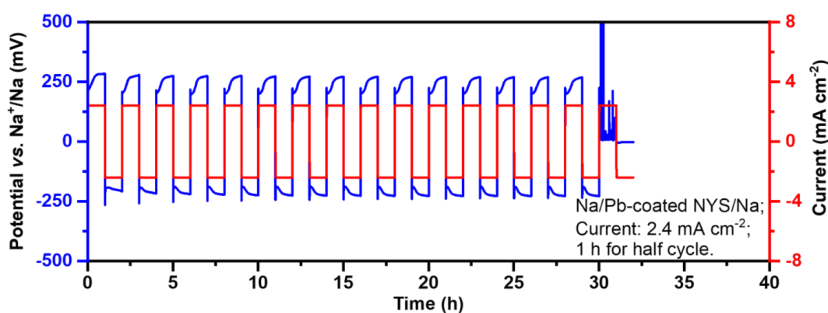


Figure 42 Cycling performance of a symmetric cell at the current density of 2.4 mA cm^{-2} .

5.3.3. Electrochemical performance of the Na/NYS/S full cells

As in a Na/NYS/Na symmetric cell, where the molten Na metal was infused into the porous layer, the composite S cathode paste was squeezed into the porous layer and dried to remove the solvent. Considering the very poor electronic and ionic conductivity of S, the optimal S content was optimized by changing the ratio of conducting additives and S in the composite cathode. The performance of the composite cathode with different S contents was evaluated by measurements of electronic conductivity (**Figure 43**), ionic conductivity (**Figure 44**) and specific discharge capacity (**Figure 45**). The results are summarized in **Table 17**. By increasing the mass of S in the composite cathode, the electronic conducting additive (super P) and ionic conducting additive [polyethylene oxide (PEO) + NaClO_4 + NYS] were decreased correspondingly.

The trade-off between the conductive additives and the S content revealed that a cathode with 32 wt.% showed optimal performance. The XRD patterns with different S contents (**Figure 46**) further indicate that the crystallinity of PEO in the composite cathode increased with a higher S content, which is unfavorable for Na⁺ ionic conduction in the composite cathode.

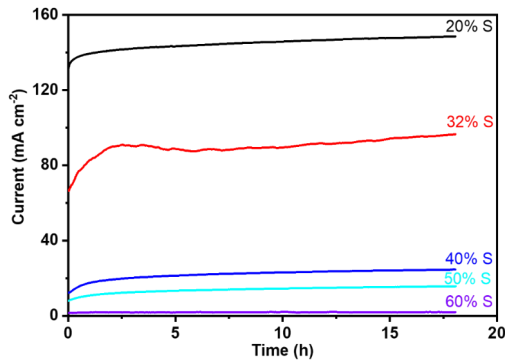


Figure 43 DC polarization curves of the composite S cathode with different S ratios to measure the electronic conductivities.

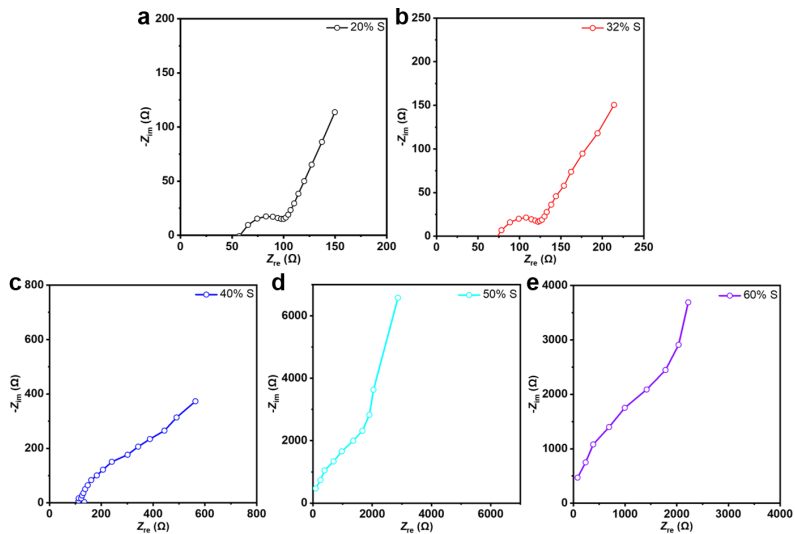


Figure 44 Nyquist plots of the composite cathodes with different S contents.

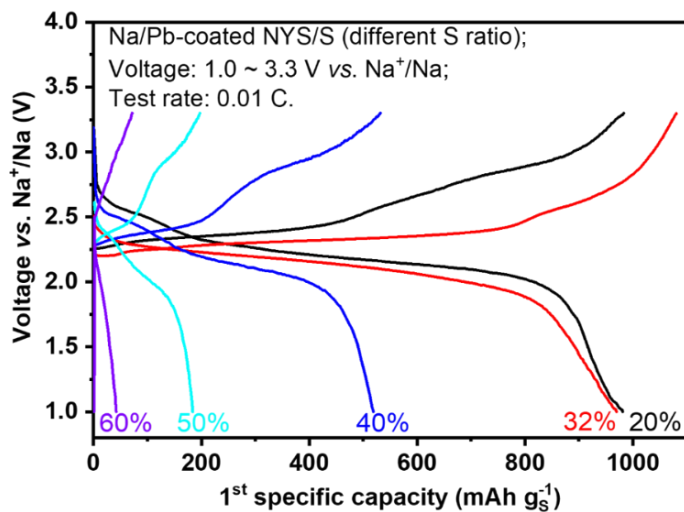


Figure 45 Discharge/charge curves of the 1st cycle for the different composite S cathodes.

Table 17 Summary of the conductive and capacity performance of the composite cathodes with different S contents.

S content /wt%	Electronic conductivity /mS cm ⁻¹	Ionic conductivity /mS cm ⁻¹	1 st cycle discharge capacity /mAh g _s ⁻¹
20	1480	0.89	981
32	960	0.74	970
40	240	0.29	519
50	150	0.053	184
60	14	0.043	42

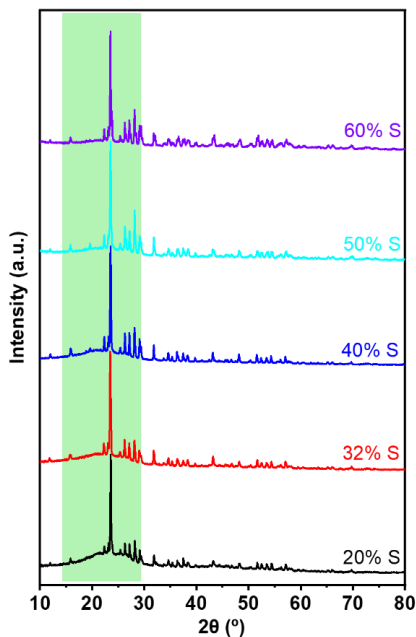


Figure 46 XRD patterns of the composite cathode with varying S content.

The green region of the diffraction angles shows the decreasing intensity of the amorphous PEO with increasing sulfur content.

In the Na/NYS/S full cell, the galvanostatic discharge/charge measurement (**Figure 47a**) at a current density of 0.017 mA cm^{-2} (equivalent to 0.01 C) with a cathode loading of 1.0 mg cm^{-2} shows that the highest discharge capacity is 970 mAh g^{-1} (based on the mass of S, equivalent to the areal capacity of 1.0 mAh cm^{-2}), which is 42% lower than the C_{th} of S. The lower specific discharge capacity reflects the fact that part of the S in the composite cathode is either not sufficiently accessed to be electrochemically active or not completely reduced to Na_2S . [236] The impedance spectra of the full cell at open-circuit voltage (OCV) indicate that the $R_{\text{interface}}$ are $94.0 \text{ } \Omega \text{ cm}^2$ and $327.6 \text{ } \Omega \text{ cm}^2$ (**Figure 47b**) resulting in a total resistance of the full cell of $500 \text{ } \Omega \text{ cm}^2$. The $R_{\text{interface}}$ of the cathode side of the full cell is also evidenced by the high overpotential in **Figures 47a, 47c** and **47d**. There are two discharge plateaus, located at $\sim 2.5 \text{ V}$ and $\sim 2.2 \text{ V}$ (vs. Na^+/Na), and the latter region contributes to the majority of the capacity with a relatively smooth voltage decrease. The higher discharge potential vanishes with increasing cycle numbers. During the charging process, there are also two visible plateaus at 2.4 V and 2.7 V (vs. Na^+/Na , mean voltage), and the

latter charge voltage increases towards 2.9 V with an increasing number of cycles. The multiple discharge/charge plateaus indicate a stepwise reaction of S in the Na/NYS/S full cells.

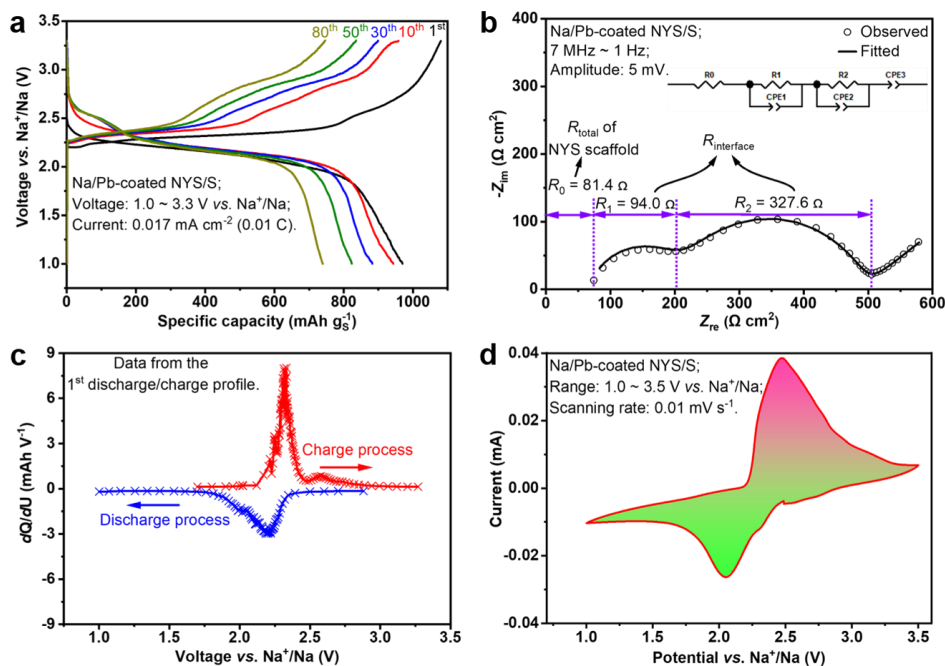


Figure 47 Electrochemical performance of Na/NYS/S full cells.

(a) Galvanostatic discharge and charge profiles at a rate of 0.01 C in the range of 1 ~ 3.3 V vs. Na⁺/Na. (b) Impedance spectrum of the full cell. The inset shows the equivalent circuit for data fitting. (c) The differential capacity curve from the 1st discharge and charge profile in **Figure 47a**. Q and U denote capacity and voltage, respectively. (d) CV profile at a scanning rate of 0.01 mV s⁻¹ between 1.0 V and 3.5 V vs. Na⁺/Na.

To analyze the equilibrium potential of the full cell from a thermodynamic perspective, the differential capacitance curve (dQ/dU vs. U; **Figure 47c**) was plotted. It shows that the equilibrium potentials of the charging and discharging states are 2.32 V and 2.21 V, respectively. This is also evidenced by the CV curve of the full cell (**Figure 47d**). The oxidation (i.e. charge process) peak occurs at around 2.47 V (vs. Na⁺/Na)

and the reduction (i.e. discharge process) peak at around 2.05 V (vs. Na^+/Na). The polarization voltage of 0.42 V between the charging and discharging process results from the kinetic barriers for the migration of Na^+ ions and electrons at the interfaces in the composite cathode.[237, 238]

To study the kinetics of the S composite in the discharge and charge processes, CV curves were recorded at different scanning rates (**Figure 48a**). The plot of the peak current i_p versus the square root of the scanning rate shows a linear relationship (**Figure 48b**), indicating good reversibility of the full Na/NYS/S cell.[60, 61] As the scanning rate increases, the polarization voltage also increases and the system changes from a reversible to a quasi-reversible state, indicating that electronic conductivity limits the kinetic properties of the S composite.

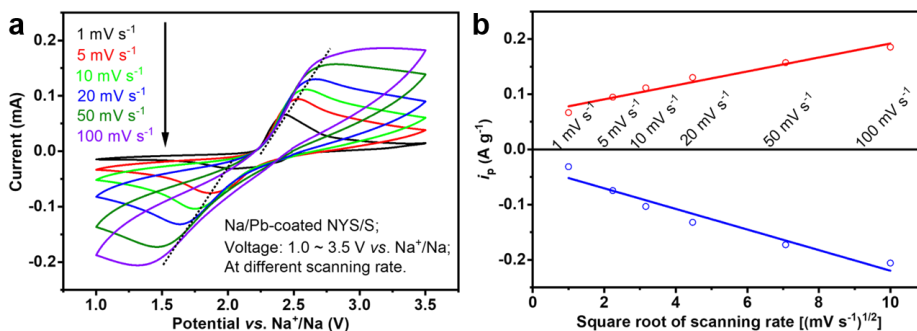


Figure 48 (a) CV profiles at different scanning rates from 1 mV s^{-1} to 100 mV s^{-1} in the range of 1.0 V to 3.5 V vs. Na^+/Na . (b) Relationship between peak current i_p and the square root of the scanning rate.

The C-rate performance was tested between 0.01 C and 2 C in the full cell (**Figure 49a**). The applied current at different C-rates correlates to the areal current based on the practical S loading in the full cell (shown in **Table 18**). Stating from 0.01 C, the discharge capacities are between 950 $\text{mAh g}_\text{S}^{-1}$ and 970 $\text{mAh g}_\text{S}^{-1}$. At a current density of 0.2 C and 2 C, the discharge capacity is 790 $\text{mAh g}_\text{S}^{-1}$ and 200 $\text{mAh g}_\text{S}^{-1}$, which corresponds to 82 % and 20 % of the initial capacity, respectively. After the stepwise C-rate test up to 2 C, the discharge capacity increases back to about 880 $\text{mAh g}_\text{S}^{-1}$ at 0.01 C, corresponding to a retention rate of 91%. The decrease in discharge capacity with increasing C-rate is visualized better in **Figure 49b**. At a high C-rate (high current density), the cathode reaction and the ionic transport in the electrolyte are the limiting processes leading to a significant decrease in capacity. However, 200 $\text{mAh g}_\text{S}^{-1}$ at 2 C is one of the highest discharge capacities ever reported for an SSB.[104, 239, 240]

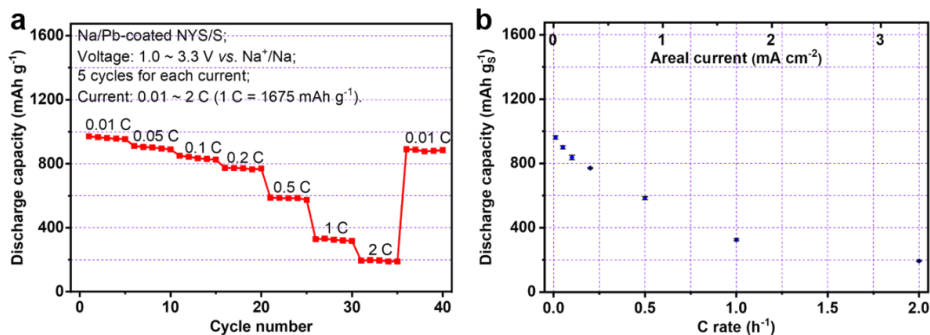


Figure 49 (a) C-rate performance measurement between 0.01 C and 2 C. (b) Change of specific capacity at different C-rates and areal-current densities.

Table 18 The current setting at different C-rates for the electrochemical tests of the full cell.

S loading ($\varnothing = 1.2$ cm, $A = 1.13$ cm ²)			Applied current and C-rate		
Absolute mass after drying (mg)	S in the composite cathode (wt%)	Areal loading (mg cm ⁻²)	Absolute current (mA)	C-rate (h ⁻¹)	Areal current (mA cm ⁻²)
1.13 (3.53 for composite cathode)	32	1.0	0.019	0.01	0.017
			0.095	0.05	0.084
			0.19	0.1	0.17
			0.38	0.2	0.34
			0.95	0.5	0.84
			1.89	1	1.67
			3.8	2	3.35

The cycling performance with the corresponding Coulombic efficiency of the Na/NYS/S full cell is shown in **Figure 50**. The initial discharge capacity reaches up to 970 mAh g_S⁻¹ at a current density of 0.01 C. The initially chosen higher charging voltage of 3.5 V may induce the decomposition of PEO in the S composite cathode.[241] Therefore, for the long-term test, the cut-off voltage was set to 3.3 V vs. Na⁺/Na to maintain a stable potential window for the composite cathode. In 150 cycles, the specific discharge capacity of the full cell decreases from 970 mAh g_S⁻¹ to 600 mAh g_S⁻¹ (0.25% degradation per cycle based on the initial

discharge capacity), showing good cycling stability due to the capability of the NYS scaffold to effectively prevent the dissolution and shuttling effect of S. The Coulombic efficiency is close to 100%, indicating no significant side reactions in the discharge and charge processes. Nevertheless, a thorough further characterization of the complex composite cathode layer needs to be carried out to identify and mitigate the dominating degradation mechanism.[242]

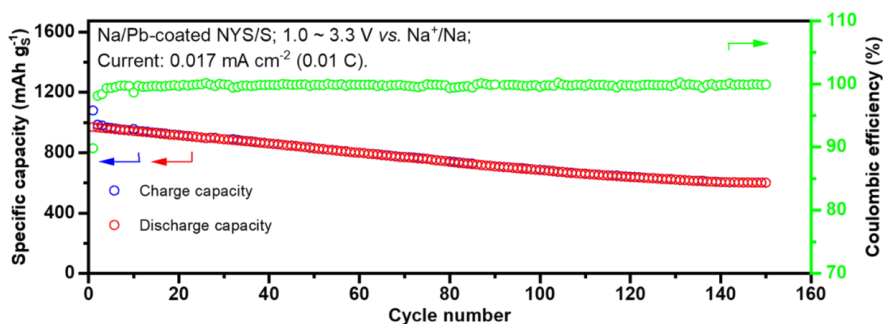


Figure 50 Galvanostatic charge and discharge cycling performance and Coulombic efficiency at a current density of 0.01 C.

The photograph of the Na/NYS/S pouch cell (**Figure 51**) demonstrates its functionality. The capacity of the cell is about 4 mAh and the open circuit voltage is ~ 2.6 V. The light-emitting diode was powered by the pouch cell, which shows the viability of the full cell operating at RT and without external pressure.



Figure 51 Photograph of the pressure-free Na/NYS/S pouch cell and the powered light-emitting diode.

5.3.4. Comparison of electrical performance with the reported data

During recent years, a lot of work on SSBs has been conducted based on pellet-type electrolytes.^[16a] However, full cells using pellets as separators can only demonstrate the generic chemistry or specific electrode modifications under consideration, but are far from realistic cell designs and have no perspective with regard to scalable fabrication, adequate specific energy or cost estimates.[79, 243] In the pellet-based SSB cells compared in **Figure 52a**, the systems Na/Na_{3.5}Zr_{1.9}Al_{0.1}Si_{2.4}P_{0.6}O₁₂/S-C,[227] Na/Na₃PS_{3.85}O_{0.15} + Na₃PS_{3.4}O_{0.6}/S-C-Na₃PS_{3.85}O_{0.15},[226] Na-Sn-C/Na₃PS₄/Na₃PS₄-Na₂S-C[239, 240] and Na/Na_{3.4}Zr₂Si_{2.4}P_{0.6}O₁₂/Na₃V₂P₃O₁₂[140] contain a very thick solid electrolyte that is far thicker than both electrodes, especially the cathode. In addition, the areal loading of the AM in the cathode is not high enough. For comparison, the thickness of the inactive SSE is significantly reduced in full cells using tapes. It is impressive that the reported porous Li₇La₃Zr₂O₁₂ (LLZO) tape is able to incorporate a loading of up to 5.3 mg cm⁻² of cathode material.[244] However, in this case, an ionic liquid-based electrolyte was added to the thick cathode to enhance the ionic conductivity and reduce the interfacial impedance of the cathode. In the porous layer of the NYS scaffold, an areal loading of 1 mg cm⁻² was realized, which is close to the values in the pellet-based full cells.[227, 236] The Ragone plot (**Figure 52b**) provides a more illustrative comparison of pellet-based and tape-based SSBs as well as batteries with liquid electrolytes. The detailed data are given in **Table 19**. In pellet-based SSBs using S[226, 227, 236] and Na₃V₂P₃O₁₂[140] as the cathode, the specific power and specific energy are much worse than the tape-based batteries and liquid electrolyte batteries.[245] The reason for this is related to the inactive electrolyte, which diminishes the energy density and increases the impedance of the cell. In addition, the thick anodes[140, 227] also deteriorate the energy density, because only a small fraction of the thick layer contributes to the cell performance. The established Na/S batteries operating at high temperatures with molten Na metal and S cannot compete with the tape-based Na/NYS/S cells because of the adoption of the thick β"-Al₂O₃ separator and low utilization rate of the electrodes.[246] It is worth mentioning that the specific energy and specific power of the Na/NYS/S all-solid-state cell are close to or even better than those of the liquid Na/S cell system in the low-current region. In the high current region, its performance is inferior to that of the liquid cell due to insufficient ionic and electronic conductivity and large interfacial impedance. Overall, tape-based all-solid-state Na/NYS/S batteries are anticipated to reach or even outperform conventional liquid batteries and they show potential for scalable preparation. Further improvements can be anticipated by increasing the electronic conductivity in the cathode and by rationalizing the degradation behavior.

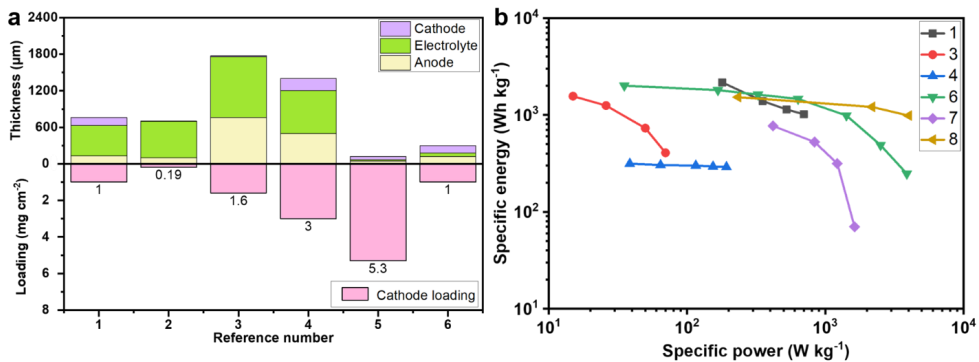


Figure 52 Comparison of different SSB cell architectures.

(a) Layer thicknesses of SSBs and their areal-specific loading of AMs in the cathode. Here mainly sulfur-containing cells were considered. (b) Ragone plot of representative battery cells. See also **Table 19**.

1. $\text{Na}/\text{Na}_{3.5}\text{Zr}_{1.9}\text{Al}_{0.1}\text{Si}_{2.4}\text{P}_{0.6}\text{O}_{12}$ (dropped liquid electrolyte)/S-C, pellet; [236]

2. $\text{Na}/\text{Na}_3\text{PS}_{3.85}\text{O}_{0.15} + \text{Na}_3\text{PS}_{3.4}\text{O}_{0.6}$ bi-layer/S-C- $\text{Na}_3\text{PS}_{3.85}\text{O}_{0.15}$, pellet; [226]

3. $\text{Na-Sn-C}/\text{Na}_3\text{PS}_4/\text{Na}_3\text{PS}_4\text{-Na}_2\text{S-C}$, pellet; [227]

4. $\text{Na}/\text{Na}_{3.4}\text{Zr}_2\text{Si}_{2.4}\text{P}_{0.6}\text{O}_{12}/\text{Na}_3\text{V}_2\text{P}_3\text{O}_{12}$, pellet; [140]

5. $\text{Li}/\text{Li-Li-La}_3\text{Zr}_2\text{O}_{12}/\text{S}$, tape; [244]

6. $\text{Na}/\text{NYS}/\text{S}$ composite, tape (This work);

7. Molten $\text{Na}/\beta\text{-Al}_2\text{O}_3/\text{S}$, pellet; [246]

8. $\text{Na}/1\text{ M NaClO}_4$ in PC-EC/S-C, liquid electrolyte. [245]

Table 19 Comparison of cell specifications of Na-based and Li-based batteries, mostly with sulfur as cathode active material.

No.	Formats of cell and electrolyte	Thickness (μm)			Areal loading of the cathode (mg cm^{-2})	Ref.
		Anode	Electrolyte	Cathode		
1	Na/ $\text{Na}_{3.5}\text{Zr}_{1.9}\text{Al}_{0.1}\text{Si}_{2.4}\text{P}_{0.6}\text{O}_{12}$ + 1 M NaPF_6 in (triethylene glycol, methoxymethane, and 5% fluoroethylene carbonate)/S-carbon nanotube, pellet	130	500	130	1.0	[236]
2	Na/ $\text{Na}_3\text{PS}_{3.85}\text{O}_{0.15}$ + $\text{Na}_3\text{PS}_{3.4}\text{O}_{0.6}$ bi-layer/S-C- $\text{Na}_3\text{PS}_{3.85}\text{O}_{0.15}$, pellet, polyetherether-ketone (PEEK) test cell die	100	600	3.4	0.19	[226]
3	Na-Sn-C/ Na_3PS_4 / Na_3PS_4 - Na_2S -C, pellet, PTFE tank cell die	760	1000	15	1.6	[227]
4	Na/ $\text{Na}_{3.4}\text{Zr}_2\text{Si}_{2.4}\text{P}_{0.6}\text{O}_{12}$ / $\text{Na}_3\text{V}_2\text{P}_3\text{O}_{12}$, pellet, Swagelok cell	500	700	200	3.0	[140]
5	Li/ $\text{Li}_7\text{La}_3\text{Zr}_2\text{O}_{12}$ /S, tape, pouch cell	50	20	50	5.3	[244]
6	Na/NYS/S composite, tape, pouch cell	120	60	120	1.0	This work
7	Molten Na/Na- β'' - Al_2O_3 /S	-	500	-		[246]
8	Na/1 M NaClO_4 in propylene carbonate-ethylene carbonate (V:V = 1:1)/S-carbon nanotube-microporous carbon	-	-	-	(S) 0.4	[245]

It is worth noting that the comparisons made above are related to the number of AMs in the various cell configurations. When the capacity is calculated at the cell level with the experimental data collected here, the obtained gravimetric and volumetric energy density results in values of 45.57 Wh kg⁻¹ and 49.79 Wh L⁻¹, respectively. These values indicate that further optimizations are necessary to compete with liquid-based batteries. Using calculations based on theoretical capacities, the above values increase to 277 Wh kg⁻¹ and 555 Wh L⁻¹, respectively, indicating the high potential of the presented SSSB.

Calculation of the energy density based on the full cell level:

(1) Size data of the cell: diameter: 12 mm (area: 1.131 cm²); thickness: 430 μm (90 μm for the dense layer in the middle and 170 μm for the porous layers on both sides); volume: 0.0486 cm³.

(2) Mass data of the cell: m (Pb coated NYS scaffold): 47.6 mg; m (composite cathode): 3.5 mg (32 wt% S; 1.0 mg cm⁻²); m (Na metal): 2.0 mg, m (total): 53.1 mg.

(3) Electrochemical data of the cell: absolute capacity (1st cycle): 1.1 mAh; mean discharge voltage U : 2.2 V vs. Na⁺/Na.

Calculation:

$$\text{Specific energy (based on the cell mass)} = \frac{U \times \text{capacity}}{m_{\text{total}}} = 45.57 \text{ Wh kg}^{-1} \quad (\text{Equation 33})$$

where U is the mean discharge voltage (V), absolute capacity (Ah) and m mass (kg).

$$\text{Energy density (based on the cell volume)} = \frac{U \times \text{capacity}}{\text{Volume}} = 49.79 \text{ Wh L}^{-1} \quad (\text{Equation 34})$$

Using the theoretical capacities of Na and S, it results in a specific energy of 277 Wh kg⁻¹ and an energy density of 555 Wh L⁻¹.

5.4. Chapter conclusion

In summary, an advanced porous/dense/porous NYS scaffold structure was designed and fabricated by tape casting. The excellent electrochemical performance was demonstrated in Na/NYS/Na symmetric cells and Na/NYS/S full cells. The Na/NYS/Na symmetric cells with a Pb-coated NYS scaffold exhibited an interfacial impedance as low as 25 Ω cm² and a CCD of up to 3.0 mA cm⁻² against Na metal. The initial discharge capacity in the pressureless Na/NYS/S cells reached up to 970 mAh g^s⁻¹ and achieved excellent capacity retention of 600 mAh g^s⁻¹ after 150 cycles. The superior performance is attributed to the as-fabricated porous/dense/porous NYS scaffold with high Na⁺ ionic conductivity of 1 mS cm⁻¹ at RT, an

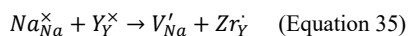
activation energy as low as 0.29 eV and a stable electrochemical window up to 8 V (vs. Na^+/Na). Moreover, this particular structural design addresses the issue of vulnerable electrode/electrolyte interfaces that frequently cause challenges in SSBs with sintered composite electrodes. The porous layers provide a host for the AMs and can mitigate the volume changes during charge/discharge processes, thus improving cycling stability. Compared to SSBs like $\text{Na}/\text{NaSICON}/\text{Na}_3\text{V}_2\text{P}_3\text{O}_{12}$, [140] the infiltration with the polymer/S mixture does not require additional heat treatment to form the AM and provides good contact during cycling. The NYS scaffold, together with the used cathode formulation, allows operation at RT without external pressure. This work presents a novel paradigm to realize affordable and reliable ASS-SMBs from the perspective of structural manufacturing of ceramic electrolytes.

VI. Enhanced Room-Temperature Na⁺ Ionic Conductivity in Na_{4.92}Y_{0.92}Zr_{0.08}Si₄O₁₂[§]

6.1. Chapter introduction

In **Chapters IV and V**, dense and porous/dense/porous NYS tapes have been successfully fabricated and investigated in detail for conductivity, electrochemical stability window, CCD and cycling stability in symmetric cells. Moreover, solid-state Na/S cells were successfully fabricated using the porous/dense/porous scaffold capable of operating at RT. However, for SSEs, the pursuit of higher ionic conductivity at RT never stops. The ionic conductivity of specific compositions can be further modified by substituting heterovalent elements to regulate the concentration of Na⁺ ions and affecting the size of the bottleneck of ionic transport.[26]

In this Chapter, the silicate electrolyte with the composition of Na_{4.92}Y_{0.92}Zr_{0.08}Si₄O₁₂ (NYZS) was synthesized by a facile solid-state reaction method, in which the strategy of defect chemistry by the aliovalent substitution of Y³⁺ with Zr⁴⁺ introduced more Na⁺ ion vacancies and regulated the concentration of defects (Kröger-Vink notation in Equation 35):



where the notation of \times , $'$ and $'$ represent the neutrally, positively and negatively net charge, respectively, and V denotes vacancies. It enables bulk conductivity at RT $\sigma_{\text{bulk-RT}}$ and total conductivity at RT $\sigma_{\text{total-RT}}$ up to 6.5 and 3.3 mS cm⁻¹, respectively. To the best of our knowledge, this is the highest conductivity obtained with NYS-type electrolytes. NYZS exhibits wide electrochemical stability of over 10 V vs. Na⁺/Na, which substantially broadens the selection of cathodes for SSSBs. The excellent cycling performance in symmetric Na/NYZS/Na cells is ascribed to good interfacial compatibility owing to a favorable sodiophilic behavior and great dendrite tolerance with a high CCD. The crystal structure of NYZS and the migration pathways of Na⁺ ions within the crystallographic framework are elucidated by a combination of synchrotron XRD and magic-angle spinning nuclear magnetic resonance (MAS NMR) techniques together with theoretical simulations, which reveal a synergistic effect of the increased number of vacancies and improved chemical surroundings with Zr⁴⁺ substitution. This work reports a novel composition of silicate-based Na⁺ ionic conductors, which will further pave the way for promising SSSBs operating at RT.

[§] Content of this section has been published in *eScience* (DOI: 10.1016/j.esci.2023.100175).

6.2. Experimental

6.2.1. Materials preparation

NYS and $\text{Na}_{5-x}\text{Y}_{1-x}\text{Zr}_x\text{Si}_4\text{O}_{12}$ powders (with different Zr substitutions of 0.04, 0.06, 0.08, 0.10, 0.12, 0.14, 0.2, 0.4, 0.6, 0.8, 1.0 mol) were prepared by solid-state reaction. All the starting materials, $\text{Na}_2\text{CO}_3 \cdot \text{H}_2\text{O}$ (Alfa Aesar, 99.5%), Y_2O_3 (MaTeck, 99.999%), SiO_2 (Aldrich) and ZrO_2 (Alfa Aesar, 99+%), were mixed stoichiometrically and put into a polyethylene vial (250 ml) with zirconia balls (200 g milling balls with diameters of 3 and 5 mm) as grinding agent and ethanol (150 ml) as the dispersant. The ball milling time was 48 h. Before mixing the starting materials, Y_2O_3 and ZrO_2 powders were heated at 900 °C for 3 h to remove the moisture. After ball-mixing the powders, the white slurry was put out and dried in an oven at 60 °C for 10 h. Then, the white powders were calcined at 500°C for 5 h in air before pressing to remove gaseous residuals and get dense pellets. In the calcination process, there is no phase formation or crystallization. After calcination, the powders were uniaxially pressed into pellets ($\text{Ø} = 13$ mm) with a pressure of 100 MPa and sintered at 1100 °C for 6 h in air.

6.2.2. Structural characterization

Synchrotron X-ray diffraction experiments were measured with powder sample NYZS in a 0.8 mm diameter glass capillary (WJM) at the beamline of PETRA III beamline P02.1 at the Deutsches Elektronen-Synchrotron (DESY). The wavelength for the measurement was $\lambda = 0.207349$ Å and the integration time for the sample was 300 s. The sample was spun during the measurement to obtain better statistics. The area detector was a Varex XRD 4343CT (150×150 μm^2 pixel size and 2880×2880 pixel area, CsI scintillator directly deposited on amorphous Si photodiodes). Data was integrated using the DAWN Science Software.[247] The data were analyzed with the Rietveld method by using the General Structure Analysis System (GSAS).[248] The crystal structures of the materials were characterized by powder X-ray diffraction (D4, Bruker) with $\text{Cu } K_\alpha$ radiation. Temperature-dependent XRD patterns were measured. The morphology of the pellets was characterized by SEM (S-4800) equipped with energy-dispersive X-ray spectroscopy and high-resolution transmission electron microscopy (HRTEM, 2100F). The surface oxidation and the composition were confirmed by XPS (PHI-5300 ESCA 1610 SAM).

6.2.3. Electrochemical characterization

The electrochemical performances (impedance spectroscopy, galvanostatic cycling profiles, DC polarization and CV) were tested with a Biologic multi-channel electrochemical workstation (VMP 300)

and a combined electrochemical system (Keysight E4991B and Novocontrol Technologies Alpha-A). These electrochemical data were recorded at RT unless otherwise specified. All tested cells were assembled in the Ar-filled glovebox (Glovebox System, Germany) with Swagelok cell models or pouch-type cells. The sandwich-structured cells were assembled for the AC impedance measurements by attaching Na foils or sputtering Au coatings on both sides of the as-prepared pellets. The testing frequency ranges were from 3 GHz or 7 MHz to 1 Hz applying an amplitude of 5 mV. The galvanostatic cycling performance was tested with Na/NYZS/Na symmetric cells at the current density of 1 mA cm⁻² and the deposition capacity of 1 mAh cm⁻² every half cycle. Preparation of the Super P electrode and (Super P + NYZS) composite electrode followed the routine procedure but with different ratios.[6] For both electrodes, PVDF ($M_w = 600,000$, Sigma-Aldrich) with a ratio of 10 wt% was used as the binder. For the composite electrode, the ratios were NYZS (70 wt%) and Super P (20 wt%). The formulation of the liquid electrolyte (LE) was 1.0 M NaPF₆ in propylene carbonate (PC), which was purchased from Suzhou Fosai New Material Co., Ltd. The CV curves were measured at different voltage intervals in the cell configuration of Na/NYZS/Au, Na/NYZS/(NYZS+Super P), Na/LE/Super P and Na/LE/(NYZS+Super P) with different scanning speeds.

6.2.4. NMR measurements

Static ²³Na relaxometry and line shape analysis were performed on a Bruker Avance Neo 200 MHz spectrometer at a magnetic field strength of 4.7 T. The samples were sealed in 10 mm evacuated silica glass tubes. The data were acquired with an inversion-recovery and solid-echo pulse sequence in the temperature range from 260 to 595 K. The recycle delay was set to values between 0.4 and 2 s and was always well above 5 · T_1 . 1 M NaCl was used as a reference for the ²³Na NMR spectra.

²³Na and ²⁹Si MAS spectra were detected on a 500 MHz Bruker Avance spectrometer using a 2.5 mm rotor at a spinning speed of 30 kHz. The ²³Na spectra were referenced with 1 M NaCl and ²⁹Si spectra with tetramethylsilane (TMS). The recycle delays were set to 30 s for the ²³Na and 60 s for the ²⁹Si spectra acquisition.

⁸⁹Y MAS spectra were detected on a Bruker Neo 600 MHz spectrometer (Larmor frequency of 29.42 MHz) using a 7 mm rotor at a spinning speed of 5 kHz. Between 1800 and 2000 scans were acquired for each sample with a relaxation delay of 50 s. The spectra were referenced concerning the signal of TMS (absolute referencing).

²³Na MQMAS NMR experiments were performed on a Bruker Avance III 400 MHz spectrometer using a 2.5 mm rotor at a spinning speed of 25 kHz. Two-dimensional ²³Na MQMAS experiments were performed

using a phase-modulated split- t_1 pulse sequence [249, 250] with rotor synchronization. A total of 512 t_1 increments were acquired in the F1 dimension, expanded after Fourier transformation to 1024 points.

6.2.5. Theoretical calculation and fitting methods

All simulations employed the CASTEP and the plane-wave DFT code with generalized gradient approximation (GGA) and Perdew-Burke-Ernzerhof (PBE) exchange functions. The transit search (TS) method was used with the complete linear synchronous transit/quadratic synchronous transit (LST/QST) method. The plane-wave energy cutoff was 500 eV. The core electrons were treated by an ultrasoft pseudopotential. The k -point grid was automatically generated with the Monkhorst-Pack method. The simulated results were visualized by VESTA. The BVSE calculations are performed using Fullprof Suite software and isosurfaces of mobile Na^+ ions are displayed by the VESTA visualization package. Impedance data were fitted using the Zview software, Scribner Associates Inc.

6.3. Results and discussion

6.3.1. Synthesis and structural analysis of NYZS

As shown in **Figure 53**, the facile solid-state reaction method was employed to synthesize the series $\text{Na}_{5-x}\text{Y}_{1-x}\text{Zr}_x\text{Si}_4\text{O}_{12}$ ($0 \leq x \leq 1$), which provides the feasibility of large-scale preparation of inexpensive silicate electrolytes.

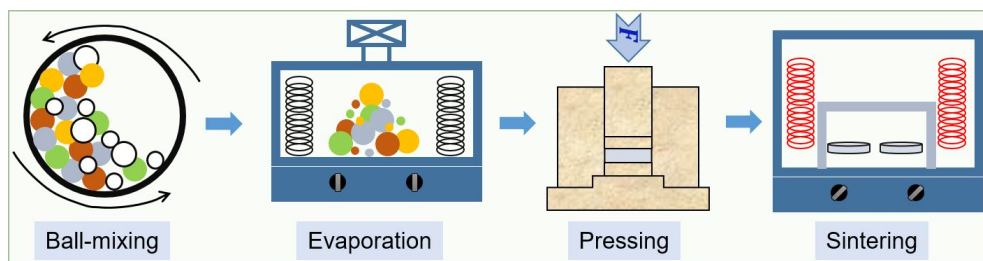


Figure 53 Schematic of the solid-state synthesis process, which consists of ball-mixing, solvent evaporation, powder pressing and sintering.

The corresponding XRD patterns, analysis of secondary phases, and $\sigma_{\text{total-RT}}$ of this series in dependence on Zr substitution are shown in **Figure 54**, **Figure 55** and **Table 20**, in which the highest $\sigma_{\text{total-RT}}$ (3.3 mS cm^{-1}) was achieved with $x = 0.08$, i.e., $\text{Na}_{4.92}\text{Y}_{0.92}\text{Zr}_{0.08}\text{Si}_4\text{O}_{12}$ (NYZS).

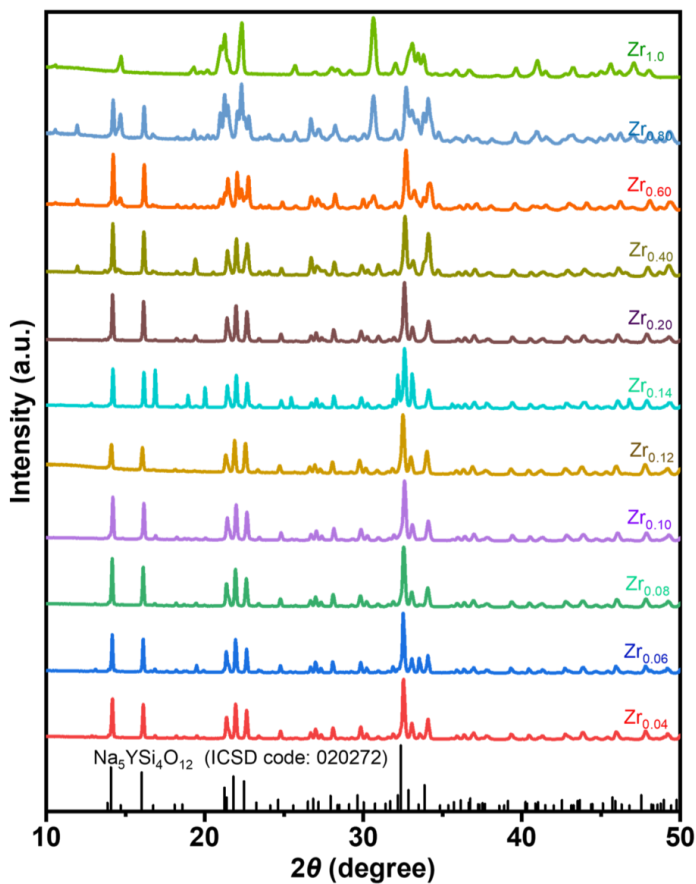


Figure 54 XRD patterns ($\lambda = 1.5406 \text{ \AA}$) of the synthesized $\text{Na}_{5-x}\text{Y}_{1-x}\text{Zr}_x\text{Si}_4\text{O}_{12}$ ($0 \leq x \leq 1$) with different Zr substitutions ($x = 0.04, 0.06, 0.08, 0.10, 0.12, 0.14, 0.20, 0.40, 0.60, 0.80, 1.0$).

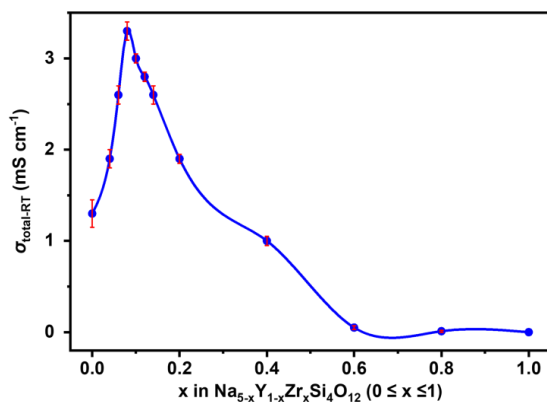


Figure 55 Total conductivities at RT in the series $\text{Na}_{5-x}\text{Y}_{1-x}\text{Zr}_x\text{Si}_4\text{O}_{12}$ ($0 \leq x \leq 1$).

Table 20 Total conductivities at RT ($\sigma_{\text{total-RT}}$) and the analysis of major secondary phases in the series $\text{Na}_{5-x}\text{Y}_{1-x}\text{Zr}_x\text{Si}_4\text{O}_{12}$ ($0 \leq x \leq 1$), corresponding to **Figure 54**.

x in $\text{Na}_{5-x}\text{Y}_{1-x}\text{Zr}_x\text{Si}_4\text{O}_{12}$	$\sigma_{\text{total-RT}}/\text{mS cm}^{-1}$	Major secondary phases*
0	1.3	$\text{Na}_3\text{YSi}_2\text{O}_7$
0.04	1.9	
0.06	2.6	
0.08	3.3	
0.10	3.0	
0.12	2.8	
0.14	2.6	
0.20	1.9	$\text{Na}_4\text{Zr}_2\text{Si}_3\text{O}_{12}$
0.40	1.0	$\text{Na}_2\text{ZrSi}_2\text{O}_7$
0.60	0.05	
0.80	0.01	
1.0	~ 0	

* The main phase for the Zr-substituted compositions is identical to the $\text{Na}_5\text{YSi}_4\text{O}_{12}$ (NYS) without Zr substitution. As the amount of Zr substitution increases, different secondary phases are formed and increased, decreasing the conductivity due to their insulating property of them.

The Rietveld-refined XRD pattern of NYZS, shown in **Figure 56a**, confirmed the rhombohedral structure with $R\bar{3}c$ symmetry (**Figure 56b**) as known from NYS. The refined lattice parameters are $a = 21.99 \text{ \AA}$, $c = 12.61 \text{ \AA}$, and $V = 5286.1 \text{ \AA}^3$. The staggered $[\text{SiO}_4]$ tetrahedra form the 12-membered silicate rings $[\text{Si}_{12}\text{O}_{36}]$ and are then stacked as columns by sharing O atoms which, in turn, are linked to each other by $[\text{YO}_6]$ or $[\text{ZrO}_6]$ octahedra. The combination of these rings, columns and octahedra results in a framework structure with two three-dimensionally (3D) linked channels. One of the channels is surrounded only by $[\text{SiO}_4]$ tetrahedra and is filled by Na^+ ions on three different sites (denoted as Na1, Na2, and Na3), which are stacked to a prismatic column parallel to the c -axis. Refinement of occupancy parameters of these three Na^+ ions tended to full occupancies, which indicated the immobility of these Na^+ ions in the rigid prismatic columns. Another channel is surrounded by $[\text{SiO}_4]$ tetrahedra and $[(\text{Y}, \text{Zr})\text{O}_6]$ octahedra and partially occupied by Na^+ ions in two sites (denoted as Na5, Na6) forming a zigzag chain parallel to the c axis. Because of their very short interatomic distances of $1 \sim 2 \text{ \AA}$ between two Na^+ ions, a restriction in the refinement was employed to obtain equivalent isotropic atomic displacement parameters (ADPs). Their occupancies were refined freely with a restriction of a fixed sum of ions to keep the charges balanced. Zigzag chains are interconnected through Na^+ ions in Na4 sites linking the Na^+ ions on Na5 and Na6 in different channels and leading to a 3D substructure of the Na^+ ions. The Na4 sites are located near the screw axes similar and close to the Y^{3+} ions. The Na4 sites are fully occupied and reveal large apparent ADPs, indicating their high mobility. In contrast, the ADPs of Na1 sites are much smaller than those of Na4 sites. The atomic parameters of the refined structure of NYZS and the selected interatomic distances are shown in **Tables 21** and **Table 22**, respectively.

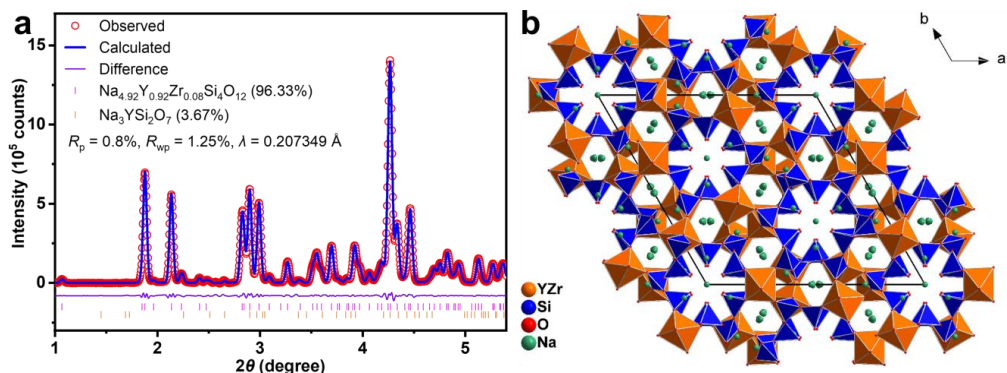


Figure 56 Synchrotron XRD refinement and projection of crystal structure of NYZS.

(a) Rietveld refinement against the powder synchrotron XRD pattern, revealing the phase purity of NYZS up to 96.33% and the secondary phase $\text{Na}_3\text{YSi}_2\text{O}_7$ of 3.67%. (b) The projection of the unit cell after Rietveld refinement viewed along the c axis: SiO_4 tetrahedra in blue; (Y, Zr) O_6 octahedra in brown; O atoms in red and Na atoms in green.

Table 21 Parameters of refined structures of NYS and NYZS.

Composition	$a/\text{\AA}$	$c/\text{\AA}$	$V/\text{\AA}^3$	The mass ratio of secondary phases
NYS	22.02	12.61	5292.6	< 5 wt% $\text{Na}_3\text{YSi}_2\text{O}_7$
NYZS	21.99	12.61	5286.1	< 5 wt% $\text{Na}_3\text{YSi}_2\text{O}_7$

Table 22 Site occupancies, atomic coordinates isotropic displacement parameters of NYZS.

Atom	Wyck.	Site	Occ.	$x (a)$	$y (b)$	$z (c)$	$U/\text{\AA}^2$
Y1	18e	.2	0.92	0	0.75210	0.75000	0.016
Zr1	18e	.2	0.08	0	0.75200	0.75000	0.016
Si1	36f	1	-	0.90130	0.54830	0.36030	0.033
Si2	36f	1	-	0.57270	0.14900	0.70840	0.001
O1	36f	1	-	0.90380	0.59820	0.26420	0
O2	36f	1	-	0.07470	0.20850	0.01020	0.034
O3	36f	1	-	0.23640	0.61950	0.28870	0.018
O4	36f	1	-	0.91310	0.27020	0.24250	0.009
O5	36f	1	-	0.88850	0.46530	0.09340	0.005
O6	36f	1	-	0.87520	0.36610	0.21730	0.001
Na1	36f	1	-	0.07020	0.13770	0.86190	0.021
Na2	6b	-3.	-	0	0	0	0
Na3	6a	32	-	0	0	0.25000	0.035
Na4	18e	.2	-	0.27540	0	0.75000	0.065
Na5	36f	1	0.28	0.33810	0.19480	0.25240	0.004
Na6	36f	1	0.35	0.32500	0.15710	0.12170	0.022

The sintered NYZS pellet is closely packed by micron-sized grains in a disordered manner. The grain size distribution is relatively narrow with 1 to 5 μm (**Figure 57a**). The high-resolution transmission electron microscopic (HRTEM) image (**Figure 57b**) of NYZS further verifies the polycrystallinity with different orientations of lattice fringes within a single grain. The cross-sectional view and energy dispersive X-ray (EDX) mapping analysis (**Figure 58**) exhibit pore-free morphology, dense microstructure ($> 95\%$ relative density; 2.85 g cm^{-3} of crystallographic density) and uniform elemental distribution of NYZS, which endow its high $\sigma_{\text{total-RT}}$.

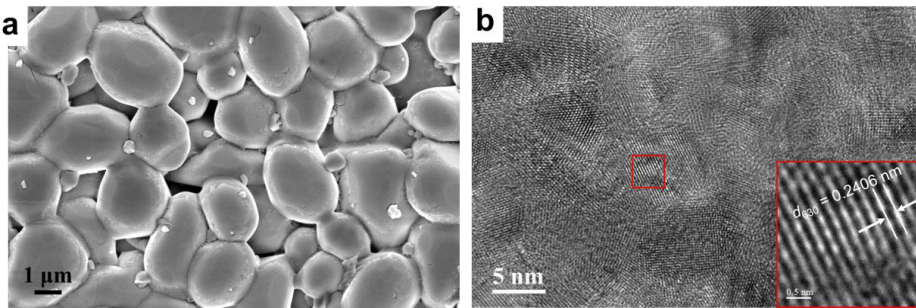


Figure 57 SEM and HRTEM images of NYZS crystal.

(a) SEM image of the surface morphology of a sintered NYZS pellet with dense packing of the grains. (b) HRTEM image of NYZS showing the polycrystallinity of the grains. The inset is the magnification of the selected area, showing the clear lattice fringe of crystal facets [630].

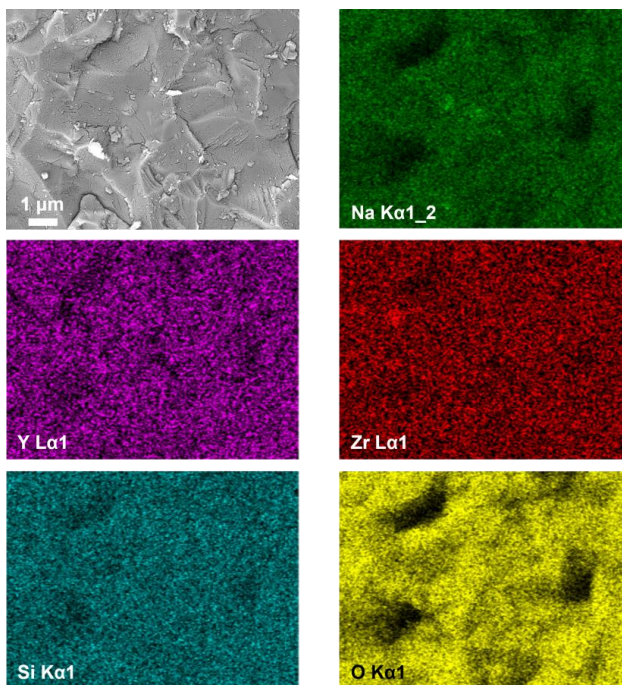


Figure 58 Cross-sectional view and EDX mapping of NYZS.

XPS is used to prove and detect the impact of the Zr incorporation in NYZS. The intensity of Zr in the survey spectra of NYZS (**Figure 59**) is not noticeable due to the low content. The binding energy of Y 3*d* (**Figure 60a**), Si 2*p* (**Figure 60b**) and O 1*s* (**Figure 60c**) slightly shifted to higher energy (**Table 23**) in NYZS compared with NYS, which is explained by the enhanced bond strength due to the shortened bond length (**Table 24**). Another indication is the slight shrinkage of the *a* and *c* axis of the unit cell for NYZS (**Table 21**) resulting from the smaller ionic radius of Zr⁴⁺, which generally increases the binding energies.

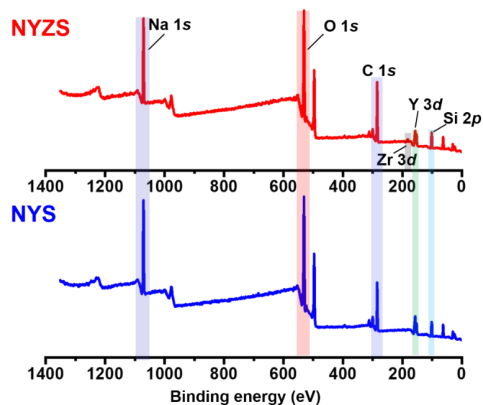


Figure 59 XPS survey spectra of NYS and NYZS.

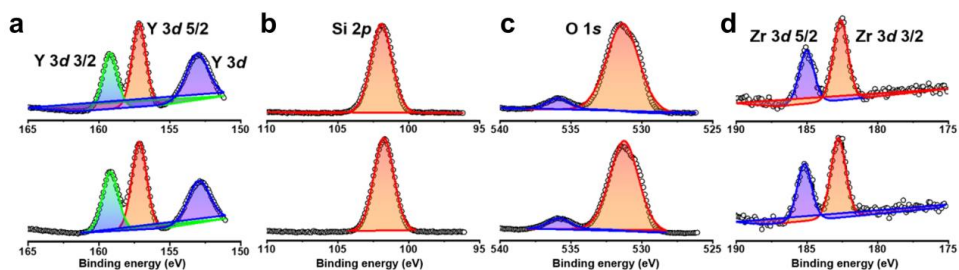


Figure 60 The fitted XPS of (f) Y 3d, (g) Si 2p and (h) O 1s.

The bottom and top spectra belong to NYS and NYZS, respectively. (i) The fitted XPS spectra of Zr 3d directly after sample preparation (bottom) and after three months (top) in ambient atmosphere.

Table 23 The comparison of binding energy between NYS and NYZS.

Composition	Binding energy/eV								
	Na 1s	Y 3d	Y 3d 5/2	Y 3d 3/2	Si 2p	O 1s	O 1s	Zr 3d 3/2	Zr 3d 5/2
NYS	1071.4	152.8	157.1	159.1	101.7	531.2	535.8	/	/
NYZS	1071.6	153.0	157.2	159.2	101.9	531.4	535.9	182.6	185.0

Table 24 Comparison of specific bond lengths between NYS and NYZS.

Composition	Na-O/Å	Si-O/Å	Y-O/Å
NYS	2.53	1.65	2.25
NYZS	2.41	1.64	2.24

Good stability in ambient air is crucial for synthesis, storage and subsequent processing. The XRD patterns (**Figure 61**) and Zr 3d XPS spectra (**Figure 60d**) of the fresh and long-term exposed sample in air for three months were individually analyzed to detect any evolution of NYZS characteristics. Still, both methods show negligible changes after the storage period, which confirms the good chemical stability thanks to the intrinsic stability of silicates. More importantly, the $\sigma_{\text{total-RT}}$ of NYZS did not show a significant degradation from 3.3 to 3.2 mS cm⁻¹ after slightly polishing both sides of the pellet (Nyquist plots are shown in **Figure 62**). The temperature-dependent XRD patterns show no phase transition between RT and 1000 °C (**Figure 63a**). From the thermal expansion of the crystal lattice, the mean coefficient of thermal expansion (CTE) was determined ($\alpha_V = 7.0 \times 10^{-6} \text{ K}^{-1}$) based on the unit cell volume of NYZS using the length changes along the *a* and *c* axis (**Figure 63b**).

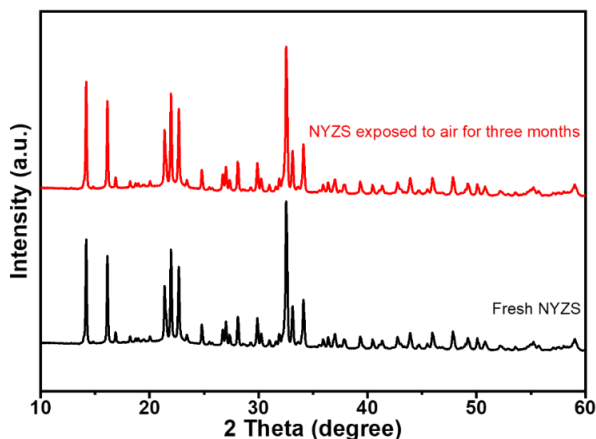


Figure 61 Comparison of XRD patterns ($\lambda = 1.5406 \text{ \AA}$) of the fresh sample and exposed sample after three months in ambient air.

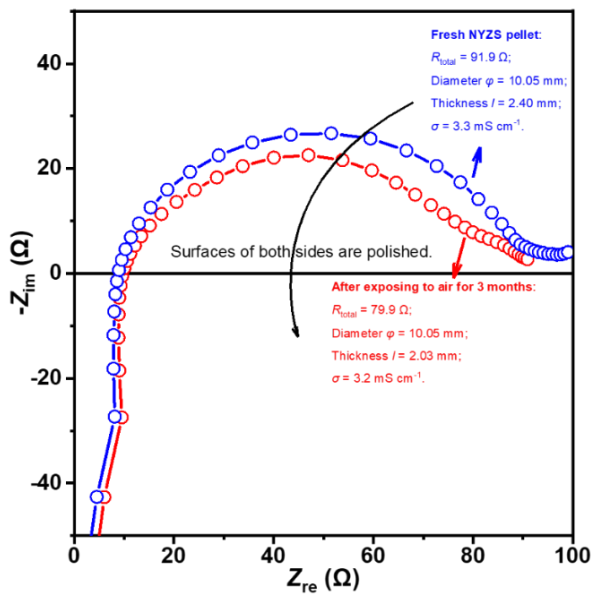


Figure 62 Nyquist plots of the fresh sample and exposed sample after three months in ambient air.

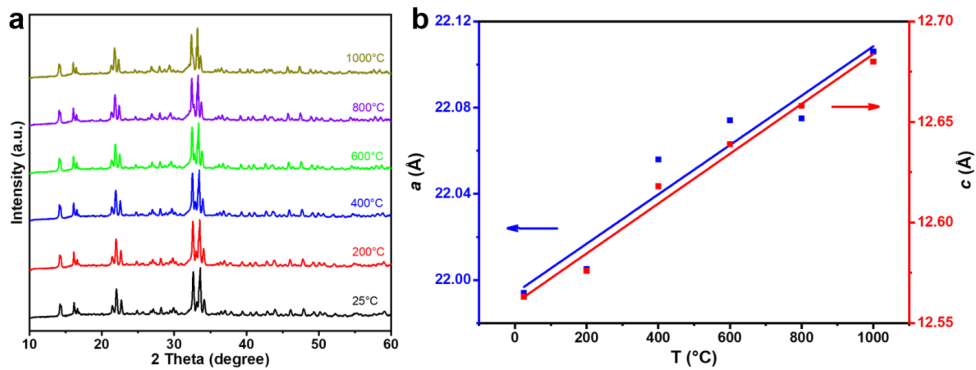


Figure 63 (a) The temperature-dependent XRD patterns ($\lambda = 1.5406 \text{ \AA}$) and (b) values of a and c in a unit cell of NYZS between 25 and 1000 °C.

The calculation of the coefficient of thermal expansion (CTE) is based on Equations 36 and 37:

$$\alpha = \frac{\Delta l}{l_0 \Delta T} \text{ (Equation 36)}$$

$$\alpha_V = \frac{2\alpha_a + \alpha_c}{3} \text{ (Equation 37)}$$

where l_0 and Δl represent the original length and the length change, and ΔT refers to the temperature difference. α , α_V , α_a and α_c are general CTE and CTE based on volume V , a and c axis, respectively, which have a unit of reciprocal temperature (K^{-1}).

6.3.2. Electrical and electrochemical properties of NYZS

The EIS (**Figure 64**) with a wide frequency range from 3 GHz to 1 Hz at RT was analyzed using gold as blocking electrodes to distinguish the resistivity from bulk (i.e., grains) and grain boundaries. The EIS curves exhibit two consecutive semicircles in different frequency regions. The fitted values for each element in the equivalent circuit are listed in **Table 25**. The first semicircle corresponds to the bulk resistance (R_{bulk}) of 46 Ω of the ceramic NYZS pellet, equivalent to the $\sigma_{\text{bulk-RT}}$ of 6.5 mS cm^{-1} . A capacitance of 1.9×10^{-12} F (capacitance of constant phase element, CPE1) and the frequency region of 3 GHz \sim 200 MHz for the first semicircle verify this assumption.[220] The second semicircle at lower frequencies is ascribed to the ionic transport resistance of grain boundaries (R_{gb}) of 45 Ω , in which the CPE2 exhibits the capacitance of 2.1×10^{-8} F, indicating a justified assignment to the ionic migration through the grain boundaries. The nearly vertical line at low frequencies is related to the electrode contact resistance of the Au/SSE interface ($R_{\text{interface}}$), which is also verified from the magnitude of the capacitance values of 1.0×10^{-7} F.[220] The $\sigma_{\text{total-RT}}$ of NYZS is determined by the summation of the resistance from bulk and grain boundary components, which is 3.3 mS cm^{-1} and is comparable to that of β'' -alumina and NASICON. In comparison, the fitted conductivity values of the NYS sample are 2.4 ($\sigma_{\text{bulk-RT}}$) and 1.3 ($\sigma_{\text{total-RT}}$) mS cm^{-1} , which are both inferior to those of NYZS. Oxide-based SSEs usually exhibit high R_{gb} ,[251] but here R_{gb} is similar to R_{bulk} , which is one of the advantages of NYS and NYZS.

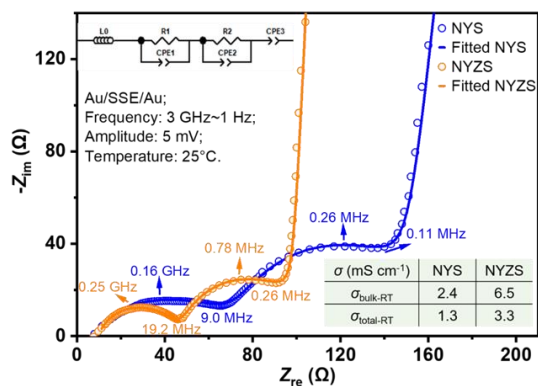


Figure 64 Nyquist plots of NYS and NYZS (inset: equivalent circuit for fitting).

Table 25 Values of the fitted equivalent circuit in the symmetric Au/SSE/Au cells (corresponding to **Figure 64**).

SSE	L0/H	R1/ Ω	CPE1/F	R2/ Ω	CPE2/F	CPE3/F
NYS	1.0×10^{-10}	80	8.6×10^{-12}	70	3.1×10^{-8}	2.3×10^{-7}
NYZS	5.5×10^{-10}	46	1.9×10^{-12}	45	2.1×10^{-8}	1.0×10^{-7}

Temperature-dependent Na^+ ionic conductivities of NYS and NYZS samples were measured between -100 and 100 °C and plotted as Arrhenius curves (**Figure 65**). Determined from the Arrhenius plot, the activation energies of bulk ($E_{a\text{-bulk}}$) and total conductivity ($E_{a\text{-total}}$) of NYZS are 0.26 and 0.30 eV, respectively. The E_a values of NYS are comparable with those of NYZS, which are 0.25 ($E_{a\text{-bulk}}$) and 0.29 eV ($E_{a\text{-total}}$). The details of the calculation and comparison of E_a are exhibited in **Tables 26** and **Table 27**.

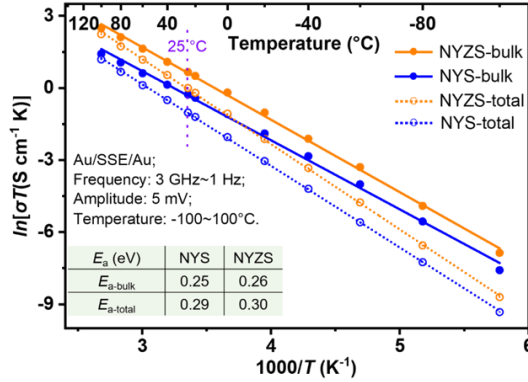


Figure 65 Arrhenius plots of NYS and NYZS in the temperature range of ± 100 °C.

Calculation method of E_a :

The conductivity of a thermally activated transport process in solids is generally depicted by the Arrhenius expression Equation 38:

$$\sigma = \frac{A}{T} e^{-\frac{E_a}{kT}} \quad (\text{Equation 38})$$

and the logarithmic deformation formula:

$$\ln(\sigma T) = \ln A - \frac{E_a}{k} \frac{1}{T} \quad (\text{Equation 39})$$

where σ represents conductivity, A represents exponential prefactor (it is a constant or shows a weak temperature dependence), T means thermodynamic temperature, E_a represents the activation energy for the transport process of thermally activated ions, e represents Euler's number and k represents Boltzmann constant ($k = 8.6 \times 10^{-5} \text{ eV K}^{-1}$). From the logarithmic-type Equation 39, it can be seen that graphing $\ln(\sigma T)$ with the reciprocal of temperature $\frac{1}{T}$ gives a straight line from which the activation energy can be conveniently calculated by the slope of the line. Moreover, when plotting the activation energies of the bulk and total conduction, both show a very good linear relationship with R-values over 99%. All the linear fitting equations are listed in the following **Table 26**.

Table 26 Linear fitting equations of NYS and NYZS (Corresponds to **Figure 65**).

Composition	NYS	NYZS
Fitted equation based on bulk conductivity	$y = -2.876x + 9.326$	$y = -3.014x + 10.734$
Fitted equation based on total conductivity	$y = -3.396x + 10.339$	$y = -3.546x + 11.842$

Table 27 Bulk ($E_{a\text{-bulk}}$) and total ($E_{a\text{-total}}$) activation energy of NYS and NYZS (Corresponding to **Figure 65**).

E_a/eV	NYS	NYZS
$E_{a\text{-bulk}}$	0.25	0.26
$E_{a\text{-total}}$	0.29	0.30

The interfacial compatibility between Na metal and NYZS was evaluated by the magnitude of the $R_{\text{interface}}$ against Na metal and the cyclic voltammetry (CV) test. Benefiting from the excellent ductility of Na metal and chemically stable contacting interface, the intrinsic $R_{\text{interface}}$ is only $4 \Omega \text{ cm}^2$ (**Figure 66a**) in the Na/NYZS/Na symmetric cell, which is lower than for most values of the published Na^+ and Li^+ solid-state conductors.[25] Values of the fitted equivalent circuit parameters of the symmetric Na/NYZS/Na cells are listed in **Table 28**. The CV curve (**Figure 66b**) was also tested with a Na/NYZS/Au cell in the scanning range from -0.5 to 10 V vs. the Na^+/Na electrode. The reduction peak ($-0.5 \sim 0 \text{ V}$) and the oxidation peak ($0 \sim 0.5 \text{ V}$) were induced by the stripping and plating of Na^+ ions at the Na/NYZS interfaces, respectively. A couple of symmetric redox peaks with nearly the same area suggest high reversibility of Na metal and no side reactions between NYZS and Na. The absence of significant oxidation peaks observed in the voltage range from 0.5 to 10 V implies that NYZS has a wide electrochemical window of up to 10 V , which is comparable with other oxide-based SSEs.[252]

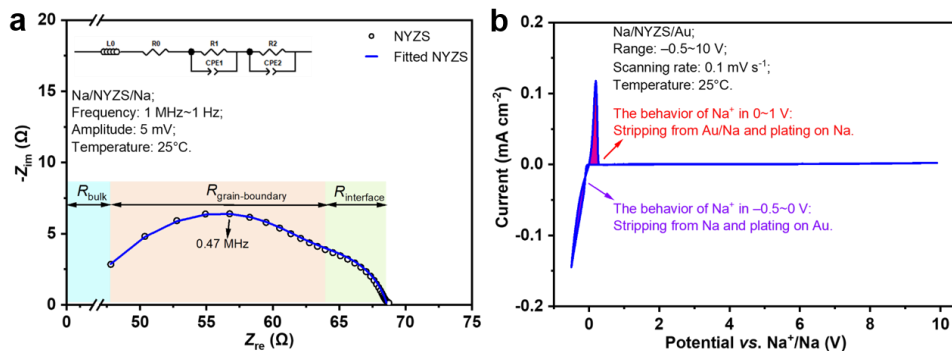


Figure 66 (a) Nyquist plot of NYZS with Na metal as electrodes (inset: equivalent circuit for fitting), revealing a low $R_{\text{interface}}$ between NYZS and Na metal. (b) CV curve of NYZS in the scanning range of $-0.5 \sim 10$ V vs. Na^+/Na with the rate of 0.1 mV s^{-1} .

Table 28 The fitted equivalent circuit in the symmetric Na/NYZS/Na cells (Corresponds to **Figure 66a**).

L0/H	R0/ Ω	R1/ Ω	CPE1/F	R2/ Ω	CPE2/F
1.3×10^{-6}	32	31	3.7×10^{-8}	4	3.8×10^{-6}

To be able to fairly evaluate the electrochemical stability window of NYZS, in addition to the CV measurement under the Na/NYZS/Au cell configuration, another two testing methodologies have been adopted to amplify the potentially invisible electrochemical response.[157, 252, 253] Fine NYZS powder along with conductive carbon Super P was fabricated into electrodes and examined for CV curves and (dis)charge performance in liquid and solid-state cells, respectively. Despite the sufficient contact area between NYZS and Super P, NYZS exhibited neither decomposition nor side-reaction evidence during the measured intervals. Detailed results and analyses are presented in **Figure 67**.

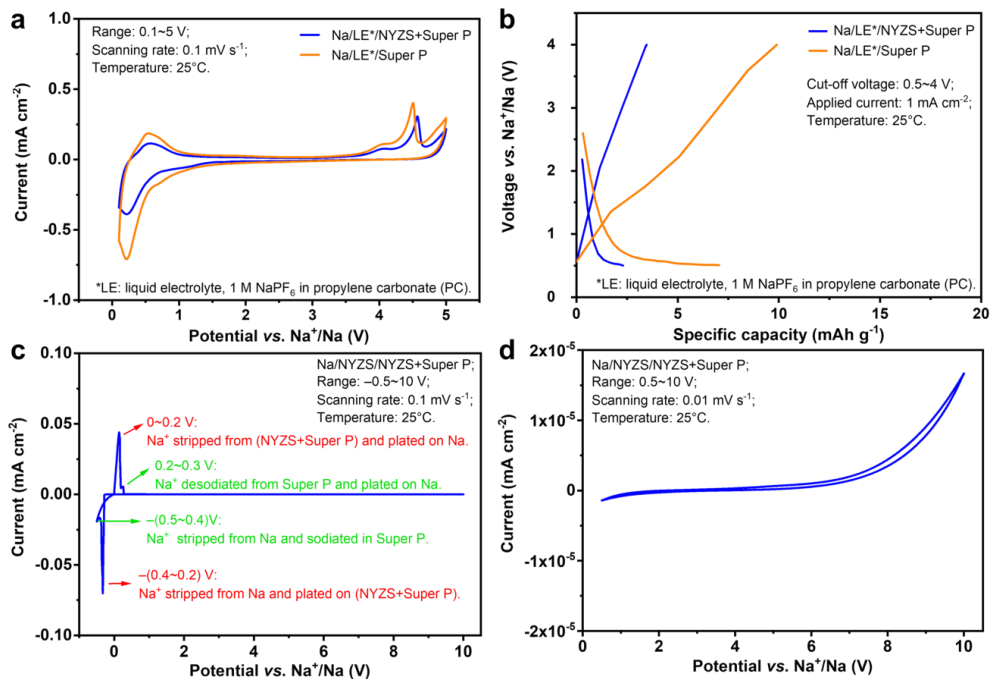


Figure 67 Electrochemical stability measurements of NYZS in the cells with (a-b) liquid electrolyte (LE) and (c-d) solid-state electrolyte NYZS.

(a) CV curves in the cells of Na/LE/(NYZS+Super P) composite cathode and Na/LE/Super P. (b) Galvanostatic (dis)charge profiles at the current density of 1 mA cm⁻² (~ 2 mg cm⁻² of areal loading, i.e., ~ 0.5 mA mg⁻¹). (c) CV curve in the cells of Na/NYZS/(NYZS+Super P) composite cathode at the scanning rate of 0.1 mV s⁻¹ within the range of -0.5 ~ 10 V vs. Na⁺/Na. (d) CV curve in the cells of Na/NYZS/(NYZS+Super P) composite cathode at the slower scanning rate of 0.01 mV s⁻¹ within the range of 0.5 ~ 10 V vs. Na⁺/Na.

The CV measurement of using a reversible electrode/SSE/inert blocking electrode configuration (here Na/NYZS/Au) to bolster electrochemical stability has been criticized for the inadequate contact area between the electrodes and the electrolyte resulting in a negligible current response as compared to the reversible stripping and plating of carrier ions at the electrodes on both sides. Therefore, to eliminate this technical deficiency, two more convincing experiments were conducted to validate the electrochemical stability of NYZS. NYZS powder along with conductive carbon Super P was fabricated into electrodes and

used for the examination of CV curves and (dis)charge performance in [i] liquid and [ii] solid-state cells, respectively.

[i] Following the protocol of the published references for the studies of electrochemical stability of sulfide electrolytes[157, 253], the inert Au electrode was replaced with a composite electrode of NYZS fine powder (70 wt%) and conductive carbon Super P (20 wt%) in the CV test. A conventional Na⁺ ion liquid electrolyte (LE), 1 M NaPF₆ in propylene carbonate (PC), is used to fabricate the cells toward achieving sufficient contact between the liquid electrolyte and the electrode NYZS. Cells only using Super P (90 wt%) as the counter electrode were also assembled and tested to obtain an electrochemical stability window of the liquid electrolyte. As shown in **Figure 67a**, unlike the behaviors in Na₃PS₄ and Na₃PSe₄[157], NYZS did not exhibit an observed electrochemical reaction response except for the broad peaks, which can be ascribed to the decomposition of the liquid electrolyte over 4 V (vs. Na⁺/Na) and the formation of solid electrolyte interphase (SEI) below 1 V (vs. Na⁺/Na)[254]. The peak current density of the control cell using Super P is higher than that of the (NYZS + Super P) composite electrode, and both (~ 0.5 mA cm⁻², **Figure 67a**) are significantly larger than the value of Na/NYZS/Au (~ 0.1 mA cm⁻², **Figure 66b** in the main text), suggesting that the use of liquid electrolyte improved the contact area and that the broad peaks come from the decomposition of the liquid electrolyte, rather than from the reaction of NYZS. Therefore, the wider applied voltage range is restricted by the narrow electrochemical window of the liquid electrolyte, which could not justify the arguments presented in this manuscript. Different from the reported sulfide electrolytes[157], NYZS did not show a visible capacity contribution (< 10 mAh g⁻¹, **Figure 67b**).

[ii] Thus for the subsequent experiment, solid-state Na/NYZS/(NYZS+Super P) cells were fabricated to amplify the current response by increasing the contact area with the fully mixed NYZS and Super P, which has been reported in the studies of Li₁₀GeP₂S₁₂ and Li₇La₃Zr₂O₁₂[252]. As shown in **Figure 67c**, in contrast to the CV curve of the Na/NYZS/Au cell, two pairs of symmetrical redox peaks were observed in Na/NYZS/(NYZS + Super P). The pair of major peaks are attributed to the reversible plating and stripping of Na⁺ ions between two electrodes, which is not unusual with the inert Au electrode. The pair of minor peaks is due to the reversible insertion and desertion of Na⁺ ions within the conducting carbon Super P. Beyond that, there was no other current response observed. In **Figure 67d**, after utilizing a slower scanning rate of 0.01 mV s⁻¹ and avoiding the reversible plating and stripping reactions of Na⁺ ions, there was still no significant side reaction in the voltage range of 0.5 ~ 10 V. The capacity of galvanostatic (dis)charge is 0 in the cell of Na/NYZS/(NYZS + Super P).

These robust proofs emphasize the superiority of NYZS in terms of its ultra-wide electrochemical stability. Matching NYZS with high-potential cathodes to take advantage of its ultra-wide electrochemical window requires further investigation.

The CCD of the NYZS pellet is observed at 2.4 mA cm^{-2} (**Figure 68**), which is ascribed to the dense microstructure, high ionic conductivity and superior interfacial compatibility. When the applied current density reaches 3.1 mA cm^{-2} , the polarization voltage becomes unstable and shows large voltage spikes, indicating that the interface between Na and NYZS starts to deteriorate, which gives rise to uneven current distribution and further short-circuiting at 3.6 mA cm^{-2} .

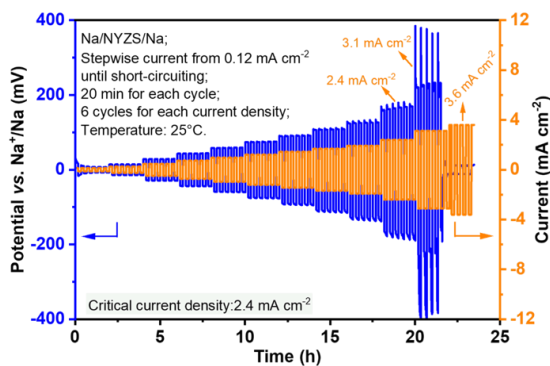


Figure 68 CCD measurement against Na for testing the occurrence of Na metal dendrites with increasing current density until short-circuiting.

The DC polarization curve under the potentiostatic test using Au as blocking electrodes shows negligible electronic conductivity (σ_{electron}) of below $10^{-6} \text{ mS cm}^{-1}$ (**Figure 69**). Therefore, the corresponding Na^+ ionic transference number t_{Na^+} is 1.0 in NYZS, indicating good ionic conducting and electronic insulating properties.[255]

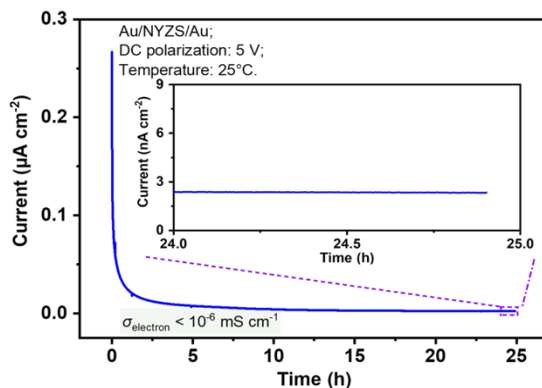


Figure 69 DC polarization curve during potentiostatic test for the electronic conductivity measurement. The inset is the magnified current curve.

The galvanostatic cycling performance was tested in a symmetric Na/NYZS/Na pouch cell (see **Figure 70**), applying a constant pressure of ~ 50 MPa. As shown in **Figure 71**, steady cycling can be carried out for more than 1000 h without significant voltage fluctuations at the current density of 1 mA cm^{-2} and the deposition capacity of 1 mAh cm^{-2} for half cycle. The polarization voltage gradually decreases within the first 100 h, which is attributed to the improved contact area during the redistribution of Na^+ ions under pressure, thus reducing the $R_{\text{interface}}$. The following decreased polarization voltage in the cycling process is dictated by the slight Na dendritic formation (supposed “soft breakdown” before reaching short-circuit) from both sides of the pellet,[256] which can be verified by post-test analysis of EIS and optical inspection (**Figure 72** and **Figure 73**) of the short-circuited cell.

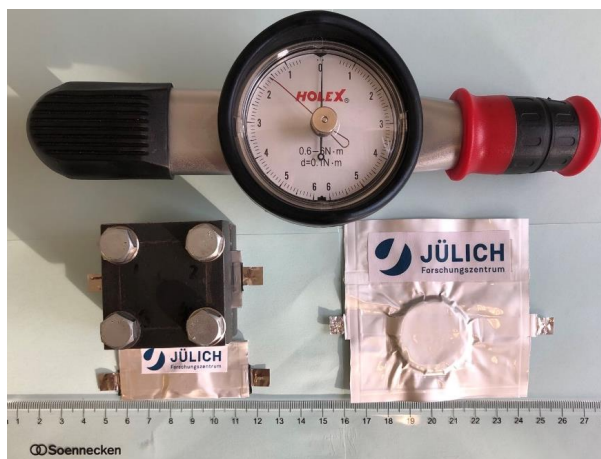


Figure 70 Digital photograph of the pouch cell for the test. The Na/NYZS/Na symmetric pouch cells were assembled in the glovebox.

Then the pouch cell was mounted to the flange for applying pressure, which was monitored by the torsionmeter.

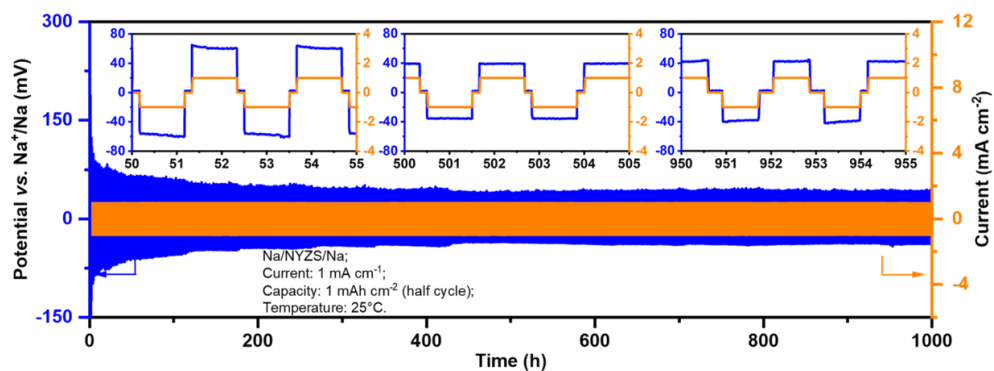


Figure 71 Galvanostatic cycling measurement at the current density of 1 mA cm^{-2} and the deposition capacity of 1 mAh cm^{-2} of NYZS. The insets are the magnified curves at different periods.

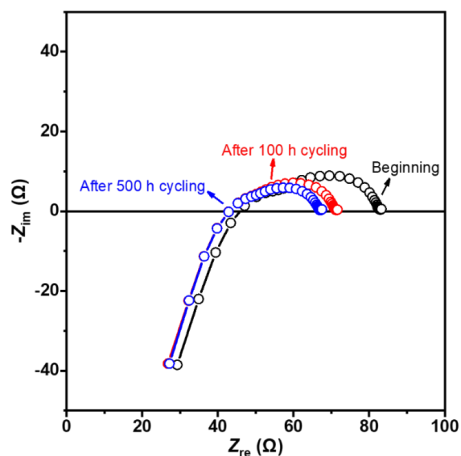


Figure 72 Nyquist plots at different cycling stages in the Na/NYZS/Na symmetric pouch cell.

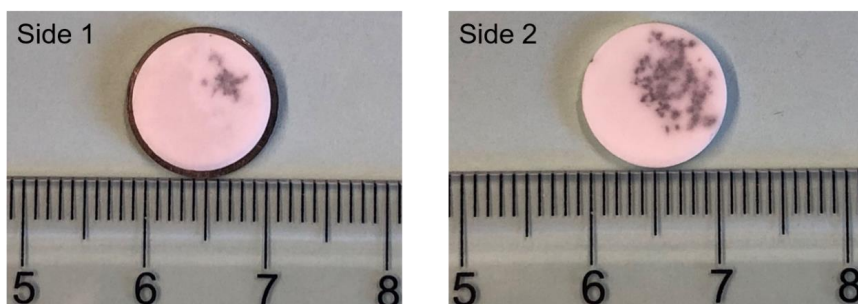


Figure 73 Digital photographs of the NYZS pellet of both sides for post-test analysis in the Na/NYZS/Na symmetric cell after short-circuit.

6.3.3. Analysis of chemical environment with NMR spectroscopy

The ^{23}Na NMR spectra for NYS and NYZS display a sharp peak at ~ 14 ppm and broad overlapping signals between -30 and 8 ppm in **Figure 74**. Due to the strong second-order quadrupolar interaction of the sodium nuclei, the broadening of the resonance cannot be completely averaged with MAS and thus remains unresolved in these 1D spectra.

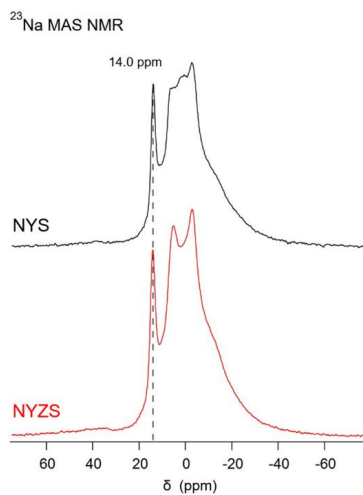


Figure 74 The ^{23}Na magic-angle-spinning nuclear magnetic resonance (MAS NMR) spectra for both NYS and NYZS.

The ^{29}Si MAS spectra (**Figure 75**) for both samples show two resonance peaks at -80.4 and -85.3 ppm representing the two different Si sites, as derived from the structural analysis. The splitting of both resonances in the spectrum of NYS indicates different local environments caused by partially unoccupied neighboring Na sites. In the NYZS sample, this splitting is not observed, revealing a higher degree of local disorder surrounding the $[\text{SiO}_4]$ tetrahedra induced by the incorporation of Zr into the crystal lattice. This also results in an additional resonance at -87.6 ppm, which is assigned to Zr next nearest neighbor around Na.

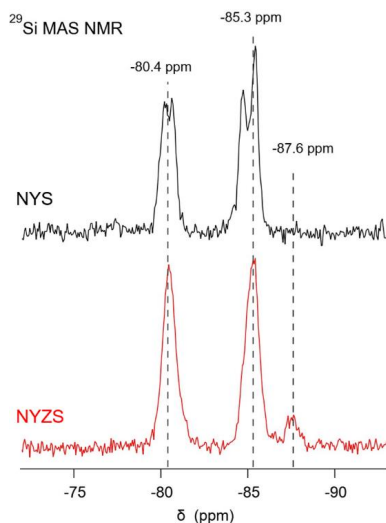


Figure 75 The ^{29}Si magic-angle-spinning nuclear magnetic resonance (MAS NMR) spectra for both NYS and NYZS.

The ^{89}Y MAS NMR spectra (**Figure 76**) for both samples show only a single resonance at 267.5 ppm, consistent with the single Y site in this crystal structure. Again, a line broadening observed for NYZS in comparison to NYS indicates a higher degree of structural disorder caused by Zr in the lattice.

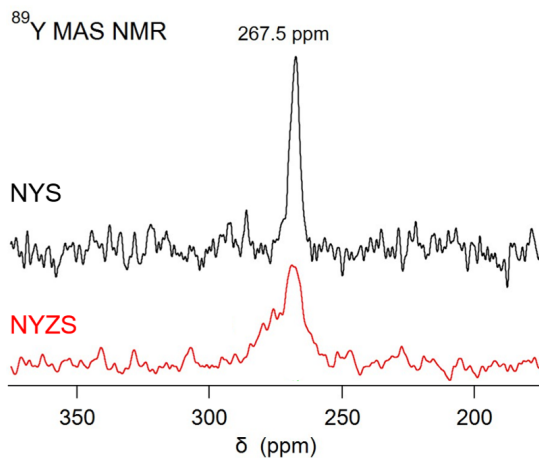


Figure 76 The ^{89}Y magic-angle-spinning nuclear magnetic resonance (MAS NMR) spectra for both NYS and NYZS.

Due to the multiple overlapping signals observed in the 1D ^{23}Na MAS NMR spectra, an additional ^{23}Na multi-quantum (MQ) MAS NMR experiments were performed. The results are shown in **Figure 77a** (NYS) and **Figure 77b** (NYZS), which allow the separation of the isotropic and anisotropic contributions for half-integer quadrupolar sodium nuclei. The narrow resonance at 14 ppm, which was detected for both samples in the ^{23}Na 1D MAS spectra, is labeled with “A”. The broad resonance, as displayed in **Figure 74**, can be separated into a narrower peak at approximately 6 ppm (labeled with “B”) and a broad contribution (labeled with “C”). The NYS sample shows an additional resonance labeled with “D” that was not detected for NYZS. We, therefore, assign this peak to one of the partially occupied Na sites in the crystal structure of NYS that is emptied in NYZS due to the aliovalent substitution of Zr^{4+} for Y^{3+} , as also expressed in the lower Na content per formula unit. The higher number of vacancies of Na sites facilitates the Na^+ ion diffusion in NYZS.

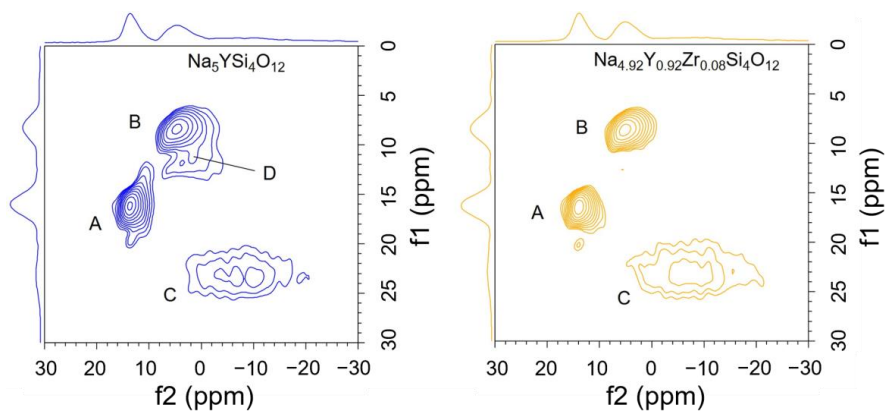


Figure 77 The 2D ^{23}Na MQ MAS NMR spectra of (a) NYS and (b) NYZS.

The temperature-dependent static ^{23}Na NMR spectra were acquired between 260 and 595 K for both samples. The line shapes for the NYS sample are shown in **Figure 78a**. The spectra contain a broad line with a full width at half maximum (FWHM) of 7.4 kHz at 260 K and the peaks become narrower and are shifted to lower ppm values above 400 K. Additionally, a shoulder at the right side of the resonance is formed. At elevated temperatures, the faster motion of the Na^+ ions (with jump rates faster than the static FWHM) results in an averaging of the local sodium environments and causes the motional narrowing of the line shapes. The FWHM decreases to ~ 1.6 kHz at 595 K. The temperature-dependent results of NYZS also display a shift to lower ppm of the resonance as well as motional narrowing at elevated temperatures (**Figure 78b**).

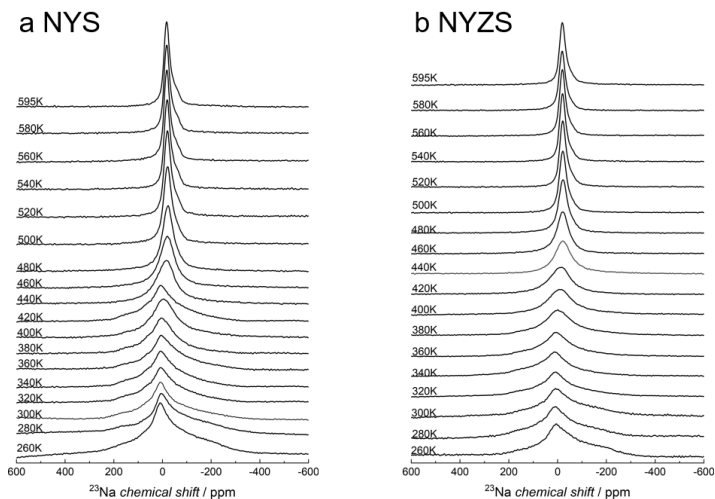


Figure 78 Temperature-dependent static ^{23}Na spectra acquired between 260 and 595 K for (a) NYS and (b) NYZS.

For the NYS and the NYZS samples, the motional narrowing starts at 400 K and 320 K, respectively, and the corresponding temperature-dependent FWHM are shown in **Figure 79a** and **Figure 79b**.

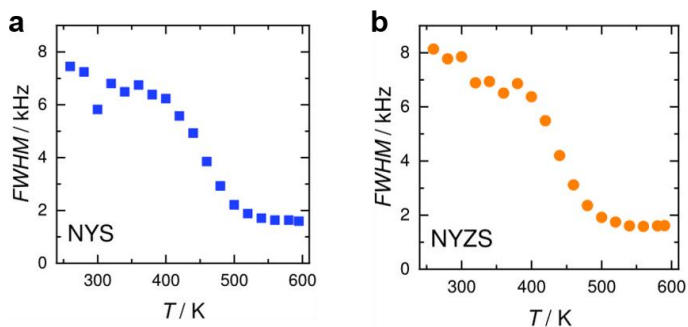


Figure 79 The different contributions are labeled with “A”, “B”, “C” and “D”. Temperature-dependent static ^{23}Na NMR linewidths (full width at half maximum, FWHM) for (a) NYS and (b) NYZS (cf. **Figure 77**).

The local hopping of the Na^+ ions was investigated by determining the relaxation times T_1 using an inversion recovery pulse sequence. These relaxation times are sensitive to motions on time scales τ of the order of the inverse Larmor frequency ($\omega_L^{-1} \approx \text{few ns}$). The temperature dependence of the relaxation rate T_1^{-1} according to the Bloembergen-Purcell-Pound theory (BPP theory) is given by

$$T_1^{-1} \sim \left(\frac{\tau}{1+\omega_L^2\tau^2} + \frac{4\tau}{1+4\omega_L^2\tau^2} \right) \quad (\text{Equation 40})$$

$$\text{with } \tau^{-1} = \tau_0^{-1} \cdot \exp\left(\frac{-E_a}{k_B T}\right) \quad (\text{Equation 41})$$

where E_a is the activation energy, k_B is the Boltzmann constant, T is the thermodynamic temperature and τ is the correlation time which can be associated with the average residence time of the Na^+ ions. Their hopping rate is given by the inverse residence time.

The temperature-dependent results of the relaxation rates T_1^{-1} are shown in **Figure 80a** (NYS) and **Figure 80b** (NYZS). Both samples show a rather similar trend in their relaxation rates. Starting at the lowest temperature (260 K), two different relaxation rates are detected, which can be understood as two different types of Na^+ ions with different hopping rates and, thus also, diffusion pathways and mobility.

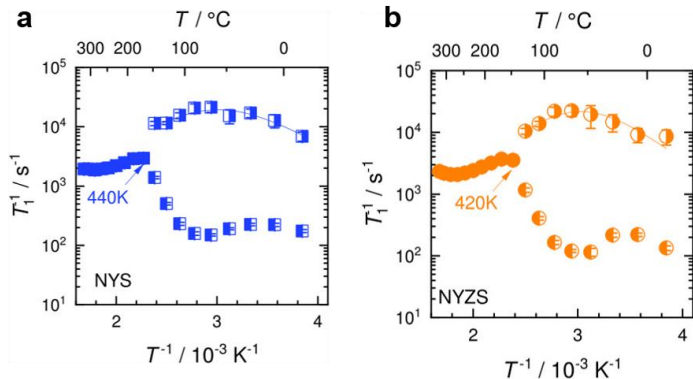


Figure 80 Static ^{23}Na relaxometry: temperature-dependent relaxation rates T_1^{-1} for (e) NYS and (f) NYZS.

The corresponding signal fractions are shown in **Figure 81a** (NYS) and **Figure 81b** (NYZS). The faster relaxation rates of NYS and NYZS have a signal fraction of approximately 20 ~ 25% below 360 K. Above this temperature, the signal fractions approach roughly a 50% distribution until 440 and 420 K, respectively.

The difference between both relaxation rates decreases in the same temperature range. Above 440 K, only one relaxation rate is detectable, and thus all Na^+ ions have enough energy to use the favored (faster) diffusion pathway. Therefore, all Na^+ ions can equally diffuse along both diffusion pathways above this temperature. From the static ^{23}Na relaxometry and line shape analysis, the two distinct migration pathways for Na^+ ions in NYS and NYZS are visible from the experimental perspective.

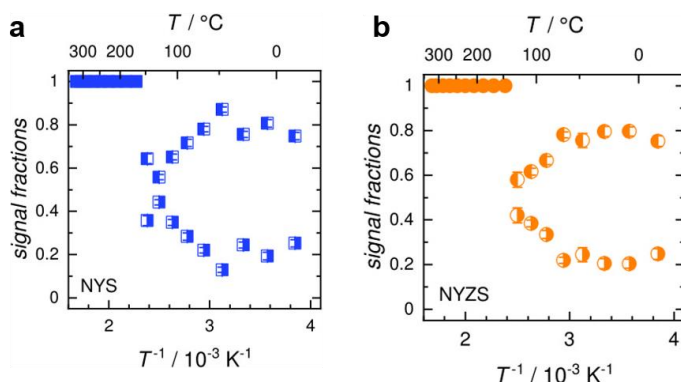


Figure 81 Static ^{23}Na relaxometry: the corresponding signal fractions in the magnetization transients of (g) NYS and (h) NYZS.

The faster relaxation rates for both samples can be fitted with BPP and Arrhenius equations (Equation 54 and Equation 55) in the temperature range from 260 to 420 or 460 K, yielding the temperature-dependent average hopping rate of the Na^+ ions as well as the activation energy E_a . E_a is (0.18 ± 0.02) eV for NYS and (0.23 ± 0.03) eV for NYZS. The average hopping rates τ^{-1} at 298 K are 2.6×10^8 and $2.3 \times 10^8 \text{ s}^{-1}$ for NYS and NYZS, respectively. Here, only the minority component, having the higher relaxation rate, is used. The slower motion of the Na^+ ions characterized by a slower relaxation rate is not taken into account. This explains the differences in the E_a compared to the results of the EIS.

6.3.4. Na^+ ion migration pathways

The bond valence site energy (BVSE) method was used to simulate ionic transport pathways. According to the main rule that atomic valence should be equal to the sum of bond valences around the atom, the two distinct transport pathways that are accessible for mobile Na^+ ions can be obtained, as shown in **Figure 82a**.

Na5 can migrate to the next periodical sites through Na6 to form 1D diffusion channels along the *c* axis, denoted as 5-6-5 (**Figure 82b**). These channels of 5-6-5 are connected by Na4 sites with zigzag chains, denoted as 5(6)-4-5(6) (**Figure 82c**), and a 3D network for Na⁺ ion diffusion forms within the NYZS crystal framework. Based on the results of density functional theory (DFT) simulation, the transport energy barriers of Na⁺ ions along 5-6-5 and 5(6)-4-5(6) in NYS are 1.2 (**Figure 82d**) and 1.5 eV (**Figure 82e**), respectively, while the energy barriers are decreased to 0.9 and 1.1 eV in NYZS. The results indicate that Zr⁴⁺ substitution plays a crucial role in the enhanced conductivity of NYZS, and channel 5-6-5 is the main pathway for Na⁺ ion diffusion. To further clarify the contribution of Zr⁴⁺ substitution to the decrease of the diffusion energy barrier, the charge difference profile that a Na⁺ ion experiences when crossing the bottleneck of channel 5-6-5 was calculated. The slices are fixed on the plane of the Na, Y/Zr and their adjacent O atoms (**Figure 82f**), in which more charges are delocalized around the Na in NYZS (**Figure 82g**) than in NYS (**Figure 82h**), which are attributed to the stronger electrophilicity of Zr than that of Y resulting from the different electronegativity and resulting in a stronger Zr-O bond than Y-O bond. The decreased charges around Na are associated with decreased Na-O bond strength, and increased mobility and contribute to the enhanced conductivity of NYZS, which is also revealed from the 2D ²³Na MQ MAS NMR profiles and the evolved chemical environment after Zr⁴⁺ substitution.

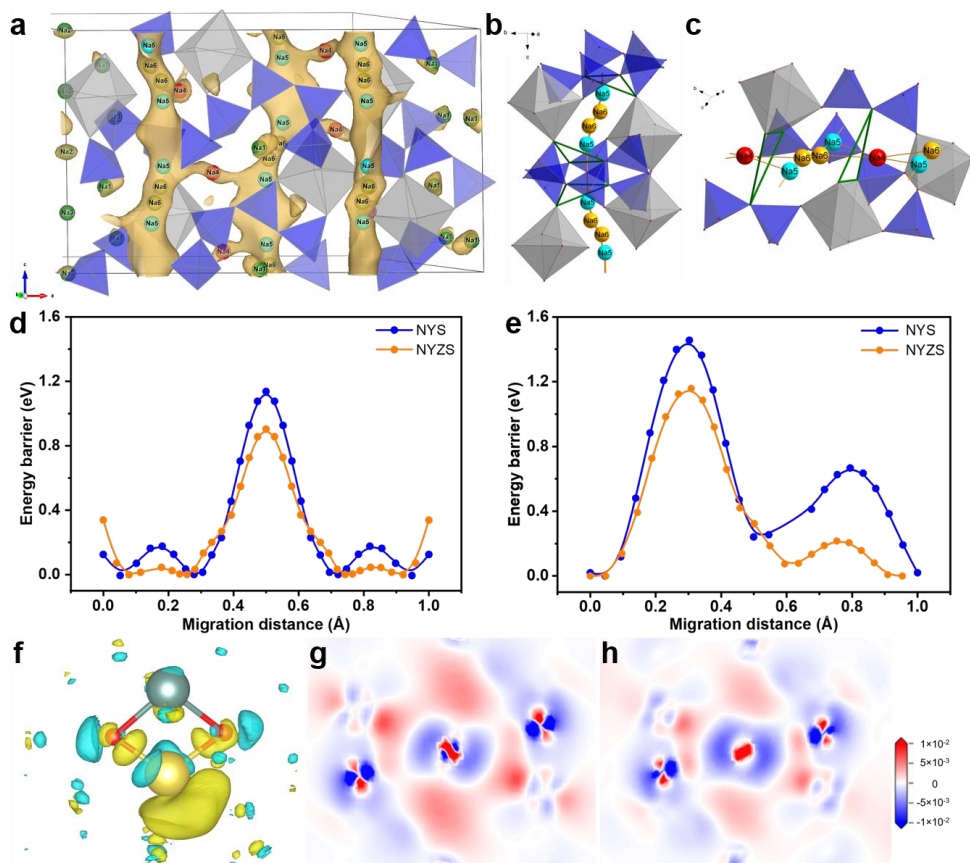


Figure 82 Simulation results for NYS and NYZS.

(a) The two distinct transport pathways within NYZS are revealed by the BVSE method. The vertical channels represent 1D channels 5-6-5, in which the Na^+ ions diffuse along the c axis. Besides, the horizontal channels between adjacent 5-6-5 channels represent channels 5(6)-4-5(6). The 3D Na^+ ion diffusion network is based on the two perpendicular channel systems. The magnified diffusion pathways are shown in (b) channel 5-6-5 and (c) 5(6)-4-5(6). The energy barriers for Na^+ ion diffusion along (d) channel 5-6-5 and (e) channel 5(6)-4-5(6) of both samples reveal lower energy barriers in NYZS. (f) The slices of charge difference of Na between (g) NYZS and (h) NYS show the lower electronic distribution of Na in NYZS. The inset of the contour plot denotes the intensity of the electronic distribution around Na.

6.3.5. Comparison with other investigations on NYS and other oxide-based Na⁺ ionic SSEs

The reports with the most conductive NYS examples are those dealing with single-crystalline materials and revealing ionic conductivities of 5 ~ 7 mS cm⁻¹ at RT (**Figure 83**). [112, 143] Polycrystalline NYS usually shows up to one order of magnitude lower conductivities. [111, 257] The NYS investigated here presents one of the highest $\sigma_{\text{total-RT}}$ values (1.3 mS cm⁻¹), comparable with conductivities obtained for NYS tape [4] or pellet [142] (1 ~ 1.5 mS cm⁻¹). Formerly, the substitutions of Y with rare earth elements showed an influence on conductivity, [111, 144] but the aliovalent substitution with Zr and the increase of sodium vacancies seem to have a more substantial impact on the improvement of the ionic transport. In the case of NYZS, the ionic conductivity is significantly increased to 3.3 mS cm⁻¹ and is already comparable to the extensively studied NASICON materials (e.g., Na_{3.4}Zr₂Si_{2.4}P_{0.6}O₁₂ [132], Na_{3.4}Sc_{0.4}Zr_{1.6}Si₂PO₁₂ [129]) and β'' -Al₂O₃ [258]. In addition, it is worth mentioning that the bulk conductivity of NYZS exactly coincides with the single-crystal measurement of Beyeler *et al.* [143] and the $\sigma_{\text{bulk-RT}}$ is as high as 6.5 mS cm⁻¹. The detailed data are listed in **Table 29**.

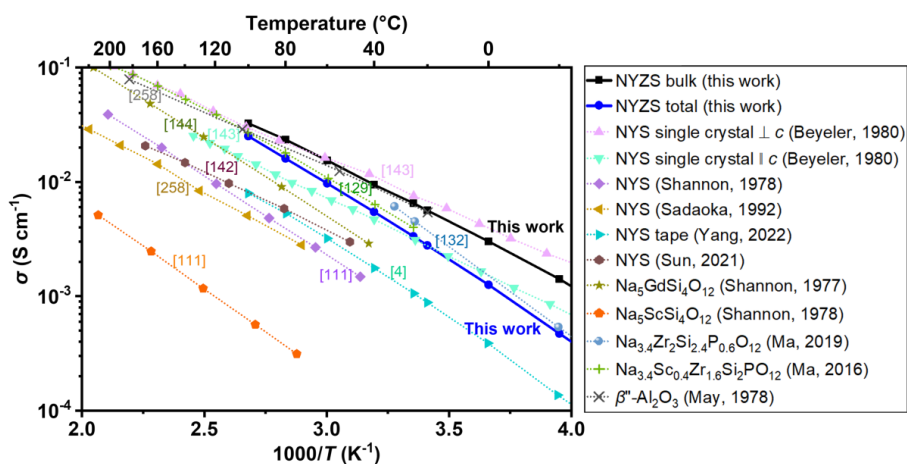


Figure 83 Comparison of electrical conductivity between NYZS and reported representative Na⁺ ionic SSEs.

The Arrhenius plots of NYS single crystal (perpendicular and parallel to c axis), [143] polycrystalline NYS, [111, 142, 257] NYS tape, [4] Na₅GdSi₄O₁₂, [144] Na₅ScSi₄O₁₂, [111] Na_{3.4}Zr₂Si_{2.4}P_{0.6}O₁₂, [132, 259] Na_{3.4}Sc_{0.4}Zr_{1.6}Si₂PO₁₂, [129] β'' -Al₂O₃, [258] NYZS with bulk and total conductivities.

Table 29 Comparison of conductivity and activation energy of NYZS with reported data (Corresponds to **Figure 83**).

Composition	$\sigma_{RT}/\text{mS cm}^{-1}$	E_a/eV	Authors and year	Refs.
Na ₅ YSi ₄ O ₁₂ (single crystal)	3.2 (<i>// c</i> axis);	0.221 (<i>// c</i> axis);	Beyeler <i>et al.</i> , 1980	[143]
	8.0 (\perp <i>c</i> axis)	0.203 (\perp <i>c</i> axis)		
Na ₅ YSi ₄ O ₁₂ (polycrystalline)	100 (300 °C)	0.31	Shannon <i>et al.</i> , 1978	[111]
Na ₅ YSi ₄ O ₁₂ (polycrystalline)	130 (300 °C)	0.21	Sadaoka <i>et al.</i> , 1992	[257]
Na ₅ YSi ₄ O ₁₂ (tape)	1.0	0.30	Yang <i>et al.</i> , 2022	[4]
Na ₅ YSi ₄ O ₁₂ (pellet)	1.59	0.20	Sun <i>et al.</i> , 2021	[142]
Na ₅ GdSi ₄ O ₁₂	300 (300 °C)	0.28	Shannon <i>et al.</i> , 1977	[144]
Na ₅ ScSi ₄ O ₁₂	20 (300 °C)	0.33	Shannon <i>et al.</i> , 1978	[111]
Na _{3.4} Zr ₂ Si _{2.4} P _{0.6} O ₁₂	4.8	0.32	Ma <i>et al.</i> , 2019	[132]
Na _{3.4} Sc _{0.4} Zr _{1.6} Si ₂ PO ₁₂	4.0	0.26	Ma <i>et al.</i> , 2016	[129]
β'' -Al ₂ O ₃	0.08	0.15	May <i>et al.</i> , 1978	[258]
NYZS	3.3	0.30	This work	

In addition to superior σ and typical E_a for Na⁺ ion conduction, the electrochemical stability window and the CCD are parameters determining the electrochemical stability of the materials (shown in **Figure 84**) to be used as SSEs. The detailed information is listed in **Table 30**. Both NYZS and NYS tape/pellet[4, 142] have good electrochemical windows, particularly NYZS exhibits the widest electrochemical window between -0.5 and 10 V, which indicates the high voltage endurance of NYZS, far superior to sulfides[146, 260] and hydrides,[164] etc. NYZS reaches a high CCD of 2.4 mA cm^{-2} at RT, one of the highest values for oxide-based Na⁺ ionic conductors (without interfacial treatment), exhibiting good Na dendrite tolerance.

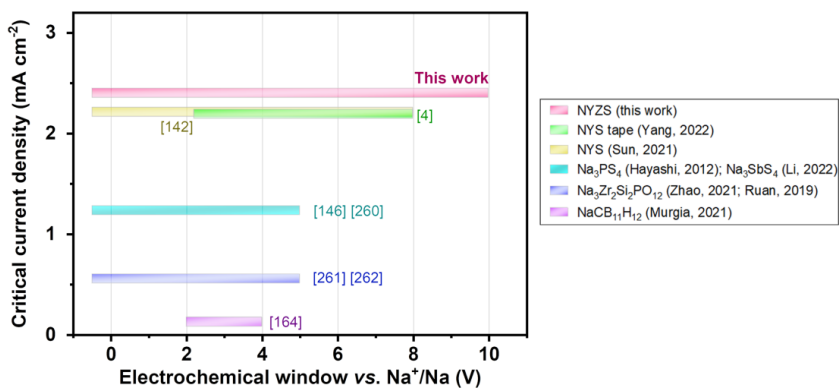


Figure 84 Comparison of electrochemical stability between NYZS and reported representative Na⁺ ionic SSEs.

The integrated comparison of CCD and electrochemical windows of NYS tape,[4] NYS pellet,[142] Na₃PS₄,[146] Na₃SbS₄,[260] Na₃Zr₂Si₂PO₁₂,[261-263] NaCB₁₁H₁₂ [164] and NYZS at RT.

Table 30 Comparison of the CCD and electrochemical window of NYZS with reported work (Corresponds to **Figure 84**).

Composition		CCD/ mA cm ⁻²	Electrochemical windows vs. Na ⁺ /Na/V	Refs.
Sulfides	Na ₃ PS ₄ glass and Na ₃ PS ₄ glass-ceramics (A. Hayashi <i>et al.</i>); Na ₃ SbS ₄ (L. Li <i>et al.</i>)	1.23	-0.5 ~ 5	[146, 260]
Hydrides	NaCB ₁₁ H ₁₂ (F. Murgia <i>et al.</i>)	0.12	2 ~ 4	[164]
Oxides	Na ₃ Zr ₂ Si ₂ PO ₁₂ (Y. Zhao <i>et al.</i> ; Y. Ruan <i>et al.</i>)	0.55	-0.5 ~ 5	[261-263]
	Na ₅ YSi ₄ O ₁₂ tape (A. Yang <i>et al.</i>)	2.2	2.2 ~ 8	[4]
	Na ₅ YSi ₄ O ₁₂ pellet (G. Sun <i>et al.</i>)	2.2	-0.5 ~ 8	[142]
	Na _{4.92} Y _{0.92} Zr _{0.08} Si ₄ O ₁₂ (NYZS)	2.4	-0.5 ~ 10	This work

6.4. Chapter conclusion

In summary, a novel Na⁺ ionic conductor NYZS is reported for the first time and shows high bulk and total conductivities up to 6.5 and 3.3 mS cm⁻¹, respectively. The crystallographic structure and the electrical properties of NYZS are thoroughly studied. By using a facile solid-state reaction approach, the resulting NYZS electrolyte allows high densification (> 95% of relative density), excellent phase purity (~ 95%) and fine grains. From the Rietveld refinement against synchrotron XRD data, the crystal structure and parameters are determined with the space group of $R\bar{3}c$. NYZS is characterized by SiO₄ tetrahedra forming puckered Si₁₂O₃₆ rings parallel to the *c*-axis. Together with MO₆ (M = Y, Zr) octahedra, these puckered rings form a framework containing two channels in the crystal structure, which are filled by mobile Na⁺ ions. It is worth mentioning that NYZS exhibits good environmental stability, with its composition remaining stable and its conductivity not decreasing significantly after three months of exposure to air. The combination of solid-state NMR techniques and theoretical calculations demonstrates that Na⁺ ions have a three-dimensional transportation pathway in NYZS. It also reveals a synergistic effect of increased vacancies and the improved chemical environment with Zr⁴⁺ substitution, which explains the origin of the high conductivity and low activation energy. Considering the simple synthesis method, ultra-high stability and excellent electrochemical properties, NYZS is a very promising SSE for large-scale SSSBs operating at RT.

VII. Conclusion and Perspectives

This thesis focuses on NYS-type Na⁺ superionic conductors and conducted practical applications such as large-scale preparation of thin NYS sheets, their application to Na/S full cells, and exploration of novel electrolyte compositions and conduction mechanisms. The main findings are summarized below:

(1) The aqueous tape casting technique enabled the fabrication of dense silicate-based NYS sheets, which exhibited good Na⁺ ion conductivity ($\sigma_{RT} = 1.0 \text{ mS cm}^{-1}$) and mechanical properties (hardness H of 2 GPa and elastic modulus E of 45 GPa), the low activation energy for Na⁺ ion migration ($E_a = 0.30 \text{ eV}$), and a wide electrochemical stability window (over 8 V vs. Na⁺/Na). The high CCD value of up to 2.2 mA cm^{-2} and stable galvanostatic cycling performance over 280 h at the current density of 0.8 mA cm^{-2} and the capacity of 0.8 mAh cm^{-2} verify the advantages of NYS tape as a qualified solid electrolyte. The aqueous tape casting technique promises environmental compatibility, operational safety and low preparation cost in scaling up, which will be beneficial for the commercialization of NYS-type SSEs.

(2) Following the fabrication of NYS sheets with tape casting, an advanced porous/dense/porous NYS scaffold structure was designed and fabricated. The excellent electrochemical performance was demonstrated in Na/NYS/Na symmetric cells and Na/NYS/S full cells. The Na/NYS/Na symmetric cells with a Pb-coated NYS scaffold exhibited an interfacial impedance as low as $25 \Omega \text{ cm}^2$ and a CCD of up to 3.0 mA cm^{-2} against Na metal. The initial discharge capacity in the pressureless Na/NYS/S cells reached up to 970 mAh g^{-1} and achieved excellent capacity retention of 600 mAh g^{-1} after 150 cycles. The superior performance is attributed to the as-fabricated porous/dense/porous NYS scaffold with high Na⁺ ionic conductivity of 1 mS cm^{-1} at RT, an activation energy as low as 0.29 eV and a stable electrochemical window up to 8 V (vs. Na⁺/Na). Moreover, this particular structural design addresses the issue of vulnerable electrode/electrolyte interfaces that frequently cause challenges in SSBs with sintered composite electrodes. The constructed Na/S full cells show high stability and good electrochemical performance, making the solid-state Na/S battery a promising candidate for practical applications.

(3) Apart from the scalable fabrication of NYS sheets and scaffolds, a novel composition NYZS was synthesized for the first time and showed high bulk and total conductivities up to 6.5 and 3.3 mS cm^{-1} , respectively. The crystallographic structure and the electrical properties of NYZS were thoroughly studied. From the Rietveld refinement against XRD data, the crystal structure and parameters are determined with the space group of $R\bar{3}c$. NYZS is characterized by SiO₄ tetrahedra forming puckered Si₁₂O₃₆ rings parallel to the c -axis. Together with MO₆ ($M = \text{Y, Zr}$) octahedra, these puckered rings form a framework containing two channels in the crystal structure, which are filled by mobile Na⁺ ions. It is worth mentioning that NYZS exhibits good environmental stability, with its composition remaining stable and its conductivity not

decreasing significantly after three months of exposure to air. The combination of SS-NMR techniques and theoretical calculations demonstrated that Na^+ ions have a three-dimensional transportation pathway in NYZS. It also revealed a synergistic effect of increased vacancies and the improved chemical environment with Zr^{4+} substitution, which explains the origin of the high conductivity and low activation energy. Considering the simple synthesis method, ultra-high stability and excellent electrochemical properties, NYZS is a very promising SSE for scalable SSBs.

Although some exciting results have been obtained for NYS-type electrolytes, given the limited RT conductivity and the problematic electrode/electrolyte interface, further research is needed in the following aspects:

(1) Novel NYS-type electrolyte compositions with higher RT ionic conductivity should be further explored. The artificial intelligence-based theoretical calculation can be utilized to discover novel compositions before the experimental synthesis. New synthesis and sintering methods can be employed to realize the high density of the electrolyte and eliminate or decrease the grain-boundary resistance.

(2) The capacity degradation mechanism of Na/S batteries requires further analysis and further suppression strategies. Considering that the discharge and charging processes of the S anode are performed in a stepwise manner, in situ spectroscopy (Raman, IR spectroscopy, etc.) can be used to study the reaction mechanism and irreversible steps.

(3) The discharge-specific capacity and S loading of the full cell based on the S composite cathode need to be further optimized. The energy density of present Na/S cells has a large discrepancy with the theoretical value. Strategies such as optimizing the composite cathode and enhancing the thickness of the cathode can further improve the energy density at the cell level.

(4) Developing high-voltage inorganic cathodes is required to match the NYS-type SSEs with a wide electrochemical stability window. The preparation method and optimization of the morphology of low-cost layered cathode materials (e.g., NaFeSiO_4) are key factors in improving the specific capacity and cycling stability. Meanwhile, how to solve the interfacial compatibility between the inorganic cathode and ceramic electrolyte NYS is also a major challenge for full batteries.

References

- [1] S. Xia, X. Wu, Z. Zhang, Y. Cui, W. Liu, Practical challenges and future perspectives of all-solid-state lithium-metal batteries, *Chem* 5 (2019) 753-785.
- [2] Q. Liu, X. Zhao, Q. Yang, L. Hou, D. Mu, G. Tan, L. Li, R. Chen, F. Wu, The progress in the electrolytes for solid state sodium-ion battery, *Adv. Mater. Technol.* 8 (2023) 2200822
- [3] A. Sivakumaran, A.J. Samson, V. Thangadurai, Progress in sodium silicates for all-solid-state sodium batteries—a Review, *Energy Technol.* 11 (2023) 2201323.
- [4] A. Yang, R. Ye, X. Li, Q. Lu, H. Song, D. Grüner, Q. Ma, F. Tietz, D. Fattakhova-Rohlfing, O. Guillon, Fabrication of thin sheets of the sodium superionic conductor $\text{Na}_5\text{YSi}_4\text{O}_{12}$ with tape casting, *Chem. Eng. J.* 435 (2022) 134774.
- [5] J. Schilm, D. Wagner, C. Heubner, U. Langklotz, C.W. Lee, H.S. Kang, J.W. Park, M. Kusnezoff, Sintering of sodium conducting glass ceramics in the $\text{Na}_2\text{O}-\text{Y}_2\text{O}_3-\text{SiO}_2$ -system, *J. Eur. Ceram. Soc.* 41 (2021) 4876-4883.
- [6] A. Yang, R. Ye, H. Song, Q. Lu, X. Wang, E. Dashjav, K. Yao, D. Grüner, Q. Ma, F. Tietz, O. Guillon, Pressureless all-solid-state Na/S batteries with self-supporting $\text{Na}_5\text{YSi}_4\text{O}_{12}$ scaffolds, *Carbon Energy*, <https://doi.org/10.1002/cey2.371> (2023) e371.
- [7] A. Yang, K. Yao, M. Schaller, E. Dashjav, H. Li, S. Zhao, Q. Zhang, M. Etter, X. Shen, H. Song, Q. Lu, R. Ye, I. Moudrakovski, Q. Pang, S. Indris, X. Wang, Q. Ma, F. Tietz, J. Chen, O. Guillon, Enhanced room-temperature Na^+ ionic conductivity in $\text{Na}_{4.92}\text{Y}_{0.92}\text{Zr}_{0.08}\text{Si}_4\text{O}_{12}$, *eScience* 3 (2023) 100175.
- [8] M. Armand, J.-M. Tarascon, Building better batteries, *Nature* 451 (2008) 652-657.
- [9] M.S. Whittingham, R.F. Savinell, T. Zawodzinski, Introduction: Batteries and fuel cells, *Chem. Rev.* 104 (2004) 4243-4244.
- [10] M. Li, J. Lu, Z. Chen, K. Amine, 30 years of lithium-ion batteries, *Adv. Mater.* 30 (2018) e1800561.
- [11] A. Yoshino, The birth of the lithium-ion battery, *Angew. Chem. Int. Ed.* 51 (2012) 5798-5800.
- [12] R.M. Dell, Batteries fifty years of materials development, *Solid State Ion.* 134 (2000) 139-158.
- [13] M. Winter, B. Barnett, K. Xu, Before Li ion batteries, *Chem. Rev.* 118 (2018) 11433-11456.
- [14] C.P. Grey, J.M. Tarascon, Sustainability and in situ monitoring in battery development, *Nat. Mater.* 16 (2016) 45-56.
- [15] J.-N. Liu, C.-X. Zhao, J. Wang, D. Ren, B.-Q. Li, Q. Zhang, A brief history of zinc–air batteries: 140 years of epic adventures, *Energy Environ. Sci.* 15 (2022) 4542-4553.
- [16] A.B. Gallo, J.R. Simões-Moreira, H.K.M. Costa, M.M. Santos, E. Moutinho dos Santos, Energy storage in the energy transition context: A technology review, *Renew. Sustain. Energy Rev.* 65 (2016) 800-822.
- [17] M.S. Whittingham, Intercalation chemistry and energy storage, *J. Solid State Chem.* 29 (1979) 303-310.
- [18] M.S. Whittingham, Beyond the Nobel recognition – To a cleaner sustainable future, *J. Power Sources* 473 (2020) 228574.
- [19] S. Clark, F.L. Bleken, S. Stier, E. Flores, C.W. Andersen, M. Marcinek, A. Szczesna-Chrzan, M. Gaberscek, M.R. Palacin, M. Uhrin, J. Friis, Toward a unified description of battery data, *Adv. Energy Mater.* 12 (2021) 2102702.
- [20] X. Yang, A.L. Rogach, Electrochemical techniques in battery research: A tutorial for nonelectrochemists, *Adv. Energy Mater.* 9 (2019) 1900747.
- [21] S. Ohno, W.G. Zeier, Sodium is the new lithium, *Nat. Energy* 7 (2022) 686-687.

- [22] K. Chayambuka, G. Mulder, D.L. Danilov, P.H.L. Notten, From Li-ion batteries toward Na-ion chemistries: Challenges and opportunities, *Adv. Energy Mater.* 10 (2020) 2001310.
- [23] T. Shao, C. Liu, W. Deng, C. Li, X. Wang, M. Xue, R. Li, Recent research on strategies to improve ion conduction in alkali metal-ion batteries, *Batteries Supercaps* 2 (2019) 403-427.
- [24] P.P. Kumar, S. Yashonath, Ionic conduction in the solid state, *J. Chem. Sci.* 118 (2006) 135-154.
- [25] Q. Lu, A. Yang, A. Omar, Q. Ma, F. Tietz, O. Guillon, D. Mikhailova, Recent advances in stabilization of sodium metal anode in contact with organic liquid and solid-state electrolytes, *Energy Technol.* 10 (2022) 2200149.
- [26] Q. Zhao, S. Stalin, C.-Z. Zhao, L.A. Archer, Designing solid-state electrolytes for safe, energy-dense batteries, *Nat. Rev. Mater.* 5 (2020) 229-252.
- [27] P.K. Nayak, L. Yang, W. Brehm, P. Adelhelm, From lithium-ion to sodium-ion batteries: Advantages, challenges, and surprises, *Angew. Chem. Int. Ed.* 57 (2018) 102-120.
- [28] A. Rudola, A.J.R. Rennie, R. Heap, S.S. Meysami, A. Lowbridge, F. Mazzali, R. Sayers, C.J. Wright, J. Barker, Commercialisation of high energy density sodium-ion batteries: Faradion's journey and outlook, *J. Mater. Chem. A* 9 (2021) 8279-8302.
- [29] S.Y. Hong, Y. Kim, Y. Park, A. Choi, N.-S. Choi, K.T. Lee, Charge carriers in rechargeable batteries: Na ions vs. Li ions, *Energy Environ. Sci.* 6 (2013) 2067-2081.
- [30] K. Cao, Q. Ma, F. Tietz, B.B. Xu, M. Yan, Y. Jiang, A robust, highly reversible, mixed conducting sodium metal anode, *Sci. Bull.* 66 (2021) 179-186.
- [31] A. Masias, N. Felten, R. Garcia-Mendez, J. Wolfenstine, J. Sakamoto, Elastic, plastic, and creep mechanical properties of lithium metal, *J. Mater. Sci.* 54 (2018) 2585-2600.
- [32] M.J. Wang, J.-Y. Chang, J.B. Wolfenstine, J. Sakamoto, Analysis of elastic, plastic, and creep properties of sodium metal and implications for solid-state batteries, *Materialia* 12 (2020) 100792.
- [33] L. Zhang, T. Yang, C. Du, Q. Liu, Y. Tang, J. Zhao, B. Wang, T. Chen, Y. Sun, P. Jia, H. Li, L. Geng, J. Chen, H. Ye, Z. Wang, Y. Li, H. Sun, X. Li, Q. Dai, Y. Tang, Q. Peng, T. Shen, S. Zhang, T. Zhu, J. Huang, Lithium whisker growth and stress generation in an in situ atomic force microscope-environmental transmission electron microscope set-up, *Nat. Nanotechnol.* 15 (2020) 94-98.
- [34] A. Wang, X. Hu, H. Tang, C. Zhang, S. Liu, Y.W. Yang, Q.H. Yang, J. Luo, Processable and moldable sodium-metal anodes, *Angew. Chem. Int. Ed.* 56 (2017) 11921-11926.
- [35] D. Puthusseri, M. Parmananda, P.P. Mukherjee, V.G. Pol, Probing the thermal safety of Li metal batteries, *J. Electrochem. Soc.* 167 (2020) 120513.
- [36] N. Yabuuchi, K. Kubota, M. Dahbi, S. Komaba, Research development on sodium-ion batteries, *Chem. Rev.* 114 (2014) 11636-11682.
- [37] J. Xie, Y.C. Lu, A retrospective on lithium-ion batteries, *Nat. Commun.* 11 (2020) 2499.
- [38] M.D. Tikekar, S. Choudhury, Z. Tu, L.A. Archer, Design principles for electrolytes and interfaces for stable lithium-metal batteries, *Nat. Energy* 1 (2016) 16114.
- [39] S.T. Oyakhire, W. Zhang, Z. Yu, S.E. Holmes, P. Sayavong, S.C. Kim, D.T. Boyle, M.S. Kim, Z. Zhang, Y. Cui, S.F. Bent, Correlating the formation protocols of solid electrolyte interphases with practical performance metrics in lithium metal batteries, *ACS Energy Lett.* 8 (2023) 869-877.
- [40] H. Zhang, C. Li, G.G. Eshetu, S. Laruelle, S. Grugeon, K. Zaghbi, C. Julien, A. Mauger, D. Guyomard, T. Rojo, N. Gisbert-Trejo, S. Passerini, X. Huang, Z. Zhou, P. Johansson, M. Forsyth, From solid-solution electrodes and the rocking-chair concept to today's batteries, *Angew. Chem. Int. Ed.* 59 (2020) 534-538.
- [41] J.B. Goodenough, Y. Kim, Challenges for rechargeable Li batteries, *Chem. Mater.* 22 (2010) 587-603.

- [42] Y. You, J. Lu, Timely or early? Breaking away from cobalt-reliant lithium-ion batteries, *Next Mater.* 1 (2023) 100004.
- [43] M. Okubo, S. Ko, D. Dwibedi, A. Yamada, Designing positive electrodes with high energy density for lithium-ion batteries, *J. Mater. Chem. A* 9 (2021) 7407-7421.
- [44] M.S. Whittingham, Ultimate limits to intercalation reactions for lithium batteries, *Chem. Rev.* 114 (2014) 11414-11443.
- [45] K. Mizushima, P.C. Jones, P.J. Wiseman, J.B. Goodenough, Li_xCoO_2 ($0 < x \leq 1$): A new cathode material for batteries of high energy density, *Solid State Ion.* 3-4 (1981) 171-174.
- [46] M.S. Whittingham, Lithium batteries and cathode materials, *Chem. Rev.* 104 (2004) 4271-4301.
- [47] R. Koksang, J. Barker, H. Shi, M.Y. Saïdi, Cathode materials for lithium rocking chair batteries, *Solid State Ion.* 84 (1996) 1-21.
- [48] S. Sen, F.H. Richter, Typology of battery cells - From liquid to solid electrolytes, *Adv. Sci.*, <https://doi.org/10.1002/advs.202303985> (2023) e2303985.
- [49] P. Peljo, H.H. Girault, Electrochemical potential window of battery electrolytes: the HOMO–LUMO misconception, *Energy Environ. Sci.* 11 (2018) 2306-2309.
- [50] R. Fong, U.v. Sacken, J.R. Dahn, Studies of lithium intercalation into carbons using nonaqueous electrochemical cells, *J. Electrochem. Soc.* 137 (1990) 2009-2013.
- [51] J.-J. Braconnier, C. Delmas, C. Fouassier, P. Hagemuller, Comportement electrochimique des phases Na_xCoO_2 , *Mater. Res. Bull.* 15 (1980) 1797-1804.
- [52] M.S. Whittingham, Chemistry of intercalation compounds: Metal guests in chalcogenide hosts, *Prog. Solid State Chem.* 12 (1978) 41-99.
- [53] E. Goikolea, V. Palomares, S. Wang, I.R. Larramendi, X. Guo, G. Wang, T. Rojo, Na-ion batteries—Approaching old and new challenges, *Adv. Energy Mater.* 10 (2020) 2002055.
- [54] K. Kubota, M. Dahbi, T. Hosaka, S. Kumakura, S. Komaba, Towards K-ion and Na-ion batteries as "beyond Li-ion", *Chem. Rec.* 18 (2018) 459-479.
- [55] R. Usiskin, Y. Lu, J. Popovic, M. Law, P. Balaya, Y.-S. Hu, J. Maier, Fundamentals, status and promise of sodium-based batteries, *Nat. Rev. Mater.* 6 (2021) 1020-1035.
- [56] Y.E. Durmus, H. Zhang, F. Baakes, G. Desmaizieres, H. Hayun, L. Yang, M. Kolek, V. Küpers, J. Janek, D. Mandler, S. Passerini, Y. Ein-Eli, Side by side battery technologies with lithium-ion based batteries, *Adv. Energy Mater.* 10 (2020) 2000089.
- [57] T. Chen, B. Ouyang, X. Fan, W. Zhou, W. Liu, K. Liu, Oxide cathodes for sodium-ion batteries: Designs, challenges, and perspectives, *Carbon Energy* 4 (2022) 170-199.
- [58] H. Ryu, T. Kim, K. Kim, J.-H. Ahn, T. Nam, G. Wang, H.-J. Ahn, Discharge reaction mechanism of room-temperature sodium-sulfur battery with tetra ethylene glycol dimethyl ether liquid electrolyte, *J. Power Sources* 196 (2011) 5186-5190.
- [59] Y.X. Yin, S. Xin, Y.G. Guo, L.J. Wan, Lithium-sulfur batteries: electrochemistry, materials, and prospects, *Angew. Chem. Int. Ed.* 52 (2013) 13186-13200.
- [60] J. Wu, Y. Tian, Y. Gao, Z. Gao, Y. Meng, Y. Wang, X. Wang, D. Zhou, F. Kang, B. Li, G. Wang, Rational electrolyte design toward cyclability remedy for room-temperature sodium-sulfur batteries, *Angew. Chem. Int. Ed.* 61 (2022) e202205416.
- [61] S. Zhang, Y. Yao, Y. Yu, Frontiers for room-temperature sodium-sulfur batteries, *ACS Energy Lett.* 6 (2021) 529-536.

- [62] P. Wang, Z. Gong, K. Ye, V. Kumar, K. Zhu, L. Sha, J. Yan, J. Yin, K. Cheng, G. Wang, D. Cao, Design and construction of a three-dimensional electrode with biomass-derived carbon current collector and water-soluble binder for high-sulfur-loading lithium-sulfur batteries, *Carbon Energy* 2 (2020) 635-645.
- [63] Z. Yan, Y. Liang, W. Hua, X. Zhang, W.H. Lai, Z. Hu, W. Wang, J. Peng, S. Indris, Y.X. Wang, S. Chou, H.K. Liu, S.X. Dou, Multiregion Janus-featured cobalt phosphide/cobalt composite for highly reversible room-temperature sodium-sulfur batteries, *ACS Nano* 14 (2020) 10284-10293.
- [64] K.B. Hueso, M. Armand, T. Rojo, High temperature sodium batteries: status, challenges and future trends, *Energy Environ. Sci.* 6 (2013) 734-749.
- [65] Z. Wen, Y. Hu, X. Wu, J. Han, Z. Gu, Main challenges for high performance NAS battery: Materials and interfaces, *Adv. Funct. Mater.* 23 (2013) 1005-1018.
- [66] S.K. Vineeth, M. Tebyetekerwa, H. Liu, C.B. Soni, Sungjemmenla, X.S. Zhao, V. Kumar, Progress in the development of solid-state electrolytes for reversible room-temperature sodium-sulfur batteries, *Mater. Adv.* 3 (2022) 6415-6440.
- [67] G.S. Hegde, R. Sundara, A flexible, ceramic-rich solid electrolyte for room-temperature sodium-sulfur batteries, *Chem. Commun.* 58 (2022) 8794-8797.
- [68] C. Vaalma, D. Buchholz, M. Weil, S. Passerini, A cost and resource analysis of sodium-ion batteries, *Nat. Rev. Mater.* 3 (2018) 18013.
- [69] N. Tapia-Ruiz, A.R. Armstrong, H. Alptekin, M.A. Amores, H. Au, J. Barker, R. Boston, W.R. Brant, J.M. Brittain, Y. Chen, M. Chhowalla, Y.-S. Choi, S.I.R. Costa, M. Crespo Ribadeneyra, S.A. Cussen, E.J. Cussen, W.I.F. David, A.V. Desai, S.A.M. Dickson, E.I. Eweka, J.D. Forero-Saboya, C.P. Grey, J.M. Griffin, P. Gross, X. Hua, J.T.S. Irvine, P. Johansson, M.O. Jones, M. Karlsmo, E. Kendrick, E. Kim, O.V. Kolosov, Z. Li, S.F.L. Mertens, R. Mogensen, L. Monconduit, R.E. Morris, A.J. Naylor, S. Nikman, C.A. O'Keefe, D.M.C. Ould, R.G. Palgrave, P. Poizot, A. Ponrouch, S. Renault, E.M. Reynolds, A. Rudola, R. Sayers, D.O. Scanlon, S. Sen, V.R. Seymour, B. Silván, M.T. Sougrati, L. Stievano, G.S. Stone, C.I. Thomas, M.-M. Titirici, J. Tong, T.J. Wood, D.S. Wright, R. Younesi, 2021 roadmap for sodium-ion batteries, *JPhys. Energy* 3 (2021) 031503.
- [70] S. Comello, S. Reichelstein, The emergence of cost effective battery storage, *Nat. Commun.* 10 (2019) 2038.
- [71] B. Sayahpour, H. Hirsh, S. Parab, L.H.B. Nguyen, M. Zhang, Y.S. Meng, Perspective: Design of cathode materials for sustainable sodium-ion batteries, *MRS Energy Sustain.* 9 (2022) 183-197.
- [72] I. Hasa, S. Mariyappan, D. Saurel, P. Adelhelm, A.Y. Kuposov, C. Masquelier, L. Croguennec, M. Casas-Cabanas, Challenges of today for Na-based batteries of the future: From materials to cell metrics, *J. Power Sources* 482 (2021) 228872.
- [73] V. Pande, V. Viswanathan, Computational screening of current collectors for enabling anode-free lithium metal batteries, *ACS Energy Lett.* 4 (2019) 2952-2959.
- [74] Y. Lu, X. Rong, Y.-S. Hu, L. Chen, H. Li, Research and development of advanced battery materials in China, *Energy Storage Mater.* 23 (2019) 144-153.
- [75] W. Liu, P. Liu, D. Mitlin, Tutorial review on structure – dendrite growth relations in metal battery anode supports, *Chem. Soc. Rev.* 49 (2020) 7284-7300.
- [76] N.S. Muhammed Hafiz, G. Singla, P. Kumar Jha, Next generation sodium-ion battery: A replacement of lithium, *Mater. Today: Proc.*, <https://doi.org/10.1016/j.matpr.2022.11.245> (2022)
- [77] J.T. Frith, M.J. Lacey, U. Ulissi, A non-academic perspective on the future of lithium-based batteries, *Nat. Commun.* 14 (2023) 420.

- [78] J.-M. Tarascon, Na-ion versus Li-ion batteries: Complementarity rather than competitiveness, *Joule* 4 (2020) 1-5.
- [79] M. Balaish, J.C. Gonzalez-Rosillo, K.J. Kim, Y. Zhu, Z.D. Hood, J.L.M. Rupp, Processing thin but robust electrolytes for solid-state batteries, *Nat. Energy* 6 (2021) 227-239.
- [80] T. Placke, R. Kloepsch, S. Dühnen, M. Winter, Lithium ion, lithium metal, and alternative rechargeable battery technologies: the odyssey for high energy density, *J. Solid State Electrochem.* 21 (2017) 1939-1964.
- [81] Y.-S. Hu, Batteries: Getting solid, *Nat. Energy* 1 (2016) 16042.
- [82] Y. Liang, H. Liu, G. Wang, C. Wang, Y. Ni, C.W. Nan, L.Z. Fan, Challenges, interface engineering, and processing strategies toward practical sulfide-based all-solid-state lithium batteries, *InfoMat* 4 (2022) e12292.
- [83] Y. Gambe, Y. Sun, I. Honma, Development of bipolar all-solid-state lithium battery based on quasi-solid-state electrolyte containing tetraglyme-LiTFSa equimolar complex, *Sci. Rep.* 5 (2015) 8869.
- [84] J.A.S. Oh, X. Xu, Z. Zeng, K. Wang, N.Y.J. Tan, E. Kok, J. Huang, L. Lu, Thin NASICON electrolyte to realize high energy density solid-state sodium metal battery, *Energy Environ. Mater.*, <https://doi.org/10.1002/eem2.12472> (2022) e12472.
- [85] W. Luo, L. Hu, Na metal anode: "Holy grail" for room-temperature Na-ion batteries?, *ACS Cent. Sci.* 1 (2015) 420-422.
- [86] Y.B. Song, K.H. Baeck, H. Kwak, H. Lim, Y.S. Jung, Dimensional strategies for bridging the research gap between lab-scale and potentially practical all-solid-state batteries: The role of sulfide solid electrolyte films, *Adv. Energy Mater.* 13 (2023) 2301142.
- [87] C. Wang, X. Sun, The promise of solid-state batteries for safe and reliable energy storage, *Engineering* 31 (2023) 32-35.
- [88] C.P. Aiken, N. Kowalski, R.C. Fitzner, S. Trussler, J.E. Harlow, E.J. Butler, J.R. Dahn, Tracking electrolyte motion in cylindrical Li-ion cells using moment of inertia measurements, *J. Electrochem. Soc.* 170 (2023) 040529.
- [89] K. Zhang, F. Wu, X. Wang, S. Weng, X. Yang, H. Zhao, R. Guo, Y. Sun, W. Zhao, T. Song, X. Wang, Y. Bai, C. Wu, 8.5 μm -thick flexible-rigid hybrid solid–electrolyte/lithium integration for air-stable and interface-compatible all-solid-state lithium metal batteries, *Adv. Energy Mater.* 12 (2022) 2200368.
- [90] J. Janek, W.G. Zeier, Challenges in speeding up solid-state battery development, *Nat. Energy* 8 (2023) 230–240.
- [91] O. Maus, M.T. Agne, T. Fuchs, P.S. Till, B. Wankmiller, J.M. Gerdes, R. Sharma, M. Heere, N. Jalarvo, O. Yaffe, M.R. Hansen, W.G. Zeier, On the discrepancy between local and average structure in the fast Na^+ ionic conductor $\text{Na}_{2.9}\text{Sb}_{0.9}\text{W}_{0.1}\text{S}_4$, *J. Am. Chem. Soc.* 145 (2023) 7147-7158.
- [92] T. Fuchs, S.P. Culver, P. Till, W.G. Zeier, Defect-mediated conductivity enhancements in $\text{Na}_{3-x}\text{Pn}_{1-x}\text{W}_x\text{S}_4$ (Pn = P, Sb) using aliovalent substitutions, *ACS Energy Lett.* 5 (2019) 146-151.
- [93] J. Janek, W.G. Zeier, A solid future for battery development, *Nat. Energy* 1 (2016) 16141.
- [94] J.B. Goodenough, P. Singh, Review—Solid electrolytes in rechargeable electrochemical cells, *J. Electrochem. Soc.* 162 (2015) A2387-A2392.
- [95] Y. Kato, S. Hori, T. Saito, K. Suzuki, M. Hirayama, A. Mitsui, M. Yonemura, H. Iba, R. Kanno, High-power all-solid-state batteries using sulfide superionic conductors, *Nat. Energy* 1 (2016) 16030.
- [96] W. Zaman, K.B. Hatzell, Processing and manufacturing of next generation lithium-based all solid-state batteries, *Curr. Opin. Solid State Mater. Sci.* 26 (2022) 101003.

- [97] L. Schweiger, K. Hogrefe, B. Gadermaier, J.L.M. Rupp, H.M.R. Wilkening, Ionic conductivity of nanocrystalline and amorphous $\text{Li}_{10}\text{GeP}_2\text{S}_{12}$: The detrimental impact of local disorder on ion transport, *J. Am. Chem. Soc.* 144 (2022) 9597-9609.
- [98] D.H.S. Tan, Y.S. Meng, J. Jang, Scaling up high-energy-density sulfidic solid-state batteries: A lab-to-pilot perspective, *Joule* 6 (2022) 1755-1769.
- [99] P. Adelhelm, P. Hartmann, C.L. Bender, M. Busche, C. Eufinger, J. Janek, From lithium to sodium: cell chemistry of room temperature sodium-air and sodium-sulfur batteries, *Beilstein J. Nanotechnol.* 6 (2015) 1016-1055.
- [100] C. Bauer, S. Burkhardt, N.P. Dasgupta, L.A.-W. Ellingsen, L.L. Gaines, H. Hao, R. Hischer, L. Hu, Y. Huang, J. Janek, C. Liang, H. Li, J. Li, Y. Li, Y.-C. Lu, W. Luo, L.F. Nazar, E.A. Olivetti, J.F. Peters, J.L.M. Rupp, M. Weil, J.F. Whitacre, S. Xu, Charging sustainable batteries, *Nat. Sustain.* 5 (2022) 176-178.
- [101] M. Dixit, C. Beamer, R. Amin, J. Shipley, R. Eklund, N. Muralidharan, L. Lindqvist, A. Fritz, R. Esshli, M. Balasubramanian, I. Belharouak, The role of isostatic pressing in large-scale production of solid-state batteries, *ACS Energy Lett.* 7 (2022) 3936-3946.
- [102] Y. Xiao, K. Turcheniuk, A. Narla, A.Y. Song, X. Ren, A. Magasinski, A. Jain, S. Huang, H. Lee, G. Yushin, Electrolyte melt infiltration for scalable manufacturing of inorganic all-solid-state lithium-ion batteries, *Nat. Mater.* 20 (2021) 984-990.
- [103] D. Landmann, G. Graeber, M.V.F. Heinz, S. Haussener, C. Battaglia, Sodium plating and stripping from $\text{Na-}\beta$ -alumina ceramics beyond 1000 mA/cm^2 , *Mater. Today Energy* 18 (2020) 100515.
- [104] J. Yang, G. Liu, M. Avdeev, H. Wan, F. Han, L. Shen, Z. Zou, S. Shi, Y.-S. Hu, C. Wang, X. Yao, Ultrastable all-solid-state sodium rechargeable batteries, *ACS Energy Lett.* 5 (2020) 2835-2841.
- [105] H.U. Beyeler, T. Hibma, The sodium conductivity paths in the superionic conductors $\text{Na}_5\text{RESi}_4\text{O}_{12}$, *Solid State Commun.* 27 (1978) 641-643.
- [106] F. Tsuji, N. Masuzawa, A. Sakuda, M. Tatsumisago, A. Hayashi, Preparation and characterization of cation-substituted Na_3SbS_4 solid electrolytes, *ACS Appl. Energy Mater.* 3 (2020) 11706-11712.
- [107] J.-F. Wu, Z.-Y. Yu, Q. Wang, X. Guo, High performance all-solid-state sodium batteries actualized by polyethylene oxide/ $\text{Na}_2\text{Zn}_2\text{TeO}_6$ composite solid electrolytes, *Energy Storage Mater.* 24 (2020) 467-471.
- [108] W. Niu, L. Chen, Y. Liu, L.-Z. Fan, All-solid-state sodium batteries enabled by flexible composite electrolytes and plastic-crystal interphase, *Chem. Eng. J.* 384 (2020) 123233.
- [109] R. Knödler, Thermal properties of sodium-sulphur cells, *J. Appl. Electrochem.* 14 (1984) 39-46.
- [110] M.P. Fertig, K. Skadell, M. Schulz, C. Dirksen, P. Adelhelm, M. Stelter, From high- to low-temperature: The revival of sodium-beta alumina for sodium solid-state batteries, *Batteries Supercaps* 5 (2021) e202100131.
- [111] R.D. Shannon, B.E. Taylor, T.E. Gier, H.-Y. Chen, T. Berzins, Ionic conductivity in $\text{Na}_5\text{YSi}_4\text{O}_{12}$ -type silicates, *Inorg. Chem.* 17 (1978) 958-964.
- [112] B.A. Maksimov, Y.A. Kharitonov, N.V. Belov, Crystal structure of the Na-Y metasilicate $\text{Na}_5\text{YSi}_4\text{O}_{12}$, *Sov. Phys. Dokl.* 18 (1974) 763-765.
- [113] H.Y.-P. Hong, J.A. Kafalas, M. Bayard, High Na^+ -ion conductivity in $\text{Na}_5\text{YSi}_4\text{O}_{12}$, *Mater. Res. Bull.* 13 (1978) 757-761.
- [114] T.M. Gür, Review of electrical energy storage technologies, materials and systems: challenges and prospects for large-scale grid storage, *Energy Environ. Sci.* 11 (2018) 2696-2767.
- [115] Z. Wen, J. Cao, Z. Gu, X. Xu, F. Zhang, Z. Lin, Research on sodium sulfur battery for energy storage, *Solid State Ion.* 179 (2008) 1697-1701.

- [116] Z. Yang, J. Zhang, M.C. Kintner-Meyer, X. Lu, D. Choi, J.P. Lemmon, J. Liu, Electrochemical energy storage for green grid, *Chem. Rev.* 111 (2011) 3577-3613.
- [117] G. Yamaguchi, K. Suzuki, On the structures of alkali polyaluminates, *Bull. Chem. Soc. Jpn.* 41 (1968) 93-99.
- [118] X. Lu, G. Xia, J.P. Lemmon, Z. Yang, Advanced materials for sodium-beta alumina batteries: Status, challenges and perspectives, *J. Power Sources* 195 (2010) 2431-2442.
- [119] K. Koganei, T. Oyama, M. Inada, N. Enomoto, K. Hayashi, C-axis oriented β'' -alumina ceramics with anisotropic ionic conductivity prepared by spark plasma sintering, *Solid State Ion.* 267 (2014) 22-26.
- [120] J.T. Kummer, β -alumina electrolytes, *Prog. Solid State Chem.* 7 (1972) 141-175.
- [121] J.-H. Kim, E.-C. Shin, D.-C. Cho, S. Kim, S. Lim, K. Yang, J. Beum, J. Kim, S. Yamaguchi, J.-S. Lee, Electrical characterization of polycrystalline sodium β'' -alumina: Revisited and resolved, *Solid State Ion.* 264 (2014) 22-35.
- [122] K. Zhao, Y. Liu, S. Zhang, S. He, N. Zhang, J. Yang, Z. Zhan, A room temperature solid-state rechargeable sodium ion cell based on a ceramic Na- β'' -Al₂O₃ electrolyte and NaTi₂(PO₄)₃ cathode, *Electrochem. Commun.* 69 (2016) 59-63.
- [123] L. Zhang, Y. Liu, Y. You, A. Vinu, L. Mai, NASICONs-type solid-state electrolytes: The history, physicochemical properties, and challenges, *Interdiscip. Mater.* 2 (2022) 91-110.
- [124] J.B. Goodenough, H.Y.-P. Hong, J.A. Kafalas, Fast Na⁺-ion transport in skeleton structures, *Mater. Res. Bull.* 11 (1976) 203-220.
- [125] H.Y.-P. Hong, Crystal structures and crystal chemistry in the system Na_{1+x}Zr₂Si_xP_{3-x}O₁₂, *Mater. Res. Bull.* 11 (1976) 173-182.
- [126] R. Rajagopalan, Z. Zhang, Y. Tang, C. Jia, X. Ji, H. Wang, Understanding crystal structures, ion diffusion mechanisms and sodium storage behaviors of NASICON materials, *Energy Storage Mater.* 34 (2021) 171-193.
- [127] J. Zhang, Y. Liu, X. Zhao, L. He, H. Liu, Y. Song, S. Sun, Q. Li, X. Xing, J. Chen, A novel NASICON-type Na₄MnCr(PO₄)₃ demonstrating the energy density record of phosphate cathodes for sodium-ion batteries, *Adv. Mater.* 32 (2020) 1906348.
- [128] J.F. Ortiz-Mosquera, A.M. Nieto-Munoz, A.C.M. Rodrigues, New Na_{1+x}Ge₂(SiO₄)_x(PO₄)_{3-x} NASICON series with improved grain and grain boundary conductivities, *ACS Appl. Mater. Interfaces* 12 (2020) 13914-13922.
- [129] Q. Ma, M. Guin, S. Naqash, C.-L. Tsai, F. Tietz, O. Guillon, Scandium-substituted Na₃Zr₂(SiO₄)₂(PO₄) prepared by a solution-assisted solid-state reaction method as sodium-ion conductors, *Chem. Mater.* 28 (2016) 4821-4828.
- [130] C. Zhao, L. Liu, X. Qi, Y. Lu, F. Wu, J. Zhao, Y. Yu, Y.-S. Hu, L. Chen, Solid-state sodium batteries, *Adv. Energy Mater.* 8 (2018) 1703012.
- [131] Z. Yang, B. Tang, Z. Xie, Z. Zhou, NASICON-type Na₃Zr₂Si₂PO₁₂ solid-state electrolytes for sodium batteries, *ChemElectroChem* 8 (2021) 1035-1047.
- [132] Q. Ma, C.-L. Tsai, X.-K. Wei, M. Heggen, F. Tietz, J.T.S. Irvine, Room temperature demonstration of a sodium superionic conductor with grain conductivity in excess of 0.01 S cm⁻¹ and its primary applications in symmetric battery cells, *J. Mater. Chem. A* 7 (2019) 7766-7776.
- [133] X. Wang, W. Mei, J. Chen, D. Wang, Z. Mao, Rare earth oxide-assisted sintered NASICON electrolyte composed of a phosphate grain boundary phase with low electronic conductivity, *ACS Appl. Energy Mater.* 5 (2022) 777-783.

- [134] J. Pengfeng, D. Guangyuan, S. Yuansheng, S. Fengquan, G. Pengqian, Q. Guoyu, L. Xueyi, X. Fangyan, L. Xia, Ultrafast sintering of $\text{Na}_3\text{Zr}_2\text{Si}_2\text{PO}_{12}$ solid electrolyte for long lifespan solid-state sodium ion batteries, *Chem. Eng. J.* 451 (2023) 138771.
- [135] T. Takahashi, K. Kuwabara, M. Shibata, Solid-state ionics-conductivities of Na^+ ion conductors based on NASICON, *Solid State Ion.* 1 (1980) 163-175.
- [136] M. Guin, F. Tietz, Survey of the transport properties of sodium superionic conductor materials for use in sodium batteries, *J. Power Sources* 273 (2015) 1056-1064.
- [137] E.M. Vogel, R.J. Cava, E. Rietman, Na^+ ion conductivity and crystallographic cell characterization in the Hf-NASICON system $\text{Na}_{1+x}\text{Hf}_2\text{Si}_x\text{P}_{3-x}\text{O}_{12}$, *Solid State Ion.* 14 (1984) 1-6.
- [138] C. Wang, Z. Sun, Y. Zhao, B. Wang, C. Shao, C. Sun, Y. Zhao, J. Li, H. Jin, L. Qu, Grain boundary design of solid electrolyte actualizing stable all-solid-state sodium batteries, *Small* 17 (2021) e2103819.
- [139] H. Yamauchi, J. Ikejiri, F. Sato, H. Oshita, T. Honma, T. Komatsu, Pressureless all-solid-state sodium-ion battery consisting of sodium iron pyrophosphate glass-ceramic cathode and β'' -alumina solid electrolyte composite, *J. Am. Ceram. Soc.* 102 (2019) 6658-6667.
- [140] T. Lan, C.-L. Tsai, F. Tietz, X.-K. Wei, M. Heggen, R.E. Dunin-Borkowski, R. Wang, Y. Xiao, Q. Ma, O. Guillon, Room-temperature all-solid-state sodium batteries with robust ceramic interface between rigid electrolyte and electrode materials, *Nano Energy* 65 (2019) 104040.
- [141] T. Okura, N. Yoshida, K. Yamashita, Na^+ superionic conducting silicophosphate glass-ceramics—Review, *Solid State Ion.* 285 (2016) 143-154.
- [142] G. Sun, X. Yang, N. Chen, S. Yao, X. Wang, X. Jin, G. Chen, Y. Xie, F. Du, $\text{Na}_5\text{YSi}_4\text{O}_{12}$: A sodium superionic conductor for ultrastable quasi-solid-state sodium-ion batteries, *Energy Storage Mater.* 41 (2021) 196-202.
- [143] H.U. Beyeler, R.D. Shannon, H.Y. Chen, Ionic conductivity of single-crystal $\text{Na}_5\text{YSi}_4\text{O}_{12}$, *Appl. Phys. Lett.* 37 (1980) 934-935.
- [144] R.D. Shannon, H.-Y. Chert, T. Berzins, Ionic conductivity in $\text{Na}_5\text{GdSi}_4\text{O}_{12}$, *Mater. Res. Bull.* 12 (1977) 969-973.
- [145] Z. Zhang, E. Ramos, F. Lalère, A. Assoud, K. Kaup, P. Hartman, L.F. Nazar, $\text{Na}_{11}\text{Sn}_2\text{PS}_{12}$: A new solid state sodium superionic conductor, *Energy Environ. Sci.* 11 (2018) 87-93.
- [146] A. Hayashi, K. Noi, A. Sakuda, M. Tatsumisago, Superionic glass-ceramic electrolytes for room-temperature rechargeable sodium batteries, *Nat. Commun.* 3 (2012) 856.
- [147] S. Takeuchi, K. Suzuki, M. Hirayama, R. Kanno, Sodium superionic conduction in tetragonal Na_3PS_4 , *J. Solid State Chem.* 265 (2018) 353-358.
- [148] N. Tanibata, K. Noi, A. Hayashi, M. Tatsumisago, Preparation and characterization of Na_3PS_4 – Na_4GeS_4 glass and glass-ceramic electrolytes, *Solid State Ion.* 320 (2018) 193-198.
- [149] A. Hayashi, N. Masuzawa, S. Yubuchi, F. Tsuji, C. Hotehama, A. Sakuda, M. Tatsumisago, A sodium-ion sulfide solid electrolyte with unprecedented conductivity at room temperature, *Nat. Commun.* 10 (2019) 5266.
- [150] A. Hayashi, K. Noi, N. Tanibata, M. Nagao, M. Tatsumisago, High sodium ion conductivity of glass-ceramic electrolytes with cubic Na_3PS_4 , *J. Power Sources* 258 (2014) 420-423.
- [151] Y. Wang, W.D. Richards, S.-H. Bo, L.J. Miara, G. Ceder, Computational prediction and evaluation of solid-state sodium superionic conductors $\text{Na}_7\text{P}_3\text{X}_{11}$ (X = O, S, Se), *Chem. Mater.* 29 (2017) 7475-7482.
- [152] H. Wang, Y. Chen, Z.D. Hood, G. Sahu, A.S. Pandian, J.K. Keum, K. An, C. Liang, An air-stable Na_3SbS_4 superionic conductor prepared by a rapid and economic synthetic procedure, *Angew. Chem. Int. Ed.* 55 (2016) 8551-8555.

- [153] Z. Yu, S.L. Shang, J.H. Seo, D. Wang, X. Luo, Q. Huang, S. Chen, J. Lu, X. Li, Z.K. Liu, D. Wang, Exceptionally high ionic conductivity in $\text{Na}_3\text{P}_{0.62}\text{As}_{0.38}\text{S}_4$ with improved moisture stability for solid-state sodium-ion batteries, *Adv. Mater.* 29 (2017) 1605561.
- [154] I.H. Chu, C.S. Kompella, H. Nguyen, Z. Zhu, S. Hy, Z. Deng, Y.S. Meng, S.P. Ong, Room-temperature all-solid-state rechargeable sodium-ion batteries with a Cl-doped Na_3PS_4 superionic conductor, *Sci. Rep.* 6 (2016) 33733.
- [155] M.A. Kraft, L.M. Gronych, T. Famprikis, S. Ohno, W.G. Zeier, Structure and sodium ion transport in $\text{Na}_{1+x}\text{Sn}_{2+x}(\text{Sb}_{1-y}\text{P}_y)_{1-x}\text{S}_{12}$, *Chem. Mater.* 32 (2020) 6566-6576.
- [156] S. Wenzel, T. Leichtweiss, D.A. Weber, J. Sann, W.G. Zeier, J. Janek, Interfacial reactivity benchmarking of the sodium ion conductors Na_3PS_4 and sodium beta-alumina for protected sodium metal anodes and sodium all-solid-state batteries, *ACS Appl. Mater. Interfaces* 8 (2016) 28216-28224.
- [157] Y. Tian, T. Shi, W.D. Richards, J. Li, J.C. Kim, S.-H. Bo, G. Ceder, Compatibility issues between electrodes and electrolytes in solid-state batteries, *Energy Environ. Sci.* 10 (2017) 1150-1166.
- [158] M. Shoji, E.J. Cheng, T. Kimura, K. Kanamura, Recent progress for all solid state battery using sulfide and oxide solid electrolytes, *J. Phys. D: Appl. Phys.* 52 (2019) 103001.
- [159] P. Lin-Feng, Z. Zi-Qi, S. Yu-Long, J. Huan-Huan, X. Jia, Facile synthesis and electrochemical properties of Na-rich anti-perovskite solid electrolytes, *Acta. Phys. Sin.* 69 (2020) 228201.
- [160] J.A. Dawson, T. Famprikis, K.E. Johnston, Anti-perovskites for solid-state batteries: recent developments, current challenges and future prospects, *J. Mater. Chem. A* 9 (2021) 18746-18772.
- [161] W. Xia, Y. Zhao, F. Zhao, K. Adair, R. Zhao, S. Li, R. Zou, Y. Zhao, X. Sun, Antiperovskite electrolytes for solid-state batteries, *Chem. Rev.* 122 (2022) 3763-3819.
- [162] L. Duchêne, R.S. Kühnel, E. Stilp, E. Cuervo Reyes, A. Remhof, H. Hagemann, C. Battaglia, A stable 3 V all-solid-state sodium-ion battery based on a closo-borate electrolyte, *Energy Environ. Sci.* 10 (2017) 2609-2615.
- [163] T.J. Udovic, M. Matsuo, W.S. Tang, H. Wu, V. Stavila, A.V. Soloninin, R.V. Skoryunov, O.A. Babanova, A.V. Skripov, J.J. Rush, A. Unemoto, H. Takamura, S. Orimo, Exceptional superionic conductivity in disordered sodium decahydro-closo-decaborate, *Adv. Mater.* 26 (2014) 7622-7626.
- [164] F. Murgia, M. Brighi, L. Piveteau, C.E. Avalos, V. Gulino, M.C. Nierstenhofer, P. Ngene, P. de Jongh, R. Cerny, Enhanced room-temperature ionic conductivity of $\text{NaCB}_{11}\text{H}_{12}$ via high-energy mechanical milling, *ACS Appl. Mater. Interfaces* 13 (2021) 61346-61356.
- [165] A.K.I. V-Shitz, Superionic conductors with intrinsic and impurity-induced structure disorder, *Bull. Soc. Cat. Gen.* 12 (1991) 435-451.
- [166] Y. Lu, L. Li, Q. Zhang, Z. Niu, J. Chen, Electrolyte and interface engineering for solid-state sodium batteries, *Joule* 2 (2018) 1747-1770.
- [167] H. Wan, J.P. Mwizerwa, F. Han, W. Weng, J. Yang, C. Wang, X. Yao, Grain-boundary-resistance-less Na_3SbS_4 -Se solid electrolytes for all-solid-state sodium batteries, *Nano Energy* 66 (2019) 104109.
- [168] P. Minnmann, F. Strauss, A. Bielefeld, R. Ruess, P. Adelhelm, S. Burkhardt, S.L. Dreyer, E. Trevisanello, H. Ehrenberg, T. Brezesinski, F.H. Richter, J. Janek, Designing cathodes and cathode active materials for solid-state batteries, *Adv. Energy Mater.* 12 (2022) 2201425.
- [169] Q. Sun, L. Dai, Y. Tang, J. Sun, W. Meng, T. Luo, L. Wang, S. Liu, Designing a novel electrolyte $\text{Na}_{3.2}\text{Hf}_2\text{Si}_{2.2}\text{P}_{0.8}\text{O}_{11.85}\text{F}_{0.3}$ for all-solid-state Na-O₂ batteries, *Small Methods* 6 (2022) e2200345.
- [170] B. Emley, Y. Liang, R. Chen, C. Wu, M. Pan, Z. Fan, Y. Yao, On the quality of tape-cast thin films of sulfide electrolytes for solid-state batteries, *Mater. Today Phys.* 18 (2021) 100397.

- [171] R.K. Nishihora, P.L. Rachadel, M.G.N. Quadri, D. Hotza, Manufacturing porous ceramic materials by tape casting—A review, *J. Eur. Ceram. Soc.* 38 (2018) 988-1001.
- [172] N. Riphaut, P. Strobl, B. Stiaszny, T. Zinkevich, M. Yavuz, J. Schnell, S. Indris, H.A. Gasteiger, S.J. Sedlmaier, Slurry-based processing of solid electrolytes: A comparative binder study, *J. Electrochem. Soc.* 165 (2018) A3993-A3999.
- [173] B. Emley, C. Wu, L. Zhao, Q. Ai, Y. Liang, Z. Chen, L. Guo, T. Terlier, J. Lou, Z. Fan, Y. Yao, Impact of fabrication methods on binder distribution and charge transport in composite cathodes of all-solid-state batteries, *Mater. Futures* 2 (2023) 045102.
- [174] R. Wei, S. Chen, T. Gao, W. Liu, Challenges, fabrications and horizons of oxide solid electrolytes for solid-state lithium batteries, *Nano Select* 2 (2021) 2256-2274.
- [175] J. Schnell, F. Tietz, C. Singer, A. Hofer, N. Billot, G. Reinhart, Prospects of production technologies and manufacturing costs of oxide-based all-solid-state lithium batteries, *Energy Environ. Sci.* 12 (2019) 1818-1833.
- [176] K.B. Hatzell, Y. Zheng, Prospects on large-scale manufacturing of solid state batteries, *MRS Energy Sustain.* 8 (2021) 33-39.
- [177] C. Wang, W. Ping, Q. Bai, H. Cui, R. Hensleigh, R. Wang, A.H. Brozena, Z. Xu, J. Dai, Y. Pei, C. Zheng, G. Pastel, J. Gao, X. Wang, H. Wang, J.-C. Zhao, B. Yang, X.R. Zheng, J. Luo, Y. Mo, B. Dunn, L. Hu, A general method to synthesize and sinter bulk ceramics in seconds, *Science* 368 (2020) 521-526.
- [178] O. Guillon, W. Rheinheimer, M. Bram, A perspective on emerging and future sintering technologies of ceramic materials, *Adv. Eng. Mater.* 25 (2023) 2201870.
- [179] C. Stan, C. Beavers, M. Kunz, N. Tamura, X-ray diffraction under extreme conditions at the advanced light source, *Quantum Beam Sci.* 2 (2018) 4.
- [180] J. Miao, T. Ishikawa, I.K. Robinson, M.M. Murnane, Beyond crystallography: Diffractive imaging using coherent x-ray light sources, *Science* 348 (2015) 530-535.
- [181] P.P. Paul, E.J. McShane, A.M. Colclasure, N. Balsara, D.E. Brown, C. Cao, B.R. Chen, P.R. Chinnam, Y. Cui, E.J. Dufek, D.P. Finegan, S. Gillard, W. Huang, Z.M. Konz, R. Kosteki, F. Liu, S. Lubner, R. Prasher, M.B. Preefer, J. Qian, M.T.F. Rodrigues, M. Schnabel, S.B. Son, V. Srinivasan, H.G. Steinrück, T.R. Tanim, M.F. Toney, W. Tong, F. Usseglio-Viretta, J. Wan, M. Yusuf, B.D. McCloskey, J. Nelson Weker, A review of existing and emerging methods for lithium detection and characterization in Li-ion and Li-metal batteries, *Adv. Energy Mater.* 11 (2021) 2100372.
- [182] J. Lefebvre, F. Galli, C.L. Bianchi, G.S. Patience, D.C. Boffito, Experimental methods in chemical engineering: X-ray photoelectron spectroscopy-XPS, *Can. J. Chem. Eng.* 97 (2019) 2588-2593.
- [183] W. Zhou, H.F. Greer, What can electron microscopy tell us beyond crystal structures?, *Eur. J. Inorg. Chem.* 2016 (2016) 941-950.
- [184] M. Aykol, J.H. Montoya, J. Hummelshøj, Rational solid-state synthesis routes for inorganic materials, *J. Am. Chem. Soc.* 143 (2021) 9244-9259.
- [185] B. Reif, S.E. Ashbrook, L. Emsley, M. Hong, Solid-state NMR spectroscopy, *Nat. Rev. Methods Primers* 1 (2021) 2.
- [186] K. Volgmann, V. Epp, J. Langer, B. Stanje, J. Heine, S. Nakhal, M. Lerch, M. Wilkening, P. Heitjans, Solid-state NMR to study translational Li ion dynamics in solids with low-dimensional diffusion pathways, *Z. Phys. Chem.* 231 (2017) 1215-1241.
- [187] P. Bottke, D. Rettenwander, W. Schmidt, G. Amthauer, M. Wilkening, Ion dynamics in solid electrolytes: NMR reveals the elementary steps of Li⁺ hopping in the garnet Li_{6.5}La₃Zr_{1.75}Mo_{0.25}O₁₂, *Chem. Mater.* 27 (2015) 6571-6582.

- [188] H. Zhang, Y. Shen, Y. Yu, Y. Huang, L. Chen, Advances in the application of solid-state nuclear magnetic resonance for the study of ion diffusion mechanism in battery materials, *Energy Storage Sci. Technol.* 9 (2020) 78-94.
- [189] B. Bhushan, Effect of tip radius on nanoindentation, *Microsyst. Technol.* 23 (2017) 1595-1649.
- [190] S. Strobl, S. Rasche, C. Krautgasser, E. Sharova, T. Lube, Fracture toughness testing of small ceramic discs and plates, *J. Eur. Ceram. Soc.* 34 (2014) 1637-1642.
- [191] F. Wu, L. Liu, S. Wang, J. Xu, P. Lu, W. Yan, J. Peng, D. Wu, H. Li, Solid state ionics – Selected topics and new directions, *Prog. Mater. Sci.* 126 (2022) 100921.
- [192] J. Maier, Defect chemistry composition, transport, and reactions in the solid state; part I: Thermodynamics, *Angew. Chem. Int. Ed.* 32 (1993) 313-335.
- [193] J. Maier, Defect chemistry: Composition, transport, and reactions in the solid state; part II: Kinetics, *Angew. Chem. Int. Ed.* 32 (1993) 528-542.
- [194] A.D. Poletayev, J.A. Dawson, M.S. Islam, A.M. Lindenberg, Defect-driven anomalous transport in fast-ion conducting solid electrolytes, *Nat. Mater.* 21 (2022) 1066-1073.
- [195] Y. Wang, Y. Wu, Z. Wang, L. Chen, H. Li, F. Wu, Doping strategy and mechanism for oxide and sulfide solid electrolytes with high ionic conductivity, *J. Mater. Chem. A* 10 (2022) 4517-4532.
- [196] A.R. Symington, M. Molinari, J.A. Dawson, J.M. Statham, J. Purton, P. Canepa, S.C. Parker, Elucidating the nature of grain boundary resistance in lithium lanthanum titanate, *J. Mater. Chem. A* 9 (2021) 6487-6498.
- [197] V. Vivier, M.E. Orazem, Impedance Analysis of Electrochemical Systems, *Chem. Rev.* 122 (2022) 11131-11168.
- [198] Y. Xiang, X. Li, Y. Cheng, X. Sun, Y. Yang, Advanced characterization techniques for solid state lithium battery research, *Mater. Today* 36 (2020) 139-157.
- [199] M. Petrowsky, R. Frech, Temperature dependence of ion transport: The compensated arrhenius equation, *J. Phys. Chem. B* 113 (2009) 5996-6000.
- [200] P. Vadhva, J. Hu, M.J. Johnson, R. Stocker, M. Braglia, D.J.L. Brett, A.J.E. Rettie, Electrochemical impedance spectroscopy for all-solid-state batteries: Theory, methods and future outlook, *ChemElectroChem* 8 (2021) 1930-1947.
- [201] N. Elgrishi, K.J. Rountree, B.D. McCarthy, E.S. Rountree, T.T. Eisenhart, J.L. Dempsey, A practical beginner's guide to cyclic voltammetry, *J. Chem. Educ.* 95 (2017) 197-206.
- [202] T. Schied, A. Nickol, C. Heubner, M. Schneider, A. Michaelis, M. Bobeth, G. Cuniberti, Determining the diffusion coefficient of lithium insertion cathodes from GITT measurements: Theoretical analysis for low temperatures, *ChemPhysChem* 22 (2021) 885-893.
- [203] J. Kasemchainan, S. Zekoll, D. Spencer Jolly, Z. Ning, G.O. Hartley, J. Marrow, P.G. Bruce, Critical stripping current leads to dendrite formation on plating in lithium anode solid electrolyte cells, *Nat. Mater.* 18 (2019) 1105-1111.
- [204] T. Krauskopf, H. Hartmann, W.G. Zeier, J. Janek, Toward a fundamental understanding of the lithium metal anode in solid-state batteries—an electrochemo-mechanical study on the garnet-type solid electrolyte $\text{Li}_{6.25}\text{Al}_{0.25}\text{La}_3\text{Zr}_2\text{O}_{12}$, *ACS Appl. Mater. Interfaces* 11 (2019) 14463-14477.
- [205] M. Wang, J.B. Wolfenstine, J. Sakamoto, Temperature dependent flux balance of the $\text{Li}/\text{Li}_7\text{La}_3\text{Zr}_2\text{O}_{12}$ interface, *Electrochim. Acta* 296 (2019) 842-847.
- [206] E. Dashjav, M. Gellert, G. Yan, D. Grüner, N. Kaiser, S. Spannenberger, I. Krалеva, R. Bermejo, M.-T. Gerhards, Q. Ma, J. Malzbender, B. Roling, F. Tietz, O. Guillon, Microstructure, ionic conductivity and

- mechanical properties of tape-cast $\text{Li}_{1.5}\text{Al}_{0.5}\text{Ti}_{1.5}\text{P}_3\text{O}_{12}$ electrolyte sheets, *J. Eur. Ceram. Soc.* 40 (2020) 1975-1982.
- [207] F. Snijkers, A. de Wilde, S. Mullens, J. Luyten, Aqueous tape casting of yttria stabilised zirconia using natural product binder, *J. Eur. Ceram. Soc.* 24 (2004) 1107-1110.
- [208] R. Ye, C.-L. Tsai, M. Ihrig, S. Sevinc, M. Rosen, E. Dashjav, Y.J. Sohn, E. Figgemeier, M. Finsterbusch, Water-based fabrication of garnet-based solid electrolyte separators for solid-state lithium batteries, *Green Chem.* 22 (2020) 4952-4961.
- [209] D. Hotza, P. Greil, Review: aqueous tape casting of ceramic powders, *Mater. Sci. Eng. A* 202 (1995) 206-217.
- [210] R. Ye, M. Ihrig, N. Imanishi, M. Finsterbusch, E. Figgemeier, A review on Li^+/H^+ exchange in garnet solid electrolytes: from instability against humidity to sustainable processing in water, *ChemSusChem* 14 (2021) 4397-4407.
- [211] Y. Li, W. Arnold, S. Halacoglu, J.B. Jasinski, T. Druffel, H. Wang, Phase-transition interlayer enables high-performance solid-state sodium batteries with sulfide solid electrolyte, *Adv. Funct. Mater.* 31 (2021) 2101636.
- [212] Y. Wang, S. Song, C. Xu, N. Hu, J. Molenda, L. Lu, Development of solid-state electrolytes for sodium-ion battery—A short review, *Nano Mater. Sci.* 1 (2019) 91-100.
- [213] N. Li, Z. Wen, Y. Liu, X. Xu, J. Lin, Z. Gu, Preparation of Na-beta'-alumina film by tape casting process, *J. Eur. Ceram. Soc.* 29 (2009) 3031-3037.
- [214] S.C. Ligon, M.C. Bay, M.V.F. Heinz, C. Battaglia, T. Graule, G. Blugan, Large planar Na-beta'- Al_2O_3 solid electrolytes for next generation Na-batteries, *Materials* 13 (2020) 433.
- [215] K. Okubo, H. Wang, K. Hayashi, M. Inada, N. Enomoto, G. Hasegawa, T. Osawa, H. Takamura, A dense NASICON sheet prepared by tape-casting and low temperature sintering, *Electrochim. Acta* 278 (2018) 176-181.
- [216] V. Petříček, M. Dušek, L. Palatinus, Crystallographic computing system JANA2006: General features, *Z. Kristallogr. – Cryst. Mater.* 229 (2014) 345-352.
- [217] W.C. Oliver, G.M. Pharr, An improved technique for determining hardness and elastic modulus using load and displacement sensing indentation experiments, *J. Mater. Res.* 7 (2011) 1564-1583.
- [218] X. Li, J. Malzbender, G. Yan, J. Gonzalez-Julian, R. Schwaiger, A combined experimental and modeling study revealing the anisotropic mechanical response of Ti_2AlN MAX phase, *J. Eur. Ceram. Soc.* 41 (2021) 5872-5881.
- [219] J.M. Valle, C. Huang, D. Tatke, J. Wolfenstine, W. Go, Y. Kim, J. Sakamoto, Characterization of hot-pressed von Alpen type NASICON ceramic electrolytes, *Solid State Ion.* 369 (2021) 115712.
- [220] J.T.S. Irvin, D.C. Sinclair, A.R. West, Electroceramics: characterization by impedance spectroscopy, *Adv. Mater.* 2 (1990) 132-138.
- [221] X. Yu, L. Xue, J.B. Goodenough, A. Manthiram, Ambient-temperature all-solid-state sodium batteries with a laminated composite electrolyte, *Adv. Funct. Mater.* 31 (2020) 2002144.
- [222] J. Zhang, J. Zhao, L. Yue, Q. Wang, J. Chai, Z. Liu, X. Zhou, H. Li, Y. Guo, G. Cui, L. Chen, Safety-reinforced poly(propylene carbonate)-based all-solid-state polymer electrolyte for ambient-temperature solid polymer lithium batteries, *Adv. Energy Mater.* 5 (2015) 1501082.
- [223] J.F. Nonemacher, S. Naqash, F. Tietz, J. Malzbender, Micromechanical assessment of Al/Y-substituted NASICON solid electrolytes, *Ceram. Int.* 45 (2019) 21308-21314.
- [224] P. Albertus, V. Anandan, C. Ban, N. Balsara, I. Belharouak, J. Buettner-Garrett, Z. Chen, C. Daniel, M. Doeff, N.J. Dudney, B. Dunn, S.J. Harris, S. Herle, E. Herbert, S. Kalnaus, J.A. Libera, D. Lu, S. Martin,

- B.D. McCloskey, M.T. McDowell, Y.S. Meng, J. Nanda, J. Sakamoto, E.C. Self, S. Tepavcevic, E. Wachsman, C. Wang, A.S. Westover, J. Xiao, T. Yersak, Challenges for and pathways toward Li-metal-based all-solid-state batteries, *ACS Energy Lett.* 6 (2021) 1399-1404.
- [225] M. Zhao, X.-Y. Li, X. Chen, B.-Q. Li, S. Kaskel, Q. Zhang, J.-Q. Huang, Promoting the sulfur redox kinetics by mixed organodiselenides in high-energy-density lithium-sulfur batteries, *eScience* 1 (2021) 44-52.
- [226] X. Chi, Y. Zhang, F. Hao, S. Kmiec, H. Dong, R. Xu, K. Zhao, Q. Ai, T. Terlier, L. Wang, L. Zhao, L. Guo, J. Lou, H.L. Xin, S.W. Martin, Y. Yao, An electrochemically stable homogeneous glassy electrolyte formed at room temperature for all-solid-state sodium batteries, *Nat. Commun.* 13 (2022) 2854.
- [227] J. Yue, F. Han, X. Fan, X. Zhu, Z. Ma, J. Yang, C. Wang, High-performance all-inorganic solid-state sodium-sulfur battery, *ACS Nano* 11 (2017) 4885-4891.
- [228] X.-Y. Yue, J. Zhang, J. Bao, Y.-F. Bai, X.-L. Li, S.-Y. Yang, Z.-W. Fu, Z.-H. Wang, Y.-N. Zhou, Sputtered MoN nanolayer as a multifunctional polysulfide catalyst for high-performance lithium-sulfur batteries, *eScience* 2 (2022) 329-338.
- [229] C.-J. Huang, J.-H. Cheng, W.-N. Su, P. Partovi-Azar, L.-Y. Kuo, M.-C. Tsai, M.-H. Lin, S. Panahian Jand, T.-S. Chan, N.-L. Wu, P. Kaghazchi, H. Dai, P.M. Bieker, B.-J. Hwang, Origin of shuttle-free sulfurized polyacrylonitrile in lithium-sulfur batteries, *J. Power Sources* 492 (2021) 229508.
- [230] M.A. Weret, W.N. Su, B.J. Hwang, Strategies towards high performance lithium-sulfur batteries, *Batteries Supercaps* 5 (2022) e202200059.
- [231] H.-J. Chang, X. Lu, J.F. Bonnett, N.L. Canfield, K. Han, M.H. Engelhard, K. Jung, V.L. Sprenkle, G. Li, Decorating β -alumina solid-state electrolytes with micron Pb spherical particles for improving Na wettability at lower temperatures, *J. Mater. Chem. A* 6 (2018) 19703-19711.
- [232] J. Hüttel, W. Cai, D. Wagner, J. Schilm, M. Kusnezoff, K. Nikolowski, N. Shaji, C.W. Lee, M. Partsch, A. Michaelis, Polarization impedance at the Na-Na₅YSi₄O₁₂ interface, *Solid State Ion.* 376 (2022) 115856.
- [233] Q. Ma, F. Tietz, Solid-state electrolyte materials for sodium batteries: Towards practical applications, *ChemElectroChem* 7 (2020) 2693-2713.
- [234] X. Han, Y. Gong, K.K. Fu, X. He, G.T. Hitz, J. Dai, A. Pearse, B. Liu, H. Wang, G. Rubloff, Y. Mo, V. Thangadurai, E.D. Wachsman, L. Hu, Negating interfacial impedance in garnet-based solid-state Li metal batteries, *Nat. Mater.* 16 (2017) 572-579.
- [235] S. Cai, H. Tian, J. Liu, S. Liu, L. Dai, J. Xu, L. Kong, L. Wang, Tuning Na₃Hf₂Si₂PO₁₂ electrolyte surfaces by metal coating for high-rate and long cycle life solid-state sodium ion batteries, *J. Mater. Chem. A* 10 (2022) 1284-1289.
- [236] L. Lu, Y. Lu, J.A. Alonso, C.A. Lopez, M.T. Fernandez-Diaz, B. Zou, C. Sun, A monolithic solid-state sodium-sulfur battery with Al-doped Na_{3.4}Zr₂(Si_{0.8}P_{0.2}O₄)₃ electrolyte, *ACS Appl. Mater. Interfaces* 13 (2021) 42927-42934.
- [237] T. An, H. Jia, L. Peng, J. Xie, Material and interfacial modification toward a stable room-temperature solid-state Na-S battery, *ACS Appl. Mater. Interfaces* 12 (2020) 20563-20569.
- [238] Y.-X. Wang, B. Zhang, W. Lai, Y. Xu, S.-L. Chou, H.-K. Liu, S.-X. Dou, Room-temperature sodium-sulfur Batteries: A comprehensive review on research progress and cell chemistry, *Adv. Energy Mater.* 7 (2017) 1602829.
- [239] W. Zhou, Y. Li, S. Xin, J.B. Goodenough, Rechargeable sodium all-solid-state battery, *ACS Cent. Sci.* 3 (2017) 52-57.

- [240] L. Liu, X. Qi, Q. Ma, X. Rong, Y.S. Hu, Z. Zhou, H. Li, X. Huang, L. Chen, Toothpaste-like electrode: A novel approach to optimize the interface for solid-state sodium-ion batteries with ultralong cycle life, *ACS Appl. Mater. Interfaces* 8 (2016) 32631-32636.
- [241] W. Zhou, H. Gao, J.B. Goodenough, Low-cost hollow mesoporous polymer spheres and all-solid-state lithium, sodium batteries, *Adv. Energy Mater.* 6 (2016) 1501802.
- [242] S. Zhang, K. Zhao, T. Zhu, J. Li, Electrochemomechanical degradation of high-capacity battery electrode materials, *Prog. Mater. Sci.* 89 (2017) 479-521.
- [243] M.J. Wang, E. Kazyak, N.P. Dasgupta, J. Sakamoto, Transitioning solid-state batteries from lab to market: Linking electro-chemo-mechanics with practical considerations, *Joule* 5 (2021) 1371-1390.
- [244] G.T. Hitz, D.W. McOwen, L. Zhang, Z. Ma, Z. Fu, Y. Wen, Y. Gong, J. Dai, T.R. Hamann, L. Hu, E.D. Wachsman, High-rate lithium cycling in a scalable trilayer Li-garnet-electrolyte architecture, *Mater. Today* 22 (2019) 50-57.
- [245] S. Xin, Y.X. Yin, Y.G. Guo, L.J. Wan, A high-energy room-temperature sodium-sulfur battery, *Adv. Mater.* 26 (2014) 1261-1265.
- [246] M.M. Li, X. Lu, X. Zhan, M.H. Engelhard, J.F. Bonnett, E. Polikarpov, K. Jung, D.M. Reed, V.L. Sprenkle, G. Li, High performance sodium-sulfur batteries at low temperature enabled by superior molten Na wettability, *Chem. Commun.* 57 (2021) 45-48.
- [247] J. Filik, A.W. Ashton, P.C.Y. Chang, P.A. Chater, S.J. Day, M. Drakopoulos, M.W. Gerring, M.L. Hart, O.V. Magdysyuk, S. Michalik, A. Smith, C.C. Tang, N.J. Terrill, M.T. Wharmby, H. Wilhelm, Processing two-dimensional X-ray diffraction and small-angle scattering data in DAWN 2, *J. Appl. Crystallogr.* 50 (2017) 959-966.
- [248] B.H. Toby, EXPGUI, a graphical user interface for GSAS, *J. Appl. Cryst.* 34 (2001) 210-213.
- [249] S.P. Brown, S. Wimperis, Two-dimensional multiple-quantum MAS NMR of quadrupolar nuclei. Acquisition of the whole echo, *J. Magn. Reson.* 124 (1997) 279-285.
- [250] S.P. Brown, S. Wimperis, Two-dimensional multiple-quantum MAS NMR of quadrupolar nuclei: A comparison of methods, *J. Magn. Reson.* 128 (1997) 42-61.
- [251] K. Takada, Progress in solid electrolytes toward realizing solid-state lithium batteries, *J. Power Sources* 394 (2018) 74-85.
- [252] F. Han, Y. Zhu, X. He, Y. Mo, C. Wang, Electrochemical stability of $\text{Li}_{10}\text{GeP}_2\text{S}_{12}$ and $\text{Li}_7\text{La}_3\text{Zr}_2\text{O}_{12}$ solid electrolytes, *Adv. Energy Mater.* 6 (2016) 1501590.
- [253] V. Lacivita, Y. Wang, S.-H. Bo, G. Ceder, Ab initio investigation of the stability of electrolyte/electrode interfaces in all-solid-state Na batteries, *J. Mater. Chem. A* 7 (2019) 8144-8155.
- [254] C.-M. Wu, P.-I. Pan, Y.-W. Cheng, C.-P. Liu, C.-C. Chang, M. Avdeev, S.-k. Lin, The mechanism of the sodiation and desodiation in Super P carbon electrode for sodium-ion battery, *J. Power Sources* 340 (2017) 14-21.
- [255] X. Liu, R. Garcia-Mendez, A.R. Lupini, Y. Cheng, Z.D. Hood, F. Han, A. Sharafi, J.C. Idrobo, N.J. Dudney, C. Wang, C. Ma, J. Sakamoto, M. Chi, Local electronic structure variation resulting in Li 'filament' formation within solid electrolytes, *Nat. Mater.* 20 (2021) 1485-1490.
- [256] C. Wang, T. Deng, X. Fan, M. Zheng, R. Yu, Q. Lu, H. Duan, H. Huang, C. Wang, X. Sun, Identifying soft breakdown in all-solid-state lithium battery, *Joule* 6 (2022) 1770-1781.
- [257] Y. Sadaoka, M. Matsuguchi, Y. Sakai, K. Komatsubara, Ionic conductivity in $\text{Na}_5\text{YSi}_4\text{O}_{12}$ -based ceramics with and without additives, *J. Mater. Sci.* 27 (1992) 5045-5051.
- [258] G.J. May, A. Hooper, The effect of microstructure and phase composition on the ionic conductivity of magnesium-doped sodium-beta-alumina, *J. Mater. Sci.* 13 (1978) 1480-1486.

- [259] Z. Deng, T.P. Mishra, E. Mahayoni, Q. Ma, A.J.K. Tieu, O. Guillon, J.N. Chotard, V. Seznec, A.K. Cheetham, C. Masquelier, G.S. Gautam, P. Canepa, Fundamental investigations on the sodium-ion transport properties of mixed polyanion solid-state battery electrolytes, *Nat. Commun.* 13 (2022) 4470.
- [260] L. Li, R. Xu, L. Zhang, Z. Zhang, M. Yang, D. Liu, X. Yan, A. Zhou, O-tailored microstructure-engineered interface toward advanced room temperature all-solid-state Na batteries, *Adv. Funct. Mater.* 32 (2022) 2203095.
- [261] Y. Ruan, F. Guo, J. Liu, S. Song, N. Jiang, B. Cheng, Optimization of $\text{Na}_3\text{Zr}_2\text{Si}_2\text{PO}_{12}$ ceramic electrolyte and interface for high performance solid-state sodium battery, *Ceram. Int.* 45 (2019) 1770-1776.
- [262] Y. Zhao, C. Wang, Y. Dai, H. Jin, Homogeneous Na^+ transfer dynamic at $\text{Na}/\text{Na}_3\text{Zr}_2\text{Si}_2\text{PO}_{12}$ interface for all solid-state sodium metal batteries, *Nano Energy* 88 (2021) 106293.
- [263] Z. Zhang, S. Wenzel, Y. Zhu, J. Sann, L. Shen, J. Yang, X. Yao, Y.-S. Hu, C. Wolverton, H. Li, L. Chen, J. Janek, $\text{Na}_3\text{Zr}_2\text{Si}_2\text{PO}_{12}$: A stable Na^+ -ion solid electrolyte for solid-state batteries, *ACS Appl. Energy Mater.* 3 (2020) 7427-7437.

Index of Figures

Figure 1 Overview of battery development milestones.	4
Figure 2 Milestone discoveries that shaped the modern LIBs.	12
Figure 3 Correct notation for the negative and positive potential limits for the electrolyte stability and the energy levels of HOMO and LUMO.	13
Figure 4 Illustration of a SIB system.	14
Figure 5 Specific energy of LIBs and SIBs based on different cathodes.	16
Figure 6 The cell configuration changes from liquid to solid system.	18
Figure 7 A slurry coating process to fabricate practical multilayer all-solid-state pouch cells.	19
Figure 8 The Ragone plots of the reported batteries and capacitors.	22
Figure 9 Timeline of the discovery and development of Na ⁺ ionic conductors.	24
Figure 10 Schematic (a) cell configuration and (b) operating principle of the Na/S battery with Na-β-Al ₂ O ₃	24
Figure 11 Crystal structures of Na-β/β''-Al ₂ O ₃	25
Figure 12 Crystal structures of rhombohedral and monoclinic NASICON compounds (Na ₃ Zr ₂ Si ₂ PO ₁₂).	27
Figure 13 Crystal structure of Na ₅ YSi ₄ O ₁₂ -type electrolyte.	29
Figure 14 Crystal structures of Na ₃ PS ₄ (cubic and tetragonal).	31
Figure 15 Ionic transport in solid inorganic electrolytes and solid polymer electrolytes.	34
Figure 16 A model explaining the sintering process.	38
Figure 17 Schematic of Bragg plane diffraction.	39
Figure 18 Schematic of X-ray photoelectric effect.	41
Figure 19 (a) Schematic of the indenting process and (b) schematic of the load-displacement curve.	43
Figure 20 Schematic of point defects in a crystal.	44
Figure 21 Cross-sectional SEM images of NYS tape with different thicknesses (120, 160, 260 and 450 μm).	51
Figure 22 Photograph of the sandwiched structure used for the tape sintering.	52
Figure 23 Crystal structure analysis of NYS tape.	54
Figure 24 Morphology of the NYS tape microstructure.	55
Figure 25 EDX analysis images of NYS tape.	55
Figure 26 The Nyquist plot of measured and fitted impedance spectrum for NYS tape at RT.	56
Figure 27 Arrhenius plots of bulk and total conductivities of the NYS tape.	58
Figure 28 The LSV profile of NYS tape.	59
Figure 29 The profile of the CCD measurement of NYS tape.	59
Figure 30 The profile of galvanostatic cycling stability measurement.	60
Figure 31 The nano-indentation curves for the loading-unloading cycles under 250 and 500 mN.	61
Figure 32 Shrinkage behavior of NYS tape.	63
Figure 33 Digital pictures of (a) the green tape and (b) the translucent sintered NYS tapes.	64
Figure 34 Particle size distribution measurement of NYS precursor.	70
Figure 35 Schematic processing steps of the preparation of NYS trilayers: milling of the raw materials, casting the slurries, drying, cutting, laminating, pressing and sintering the green tapes.	71
Figure 36 (a) Cross-sectional SEM image of the NYS trilayered structure, (b) and (c) magnified SEM images of the dense and porous layer, respectively.	72
Figure 37 (a) Refined XRD pattern after tape casting and sintering and (b) projection of crystal structure along the c-axis.	73
Figure 38 Electrochemical performance of NYS scaffold in Na/NYS/Na symmetric cells and Na/NYS/Au cells.	75

Figure 39 CCD measurement with stepwise increase of the current density until short-circuiting.	76
Figure 40 CV profile in the range of -0.5 V to 8 V vs. Na^+/Na in the $\text{Na}/\text{NYS}/\text{Au}$ cell with a scanning rate of 0.01 mV s^{-1}	77
Figure 41 Galvanostatic cycling performance of the $\text{Na}/\text{NYS}/\text{Na}$ symmetric cell at the current density of 1.3 mA cm^{-2} and capacity of 1.3 mAh cm^{-2}	78
Figure 42 Cycling performance of a symmetric cell at the current density of 2.4 mA cm^{-2}	78
Figure 43 DC polarization curves of the composite S cathode with different S ratios to measure the electronic conductivities.	79
Figure 44 Nyquist plots of the composite cathodes with different S contents.	79
Figure 45 Discharge/charge curves of the 1 st cycle for the different composite S cathodes.	80
Figure 46 XRD patterns of the composite cathode with varying S content.	81
Figure 47 Electrochemical performance of $\text{Na}/\text{NYS}/\text{S}$ full cells.	82
Figure 48 (a) CV profiles at different scanning rates from 1 mV s^{-1} to 100 mV s^{-1} in the range of 1.0 V to 3.5 V vs. Na^+/Na . (b) Relationship between peak current i_p and the square root of the scanning rate.	83
Figure 49 (a) C-rate performance measurement between 0.01 C and 2 C. (b) Change of specific capacity at different C-rates and areal-current densities.	84
Figure 50 Galvanostatic charge and discharge cycling performance and Coulombic efficiency at a current density of 0.01 C.	85
Figure 51 Photograph of the pressure-free $\text{Na}/\text{NYS}/\text{S}$ pouch cell and the powered light-emitting diode.	85
Figure 52 Comparison of different SSB cell architectures.	87
Figure 53 Schematic of the solid-state synthesis process, which consists of ball-mixing, solvent evaporation, powder pressing and sintering.	94
Figure 54 XRD patterns ($\lambda = 1.5406$ Å) of the synthesized $\text{Na}_{5-x}\text{Y}_{1-x}\text{Zr}_x\text{Si}_4\text{O}_{12}$ ($0 \leq x \leq 1$) with different Zr substitutions ($x = 0.04, 0.06, 0.08, 0.10, 0.12, 0.14, 0.20, 0.40, 0.60, 0.80, 1.0$).	95
Figure 55 Total conductivities at RT in the series $\text{Na}_{5-x}\text{Y}_{1-x}\text{Zr}_x\text{Si}_4\text{O}_{12}$ ($0 \leq x \leq 1$).	96
Figure 56 Synchrotron XRD refinement and projection of crystal structure of NYZS.	97
Figure 57 SEM and HRTEM images of NYZS crystal.	99
Figure 58 Cross-sectional view and EDX mapping of NYZS.	100
Figure 59 XPS survey spectra of NYS and NYZS.	101
Figure 60 The fitted XPS of (f) Y 3d, (g) Si 2p and (h) O 1s.	101
Figure 61 Comparison of XRD patterns ($\lambda = 1.5406$ Å) of the fresh sample and exposed sample after three months in ambient air.	102
Figure 62 Nyquist plots of the fresh sample and exposed sample after three months in ambient air.	103
Figure 63 (a) The temperature-dependent XRD patterns ($\lambda = 1.5406$ Å) and (b) values of a and c in a unit cell of NYZS between 25 and 1000 °C.	103
Figure 64 Nyquist plots of NYS and NYZS (inset: equivalent circuit for fitting).	105
Figure 65 Arrhenius plots of NYS and NYZS in the temperature range of ± 100 °C.	106
Figure 66 (a) Nyquist plot of NYZS with Na metal as electrodes (inset: equivalent circuit for fitting), revealing a low $R_{\text{interface}}$ between NYZS and Na metal. (b) CV curve of NYZS in the scanning range of $-0.5 \sim 10$ V vs. Na^+/Na with the rate of 0.1 mV s^{-1}	108
Figure 67 Electrochemical stability measurements of NYZS in the cells with (a-b) liquid electrolyte (LE) and (c-d) solid-state electrolyte NYZS.	109
Figure 68 CCD measurement against Na for testing the occurrence of Na metal dendrites with increasing current density until short-circuiting.	111
Figure 69 DC polarization curve during potentiostatic test for the electronic conductivity measurement. The inset is the magnified current curve.	112

Figure 70 Digital photograph of the pouch cell for the test. The Na/NYZS/Na symmetric pouch cells were assembled in the glovebox.	113
Figure 71 Galvanostatic cycling measurement at the current density of 1 mA cm^{-2} and the deposition capacity of 1 mAh cm^{-2} of NYZS. The insets are the magnified curves at different periods.	113
Figure 72 Nyquist plots at different cycling stages in the Na/NYZS/Na symmetric pouch cell.	114
Figure 73 Digital photographs of the NYZS pellet of both sides for post-test analysis in the Na/NYZS/Na symmetric cell after short-circuit.	114
Figure 74 The ^{23}Na magic-angle-spinning nuclear magnetic resonance (MAS NMR) spectra for both NYS and NYZS.	115
Figure 75 The ^{29}Si magic-angle-spinning nuclear magnetic resonance (MAS NMR) spectra for both NYS and NYZS.	116
Figure 76 The ^{89}Y magic-angle-spinning nuclear magnetic resonance (MAS NMR) spectra for both NYS and NYZS.	117
Figure 77 The 2D ^{23}Na MQ MAS NMR spectra of (a) NYS and (b) NYZS.	118
Figure 78 Temperature-dependent static ^{23}Na spectra acquired between 260 and 595 K for (a) NYS and (b) NYZS.	119
Figure 79 The different contributions are labeled with “A”, “B”, “C” and “D”. Temperature-dependent static ^{23}Na NMR linewidths (full width at half maximum, FWHM) for (a) NYS and (b) NYZS (cf. Figure 77).	119
Figure 80 Static ^{23}Na relaxometry: temperature-dependent relaxation rates T_1^{-1} for (e) NYS and (f) NYZS.	120
Figure 81 Static ^{23}Na relaxometry: the corresponding signal fractions in the magnetization transients of (g) NYS and (h) NYZS.	121
Figure 82 Simulation results for NYS and NYZS.	123
Figure 83 Comparison of electrical conductivity between NYZS and reported representative Na^+ ionic SSEs.	124
Figure 84 Comparison of electrochemical stability between NYZS and reported representative Na^+ ionic SSEs.	126

Index of Tables

Table 1 Comparison of Li and Na elements' physical and chemical properties.	7
Table 2 Comparison between liquid and solid electrolytes for Na-based batteries.....	19
Table 3 Composition, structure data and conductivity of Na- $\beta/\beta'/\beta''$ -Al ₂ O ₃	26
Table 4 Conductivity and activation energy of NASICONs.	28
Table 5 Conductivity and activation energy of reported Na ₅ YSi ₄ O ₁₂ materials.....	30
Table 6 Conductivity and activation energy of sulfides.	32
Table 7 Slurry recipe for the NYS tape.	51
Table 8 The attributions of each component in the equivalent circuit are in Figure 26	57
Table 9 Comparison of ionic conductivity, activation energy and electrochemical stability window with representative Li ⁺ and Na ⁺ electrolytes, especially tape-cast samples.	57
Table 10 Mechanical properties of NYS tape determined by nano-indentation method.	61
Table 11 Comparison of synthesis, thermal and mechanical properties with representative Li ⁺ /Na ⁺ SSEs.	61
Table 12 Shrinkage of the tapes during sintering.	63
Table 13 The cost comparison of representative Li ⁺ /Na ⁺ SSEs tapes.	64
Table 14 Formulations of the composite cathodes with different S content.	68
Table 15 The parameters of NYS unit cell from refined XRD data.	73
Table 16 Values of the individual equivalent circuit elements of the fitted impedance spectra of Na/NYS/Na cells.....	75
Table 17 Summary of the conductive and capacity performance of the composite cathodes with different S contents.	80
Table 18 The current setting at different C-rates for the electrochemical tests of the full cell.	84
Table 19 Comparison of cell specifications of Na-based and Li-based batteries, mostly with sulfur as cathode active material.	88
Table 20 Total conductivities at RT ($\sigma_{\text{total-RT}}$) and the analysis of major secondary phases in the series Na _{5-x} Y _{1-x} Zr _x Si ₄ O ₁₂ (0 ≤ x ≤ 1), corresponding to Figure 54	96
Table 21 Parameters of refined structures of NYS and NYZS.....	98
Table 22 Site occupancies, atomic coordinates isotropic displacement parameters of NYZS.	98
Table 23 The comparison of binding energy between NYS and NYZS.	101
Table 24 Comparison of specific bond lengths between NYS and NYZS.....	102
Table 25 Values of the fitted equivalent circuit in the symmetric Au/SSE/Au cells (corresponding to Figure 64).	105
Table 26 Linear fitting equations of NYS and NYZS (Corresponds to Figure 65).....	107
Table 27 Bulk ($E_{\text{a-bulk}}$) and total ($E_{\text{a-total}}$) activation energy of NYS and NYZS (Corresponding to Figure 65).	107
Table 28 The fitted equivalent circuit in the symmetric Na/NYZS/Na cells (Corresponds to Figure 66a).	108
Table 29 Comparison of conductivity and activation energy of NYZS with reported data (Corresponds to Figure 83).	125
Table 30 Comparison of the CCD and electrochemical window of NYZS with reported work (Corresponds to Figure 84).	126

Acknowledgments

I want to take this opportunity to express my deepest gratitude to everyone who has contributed to the successful completion of my doctoral thesis entitled “ $\text{Na}_5\text{YSi}_4\text{O}_{12}$ -type Na^+ superionic conductors for solid-state batteries”.

First and foremost, I would like to express my sincere appreciation to my doctoral supervisor, Prof. Olivier Guillon, for his unwavering support, guidance, and encouragement throughout my research journey. His expert knowledge, constructive feedback, and continuous support have been beneficial in shaping the direction of my research and improving the quality of my work.

I would also like to sincerely thank my scientific supervisors sincerely, Dr. Qianli Ma and Dr. Frank Tietz, for their invaluable advice, guidance, insightful suggestions, constructive criticism and support throughout my doctoral period. Their expertise in materials science and electrochemistry has been crucial in guiding my research and helping me overcome various challenges.

I would also like to extend my gratitude to my colleagues at Forschungszentrum Jülich, especially Dr. Ruijie Ye (scientific discussion and tape-casting), Dr. Enkhtsetseg Dashjav (scientific discussion and XRD refinement), Mr. Volker Bader (heat treatment), Ms. Marie Theres-Gerhards (thermal analysis and assistance in the lab work), Dr. Martin Ihrig (scientific discussion), Dr. Dapeng Zhou (assistance in the lab work), Dr. Wenyu Zhou (scientific discussion), Mr. Kai Yao (theoretical simulation and scientific discussion), Dr. Xiaoqiang Li (mechanical measurements), Dr. Daniel Grüner (SEM measurements), Mr. Jie Chen (SEM characterization) and Mr. Xinwei Zhu (theoretical discussion) for their support, encouragement, and helpful discussions. Their camaraderie and teamwork have made my research journey more enjoyable and rewarding.

I am also very grateful to my collaborators in Germany and China, including Prof. Jun Chen (Nankai University; scientific discussion and guidance), Prof. Xingchao Wang (Xinjiang University; scientific discussion, XPS and TEM characterization), Prof. Wei Xie (Nankai University; discussion of career direction), Dr. Sylvio Indris (Karlsruhe Institute of Technology; NMR measurements and discussion), Dr. Hang Li (Karlsruhe Institute of Technology; NMR measurements and discussion), Dr. Mareen Schaller (Karlsruhe Institute of Technology; NMR measurements and discussion), Dr. Igor Moudrakovski (Max Planck Institute for Solid State Research; NMR measurements and discussion), Dr. Qionqiong Lu (IFW Dresden and Henan Academy of Sciences; scientific discussion), Dr. Huimin Song (Peking University; XRD refinement), Dr. Dequan Jiang (Peking University, XRD refinement), Dr. Qiu Zhang (Nankai University; scientific discussion), Dr. Lin Li (Wenzhou University; scientific discussion), Mr. Shuo Zhao (Nankai University; simulation assistance), Dr. Martin Etter (Deutsches Elektronen-Synchrotron (DESY);

synchrotron XRD measurement and analysis) and Dr. Xingchen Shen (Laboratoire de Cristallographie et Sciences des Matériaux (CRISMAT), CNRS; synchrotron XRD analysis). Their support, contributions, and discussions have been invaluable to my research project and have enriched my research experience.

I am very grateful to Prof. Egbert Figgemeier for being able to be my second reviewer and for providing valuable comments and suggestions that made my doctoral thesis more comprehensive. I am grateful to Prof. Jesus Gonzalez-Julian for being the host of my defense and for providing the Institute of Mineral Engineering (GHI) as the venue for my defense. I appreciate the help, support and coordination during my doctoral procedure from the doctoral committee at the Faculty of Georesources and Materials Engineering.

I want to acknowledge the generous funding from the China Scholarship Council (CSC), Forschungszentrum Jülich, RWTH Aachen University and MatKat Foundation. These financial supports have enabled me to pursue my doctoral studies and carry out my research project.

Band / Volume 606

**Examining transport in the Upper Troposphere –
Lower Stratosphere with the infrared limb imager GLORIA**

L. Krasauskas (2023), v, 107 pp

ISBN: 978-3-95806-691-5

Band / Volume 607

**Sustainable Fabrication of Ceramic Solid Electrolytes
for Solid-State Lithium Batteries**

R. Ye (2023), vi, 119 pp

ISBN: 978-3-95806-694-6

Band / Volume 608

**Improving Nitrogen Retention in Soils Treated with Pig and Cattle Slurry
Through the Use of Organic Soil Amendments**

X. Cao (2023), XVI, 119 pp

ISBN: 978-3-95806-696-0

Band / Volume 609

**Mechanisches Verhalten von Polymer-Elektrolyt-Membran-
Elektrolysezellen und -Stacks**

S. Holtwerth (2023), x, 251 pp

ISBN: 978-3-95806-697-7

Band / Volume 610

Membrane Reactor Concepts for Power-to-Fuel Processes

H. Huang (2023), VI, 197 pp

ISBN: 978-3-95806-703-5

Band / Volume 611

**Deployment of Fuel Cell Vehicles in Road Transport and the
Expansion of the Hydrogen Refueling Station Network: 2023 Update**

R. C. Samsun, M. Rex (2023), i, 39 pp

ISBN: 978-3-95806-704-2

Band / Volume 612

**Behavior/performance of tungsten as a wall material
for fusion reactors**

M. Gago (2023), X, 120 pp

ISBN: 978-3-95806-707-3

Band / Volume 613

**Strategieentwicklung zur Umsetzung der Klimaschutzziele im
Verkehrssektor mit dem Fokus Kraftstoffe**

M. Decker (2023), ix, 243 pp

ISBN: 978-3-95806-714-1

Band / Volume 614

Joining of tungsten and steel for the first wall of a future fusion reactor

V. Ganesh (2023), xxx, 142, a-v pp

ISBN: 978-3-95806-715-8

Band / Volume 615

Polluter group specific emission optimisation for regional air quality analyses using four-dimensional variational data assimilation

P. M. Backes (2023), xxi, 115 pp

ISBN: 978-3-95806-717-2

Band / Volume 616

Effect of organic soil amendments on increasing soil N retention and reducing N losses from agricultural soils

Z. Li (2023), XI, 134 pp

ISBN: 978-3-95806-721-9

Band / Volume 617

Radiolytic Stability of BTBP-, BTPhen- and DGA-based Ligands for the Selective Actinide Separation by Solvent Extraction

H. Schmidt (2023), ca. 200 pp

ISBN: 978-3-95806-723-3

Band / Volume 618

Na₅YSi₄O₁₂-type Na⁺ superionic conductors for solid-state batteries

A. Yang (2023), X, 150 pp

ISBN: 978-3-95806-731-8

Weitere **Schriften des Verlags im Forschungszentrum Jülich** unter
<http://wwwzb1.fz-juelich.de/verlagextern1/index.asp>

Energie & Umwelt / Energy & Environment
Band / Volume 618
ISBN 978-3-95806-731-8